Forschungszentrum Rossendorf

Institut für Sicherheitsforschung

Abschlussbericht / Final Report

Reaktorsicherheitsforschung –Vorhaben-Nr.: 1501256
(Projekt im Rahmen der WTZ zwischen Russland und Deutschland)

Reactor Safety Research – Project No.: 1501256
(Project in the frame of the Russian-German Science and Technology Cooperation)

Vorhabenstitel:
Mikrostrukturelle Mechanismen der Strahlenversprödung

Project Title:
Microstructural Mechanisms of the radiation embrittlement

Autoren / Authors:
Eberhard Altstadt
Jürgen Böhmert
Andreas Ulbricht
Vladimir A. Borodin*
Maria Ganchenkova**
Roman Voskoboinikov**

* Kurchatov-Institut Moskau
** Moscow Engineering Physics Institute

Dienststelle des Autors / Performing Organisation:
Forschungszentrum Rossendorf e. V.

Berichtsdatum / Publication Date: 05. Mai 2006

Berichts – Nr. / Report - No: FZR-452

Hinweis:

Das diesem Bericht zugrunde liegende Vorhaben wurde mit Mitteln des Bundesministeriums für Wirtschaft und Technologie (BMWi) unter dem Förderkennzeichen 150 1256 gefördert. Die Verantwortung für den Inhalt dieser Veröffentlichung liegt bei den Autoren.

Kurzfassung

Gegenstand des Vorhabens im Rahmen der WTZ mit Russland ist die Versprödung des Reaktordruckbehälters infolge der Strahlenbelastung mit schnellen Neutronen im kernnahen Bereich.

Um den Einfluss von bestrahlungsinduzierten Gitterdefekten auf die mechanischen Eigenschaften zu ermitteln, wurden analytische Berechnungen zum Einfluss von Hindernissen auf die Beweglichkeit von Versetzungen und damit auf die Ausbildung einer plastischen Zone an der Rissspitze durchgeführt. Es wird demonstriert, dass sich die an der Rissspitze entstehenden Versetzungen an dem Hindernis (bestrahlungsinduzierte Punktdefekte) aufstauen. In Abhängigkeit der Rissbelastung K_I und der Entfernung des Hindernisses von der Rissspitze werden die Versetzungsdichte und das durch den Versetzungsstau verursachte Spannungsfeld berechnet.

Mit Hilfe von Experimenten zur Neutronenkleinwinkelstreuung (SANS – small angle neutron scattering) an verschiedenen WWER-Stählen und Modelllegierungen wurden Größenverteilungen und die Volumenanteile der strahleninduzierten Defekte für verschiedene Bestrahlungszustände (Fluenzen, Bestrahlungstemperaturen) ermittelt. Es wurde gezeigt, dass sich die strahleninduzierte Werkstoffschädigung durch Wärmebehandlung weitgehend wieder ausheilen lässt. Nach der thermischen Ausheilung ist der Werkstoff bei erneuter Bestrahlung weniger anfällig für strahleninduzierte Defekte. Die Ergebnisse der SANS-Untersuchungen wurden mit der Änderung der mechanischen Eigenschaften (Härte, Streckgrenze und Sprödbruchübergangstemperatur) korreliert.

Mit der kinetischen Gitter-Monte-Carlo-Methode wurden numerische Sensitivitätsstudien zum Einfluss des Cu-Gehalts auf die Stabilität von Defekt-Clustern durchgeführt. Die Berechnungen zeigen, dass die Anwesenheit von Cu-Atomen zur Bildung von langlebigen Defekten führt. Dabei werden Leerstellen in Cu/Leerstellen-Cluster eingefangen. Leerstellen in reinem Eisen sind bei Bestrahlungstemperaturen von 270 °C dagegen nicht stabil, die Lebensdauer liegt zwischen 10^{-2} s und 1 s. Die kritische Cu-Konzentration, ab welcher stabile Defekte entstehen, beträgt ca. 0.1 Masseprozent.

Abstract

The embrittlement of the reactor pressure vessel steel due to neutron irradiation is the subject of this project under the umbrella of the scientific technological cooperation with Russia.

To evaluate the influence of irradiation induced microstructure defects to the mechanical properties, the influence of obstacles to the mobility of dislocations and thus to the development of the plastic zone has been analytically calculated. It is shown that the dislocations nucleated at a crack tip are piled up in front of the obstacle (irradiation induced point defect). The dislocation density and the stress field due to the dislocation pile-up are calculated in dependence on the crack load K_I and the distance between crack tip and obstacle.

By means of small angle neutron scattering (SANS) experiments at various VVER steels and model alloys, size distributions and volume fractions of the irradiation defects have been investigated for different irradiation conditions (fluence, irradiation temperature). It is shown that the irradiation damage can be rescinded to a large extend by thermal treatment. After the annealing the material is less sensitive to irradiation defects during a re-irradiation. The results of the SANS experiments have been correlated to the change of mechanical properties (hardness, yield strength, ductile-brittle transition temperature).

By means of the kinetic lattice Monte-Carlo method, numerical sensitivity studies have been performed, related to the influence of Cu content on the stability of defect clusters. The calculations show that the presence of Cu leads to stable microstructure defects. During this process vacancies are trapped by Cu/V-Clusters. Contrary to this, vacancies in pure iron are not stable at irradiation temperatures of 270 °C. Their life time lies between 10^{-2} s and 1 s. The critical Cu concentration for the generation of stable defect clusters is about 0.1 w%.

Inhalt

1 Einleitung und Aufgabenstellung

Die Strahlenversprödung von Strukturwerkstoffen ist von hoher wissenschaftlicher und sicherheitstechnischer Relevanz. Das gilt besonders für die Strahlenversprödung von ferritischen Stählen, die für die Reaktordruckbehälter der Leichtwasserreaktoren eingesetzt werden. Hier führt die Strahlenversprödung zu einer Verschiebung der Übergangstemperatur zwischen sprödem und duktilem Bruchverhalten zu höheren Temperaturen und zu einer Verringerung der Zähigkeit im Temperaturbereich des duktilen Bruchverhaltens. Dadurch kann der spontane spröde Bruch eines Druckbehälters unter Belastungsbedingungen bestimmter Auslegungsstörfälle nicht mehr mit Sicherheit ausgeschlossen werden. Sicherheitstechnisch wird das Problem beherrscht durch konservative Auslegungsregeln und betriebsbegleitende Versprödungsüberwachungsprogramme. In den Fällen, in denen hohe Neutronenflussdichten am Reaktordruckbehälter auftreten, besonders strahlenversprödungsempfindliches Material verwendet wurde, und/oder nach langen Betriebszeiten kann die Strahlenversprödung zu einschneidenden Konsequenzen für den Weiterbetrieb der Anlage führen. So konnten die WWER-Reaktoren vom Typ 440/230 nur nach einer Ausheilglühung weiterbetrieben werden. Ähnliche Maßnahmen sind inzwischen aktuell für die Reaktoren vom Typ WWER 440/213 oder werden diskutiert für ältere US-amerikanische Druckwasserreaktoren.

In Anbetracht der hohen sicherheitstechnischen Bedeutung des Phänomens ist ein physikalisch fundiertes Verständnis und eine gut begründete Quantifizierung der Sicherheitsmargen unverzichtbar. International wird demzufolge dieser Aufgabe hohe Aufmerksamkeit gewidmet. Die Bemühungen sind allerdings auf die ASTM-bezogenen Reaktordruckbehälterstähle und auf die in westlichen Druckwasserreaktoren herrschenden Bedingungen ausgerichtet. Typ und metallurgische Behandlung russischer Reaktordruckbehälterstähle unterscheiden sich aber ebenso wie die Einsatzbedingungen in den WWER-Reaktoren davon durchaus essentiell.

Das Vorhaben zielt auf die Entwicklung eines aus der Physik der fundamentalen Werkstoffprozesse abgeleiteten Modells der Strahlenversprödung mit spezieller Anwendung auf WWER-Bedingungen. Dieses Modell soll die Bruchzähigkeit eines Druckbehälterstahles als Funktion der Bestrahlungsparameter (Neutronenflussdichte, Fluenz, Bestrahlungstemperatur) und der ursprünglichen Materialeigenschaften vorherzusagen gestatten. Das Modell umfasst die Beschreibung der Kinetik der Strukturänderung infolge Bestrahlung und die Modellierung des Spröd-duktil-Übergangsverhaltens unter Berücksichtigung einer Struktur mit Strahlendefekten. Die Korrelation mit Strukturuntersuchungen und mechanischen Werkstoffprüfungen an bestrahlten WWER-Reaktordruckbehälterstählen justiert und verifiziert das Modell.

In dieser Weise unterstützt das Vorhaben die förderpolitischen Ziele der Reaktorsicherheitsforschung auf dem Gebiet der Komponentensicherheit und der Integritätsbewertung, insbesondere im Hinblick auf das Werkstoffverhalten bei Langzeitbetrieb und unter Bestrahlung. Das Vorhaben schafft die Grundlage für ein im Rahmen der bilateralen wissenschaftlich-technischen Kooperation auf dem Gebiet der friedlichen Nutzung der Kernenergie zwischen MINATOM und dem BMWi vereinbartes Projekt (Themenbereich A.4 Komponentensicherheit und Qualitätssicherung, Aktivität A.4.2).

2 Voraussetzungen

Das Vorhaben ist als ein Beitrag für die bilaterale wissenschaftlich-technische Zusammenarbeit zwischen Deutschland und Russland auf dem Gebiet der Reaktorsicherheit konzipiert. Es verknüpft die qualifizierte wissenschaftliche Kompetenz der Arbeitsgruppe aus dem Institut für Allgemeine und Kernphysik des RRC Kurtchatov-Institut Moskau auf dem Gebiet der Modellierung werkstoffphysikalischer Prozesse mit den langjährigen Erfahrungen des FZR auf dem Gebiet der mechanischen Charakterisierung und der strukturanalytischen Untersuchung von WWER-Reaktordruckbehälterstählen. In dieser Weise erfolgt auch die Arbeitsteilung im Vorhaben: Das RRC entwickelt das analytische Modell des Mechanismus der Strahlenversprödung, während das FZR die mechanischen und mikrostrukturellen Parameter zur Verfügung stellt.

Die SANS-Untersuchungen werden an den einschlägigen Neutronen-Kleinwinkelstreuanlagen in nationalen und EU-Großforschungseinrichtungen durchgeführt. Die Software zur Auswertung der SANS-Messungen steht im FZR zur Verfügung. Zur Probenhandhabung und Probenvorbereitung stehen am FZR Radionuklidlabors zur Verfügung.

Für die Entwicklung von Simulationsmodellen steht entsprechende Rechentechnik, sowie ein FORTRAN Compiler zur Verfügung. Für die makroskopischen Finite-Elemente-Simulationen ist das Programm ANSYS® verfügbar.

3 Planung und Ablauf des Vorhabens

3.1 Wissenschaftlich-technische Einzelziele

Die Versprödung des Reaktordruckbehälters infolge der Strahlenbelastung im kernnahen Bereich ist ein Phänomen von hoher sicherheitstechnischer Relevanz. Das gilt besonders für Reaktoren der WWER-Baureihen. Das Phänomen wird sicherheitstechnisch auf der Grundlage konservativer Auslegungsvorschriften beherrscht, lässt sich aber noch nicht befriedigend mit einem aus der Physik der fundamentalen Werkstoffprozesse abgeleiteten Modell beschreiben. Das Vorhaben zielt auf die Entwicklung eines solchen Modells mit spezieller Ausrichtung auf die WWER-Bedingungen. Das Modell soll einen Beitrag leisten zur Bestimmung der Bruchzähigkeit eines Druckbehälterstahles als Funktion der Bestrahlungsparameter (Neutronenflussdichte, Fluenz, Bestrahlungstemperatur) und der ursprünglichen Materialeigenschaften. Es umfasst die Beschreibung der Kinetik der Strukturänderung infolge Bestrahlung und die Modellierung des Spröd-duktil-Übergangsverhaltens für eine Struktur mit Strahlendefekten. Die Korrelation mit Strukturuntersuchungen und mechanischen Werkstoffprüfungen an bestrahlten WWER-Reaktordruckbehälterstählen dient der Anpassung und Verifikation des Modells.

In dem Vorhaben wurden folgende Einzelziele verfolgt:

- Entwicklung eines analytischen Modells des Überganges vom spröden zum duktilen Bruchverhalten in Reaktordruckbehälterstählen auf der Grundlage von Rissinitiierung und Rissfortschritt in einer Matrix mit Ausscheidungen. Das Modell beruht auf der Analyse der Wechselwirkung eines Risses mit einem Ensemble von Ausscheidungen unterschiedlicher Größenskalen.
- Experimentelle und theoretische Untersuchungen über die Kinetik der Bildung strahleninduzierter Ausscheidungen zielen auf die Entwicklung eines kineti-

schen Modells. Es sollen Anzahldichte und Größe unterschiedlicher Arten von Ausscheidungen als Funktion der Bestrahlungsparameter und der chemischen Zusammensetzung des Druckbehälterstahles vorausgesagt werden. Die experimentellen Ergebnisse werden aus SANS-Experimenten mit Testlegierungen, mit russischen Surveillance-Proben und mit Bestrahlungsproben aus dem Bestrahlungsexperiment Rheinsberg gewonnen. Neben der Aufbereitung vorhandener Untersuchungen sind punktuell auch ergänzende SANS-Untersuchungen durchzuführen.

- Die Modell-Vorhersagen der Versprödungsparameter sollen mit experimentellen Ergebnissen korreliert werden. Insbesondere soll der Zusammenhang von mikrostrukturellen Defekten und der Änderung der mechanischen Eigenschaften aufgezeigt werden. Die Strukturuntersuchungen (SANS) und die mechanischen Tests werden jeweils am gleichen Probensatz durchgeführt.

3.2 Arbeitsplan

Das Vorhaben umfasst folgende Arbeitspakete (AP):

AP1 – Entwicklung eines analytischen Modells für den Spröd-duktil-Übergang: Das Modell beruht auf der Analyse der Wechselwirkung eines Risses mit einem Ensemble von Ausscheidungen unterschiedlicher Größenskalen.

AP2 – Strukturanalysen mit SANS-Experimenten: An bestrahlten Testlegierungen, russischen Surveillance-Proben und Proben aus dem Bestrahlungsprogramm Rheinsberg werden SANS-Untersuchungen durchgeführt. Es werden charakteristische Strukturparameter bestimmt.

AP3 – Entwicklung eines kinetischen Modells der Strahlendefektbildung: Das Modell soll Typ, Größe und Anzahldichte von bestrahlungsbedingten Strukturdefekten in Abhängigkeit von den Bestrahlungsparametern und der chemischen Zusammensetzung liefern.

AP4 – Korrelation der Modell-Vorhersage mit experimentellen Ergebnissen: Vorhandene Ergebnisse zur Mikrostrukturentwicklung und zur Änderung der mechanischen Eigenschaften infolge Bestrahlung sind mit den Aussagen der in AP1 und AP3 entwickelten Modelle zu vergleichen. Strukturuntersuchungen und mechanische Prüfungen sind jeweils am gleichen Probensatz durchzuführen.

4 Stand von Wissenschaft und Technik

4.1 Internationale Aktivitäten

Einen guten Überblick über den aktuellen Stand des physikalischen Verständnisses zum Mechanismus der Strahlenversprödung und den Modellansätzen zur quantitativen Beschreibung des Phänomens liefern die Arbeiten von Odette und Mitarbeitern [1-4]. Die Strahlenschädigung wird als hochkomplexer, mehrstufiger Prozess betrachtet. Sie beginnt mit der Erzeugung stark strukturgeschädigter Zonen als Folge der ballistischen Prozesse und führt zu Bestrahlungsdefekten im nanodispersen Bereich, die sich als Folge bestrahlungsbeschleunigter Diffusion oder neuer thermodynamischer Randbedingungen in einem an Gitterfehlstellen reichen Umfeld herausbilden. Struktur und Zusammensetzung dieser nanodispersen Defekte sind weitestgehend unbekannt. Abhängig von der Zusammensetzung des Stahles werden kupfer-

reiche Ausscheidungen (CRP) oder Leerstellencluster (voids) angenommen. Bei hohen, für die Druckbehälterstähle nicht mehr relevanten Cu-Gehalten sind CRPs unzweifelhaft nachgewiesen. Im Bereich des üblichen Cu-Gehaltes (0.05-0.3 %) lassen Untersuchungen mit Neutronenkleinwinkelstreuung (SANS) und mit Atomsonden-Feldionen-Mikroskopie (APFIM) eher die Bildung von Leerstellen-Fremdatom-Komplexen vermuten. Diese Komplexe haben eine matrix-ähnliche Struktur und weit variierende Zusammensetzung. Die Bildung von CRPs und Leerstellencluster wird mit Methoden der Molekulardynamik bereits modelliert. Ferner existieren kinetische Modelle zur Beschreibung der Wachstums- und Vergröberungsphase für beide Defekttypen.

Die Strukturdaten werden zur Beschreibung der Strahlenversprödung benutzt. Der Versprödungseffekt wird dabei als Strahlenverfestigungseffekt interpretiert und der Zusammenhang zwischen dem strahlenbedingten Anstieg der Streckgrenze und den Parametern der Strahlendefektstruktur (Volumenanteil, Defektgröße) modelliert. Grundlage ist die Wechselwirkung zwischen Versetzung und Bestrahlungsdefekt nach dem Orowan- oder dem Russell-Brown-Mechanismus. Für WWER-Stähle wurden vergleichbare Ergebnisse nicht publiziert.

4.2 Eigene Vorarbeiten

Am FZR sind im Rahmen des BMWi-Projektes “Nachweis, Interpretation und Bewertung Neutronen induzierter Defektstrukturen bei WWER-Reaktordruckbehälterstählen” (Förderkennzeichen: 1501012) umfangreiche Strukturuntersuchungen vorzugsweise mit SANS-Experimenten an bestrahlten WWER-Druckbehälterstählen und Modelllegierungen durchgeführt worden [5]. Sie lassen den Einfluss von Fluenz, Zusammensetzung und Bestrahlungstemperatur erkennen. Es werden Defektstrukturen mit einem scharfen Verteilungsmaximum bei einem Radius von ca.1 nm gefunden. Die Fluenz verändert die Verteilungsfunktion nicht, statt dessen führt zunehmende Neutronenfluenz zu zunehmendem Volumenanteil der Defekte. Auch Kupfer spielt eine große Rolle und beeinflusst den Volumenanteil, den Typ und die Fluenzabhängigkeit.

Weiterhin wurden an Proben aus WWER-Druckbehälterstählen, die in einem umfangreichen Bestrahlungsexperiment im WWER-Prototypreaktor WWER-2 des KKW Rheinsberg bestrahlt worden waren, Festigkeits- und Zähigkeitseigenschaften bestimmt [6-9]. In Zusammenarbeit mit dem RRC Kurtchatov-Institut Moskau sind darüber hinaus auch die Zähigkeitseigenschaften an Modelllegierungen mit unterschiedlichen Gehalten an die Strahlenversprödung fördernden Elementen ermittelt worden [10,11]. Dadurch liegt ein für WWER-Werkstoffe in dieser Form einmaliger Datenbestand vor, der unmittelbar mechanische Eigenschaft und Strukturparameter kombiniert.

Neue Ansätze zur Modellierung der Sprödbruchanfälligkeit bestrahlter Materialien wurden von den Mitarbeitern des RRC Kurtchatov-Institut Moskau erarbeitet. Sie betrachten das Spannungsfeld in der Umgebung einer Rissspitze unter dem Einfluss von Ausscheidungen und dessen Einfluss auf die Emission von Versetzungen aus der Rissspitze [12,13]. Zusätzlich wurde eine innovative Näherung zur Bildung von CRPs im Wirkungsbereich einer Schädigungskaskade entwickelt [14]. Sie geht auf eine Lösungsidee zurück, die einer der Autoren im Rahmen des BMWi-Projektes “Einfluss der Gammastrahlung auf die Schädigung von Reaktordruckbehältermaterialien und reaktordosimetrische Messungen” (Vorhaben-Nr.: 1501221) erarbeitet hat.

5 Ergebnisse

Die Ergebnisse wurden in technischen Berichten dokumentiert, die als Anhänge 1 bis 7 in diesem Bericht enthalten sind. Die Berichte der russischen Partner liegen in englischer Sprache vor. Das vorliegende Kapitel gibt eine ausführliche Zusammenfassung der technischen Berichte.

5.1 Modellierung der bestrahlungsinduzierten Erhöhung der Sprödbruchübergangstemperatur

Die Arbeiten zum AP1 wurden von den russischen Partnern durchgeführt. In den **Anhängen 1 und 2** ist für kubisch-raumzentrierte Metallgitter dargestellt, welcher analytische Zusammenhang zwischen der Entstehung von Versetzungsschleifen und der Spannungsverteilung in der Umgebung einer Rissspitze besteht. Für einen Mode I - Riss wird gezeigt, dass Energieschranke für die Entstehung einer Versetzungsschleife empfindlich von der Spannungsintensität abhängt. Für Spannungsintensitätsfaktoren $K_I > 0.43*K_{IC}$ entstehen spontane Versetzungsschleifen an der Rissspitze. Ferner wird der Einfluss von Hindernissen auf die Beweglichkeit von Versetzungen und damit auf die Ausbildung einer plastischen Zone an der Rissspitze analysiert. Es wird demonstriert, dass sich die an der Rissspitze entstehenden Versetzungen an dem Hindernis aufstauen. Als Hindernisse werden Punktdefekte betrachtet, wie sie auch durch Bestrahlung mit schnellen Neutronen entstehen. In Abhängigkeit der Rissbelastung K_I und der Entfernung des Hindernisses von der Rissspitze werden die Versetzungsdichte und das durch den Versetzungsstau verursachte Spannungsfeld berechnet.

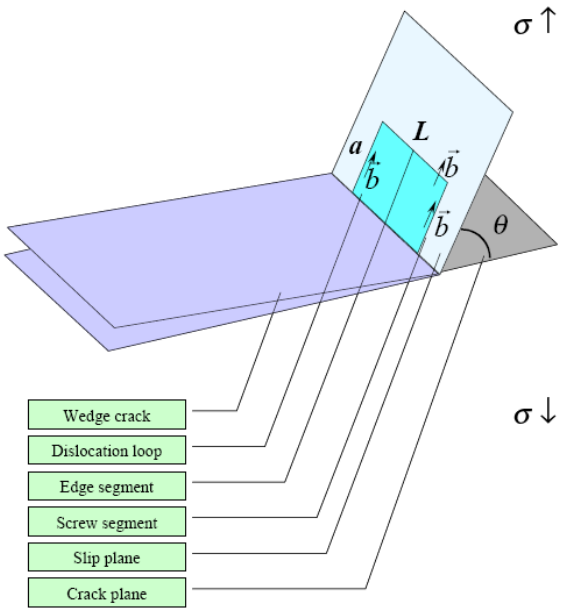

Bild 1: Geometrie zur Berechnung der Bildungsenergie einer Versetzungsschleife

Die Bildungsenergie einer Versetzungsschleife setzt sich aus folgenden Anteilen zusammen:

$$W_\Sigma = W_\sigma + W_i + 2W_f + W_l \qquad \textbf{Gl 1}$$

W_σ – Energie des Flankensegments der rechteckigen Versetzungsschleife im Spannungsfeld vor Rissspitze, W_i – Interaktionsenergie der Schraubensegmente der Versetzung, W_f – Bildungsenergie der eines Schraubensegmentes der Versetzungsschleife, W_l – Energie für die Bildung der Stufe

Zur Berechnung von W_σ wird die Schubspannungsverteilung in der Rissumgebung benötigt. Nach der linear-elastischen Bruchmechanik ergibt sich dafür:

$$\sigma_{r\theta} = K_I \cdot \frac{\sin(\theta)\cdot\cos(\theta/2)}{2\cdot\sqrt{2\pi\cdot r}} \qquad \textbf{Gl 2}$$

$K_I = \sigma_0 \cdot \sqrt{\pi \cdot a}$ ist der Spannungsintensitätsfaktor am Riss. Die maximale Schubspannung erhält man für θ = 70.5° Die von der Versetzung herrührenden Rückspannungen sind:

$$\sigma_{r\theta}^{b} = -\frac{G\cdot b}{1-\nu}\cdot\frac{\sin^2(\theta)\cdot\cos^2(\theta/2)}{4\cdot\pi\cdot r} \qquad \textbf{Gl 3}$$

wobei b der Betrag des Burgersvektors, G der Gleitmodul und ν die Querkontraktionszahl sind. Daraus ergibt sich W_σ zu:

$$W_\sigma = b\cdot L\cdot \int_{\xi_{np}\cdot b}^{a}\left[\sigma_{r\theta}+\sigma_{r\theta}^{b}\right]dr \qquad \textbf{Gl 4}$$

Dabei ist ξ_{np} ein Faktor zwischen 1 .... 10. Die untere Integrationsgrenze muss wegen der Singularität von Gl 2 und Gl 3 bei r = 0 ein Vielfaches des Burgersvektors betragen. Die Bildungsenergie der eines Schraubensegmentes der Versetzungsschleife ergibt sich aus:

$$W_i = \frac{G\cdot b^2\cdot a}{4\pi}\cdot\ln\left[\frac{a}{\xi_{pn}\,b}\right] \qquad \textbf{Gl 5}$$

und die Energie für die Bildung der Stufe aus:

$$W_l = b\cdot L\cdot\gamma \qquad \textbf{Gl 6}$$

Die Interaktionsenergie der Schraubensegmente der Versetzung ergibt sich aus:

$$W_i = \frac{G\cdot b^2\cdot a}{4\pi}\left\{\ln\frac{a+\sqrt{a^2+L^2}}{L}-\frac{2-\nu}{1-\nu}\cdot\left[\sqrt{1+\frac{L^2}{a^2}}-\frac{L}{a}\right]\right\} \qquad \textbf{Gl 7}$$

Das Bild 2 zeigt den Stau der an der Rissspitze emittierten Versetzungen an einem Hindernis. Dieses Hindernis kann z. B. ein bestrahlungsinduzierter Gitterdefekt sein. Der Bereich r = 0 ....r_0 wird auf Grund experimenteller Befunde als versetzungsfrei angenommen.

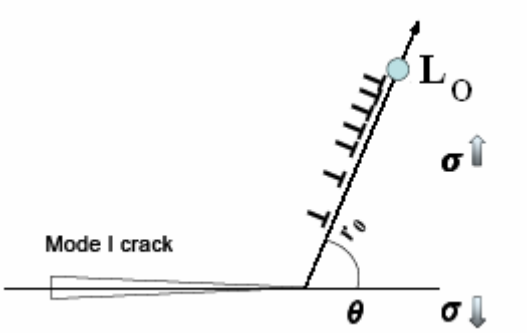

Bild 2: Versetzungsaufstau an einem Hindernis

Die Versetzungsdichte zwischen der Rissspitze und dem Hindernis ergibt sich nach folgender Beziehung:

$$\rho(r) = -\frac{2(1-\nu)}{\pi^2 \cdot G \cdot b} \cdot \sqrt{\frac{r - r_0}{L_O - r}} \cdot \int_{r_0}^{L_O} \sqrt{\frac{L_O - \xi}{\xi - r_0}} \cdot \frac{\sigma_{r\theta}(\xi)}{\xi - r} d\xi \qquad \textbf{Gl 8}$$

wobei $\sigma_{r\theta}$ nach Gl 2 für den entsprechenden Winkel θ einzusetzen ist. L_O ist der Abstand zwischen Hindernis und Rissspitze (Bild 2).

Das Integral in Gl 8 ist lösbar, wenn statt $\sigma_{r\theta}(r)$ die über den Radiusbereich r_0 ... L_O gemittelte Schubspannung $\langle \sigma_{r\theta} \rangle$ verwendet wird. Man erhält für die Versetzungsdichte:

$$\rho(r) = \frac{2 \cdot (1-\nu) \cdot K_I}{G \cdot b \cdot \left[\sqrt{L_O} + \sqrt{r_0}\right] \cdot \sqrt{2\pi}} \cdot \sqrt{\frac{r - r_0}{L_O - r}} \cdot \sin\theta \cdot \cos\left(\frac{\theta}{2}\right) \qquad \textbf{Gl 9}$$

Die Gesamtzahl der Versetzungen ergibt sich aus:

$$N = \int_{r_0}^{L_O} \rho(r) \cdot dr = \frac{\pi \cdot (1-\nu) \cdot K_I}{G \cdot b \cdot \sqrt{2\pi}} \cdot \sqrt{L_O} \cdot \left[1 - \sqrt{\frac{r_0}{L_O}}\right] \cdot \sin\theta \cdot \cos\left(\frac{\theta}{2}\right) \qquad \textbf{Gl 10}$$

Das Bild 3 stellt die Bildungsenergie einer Versetzungschleife über der Spannungsintensität dar. Diese Kurve erhält man durch Auswertung der Gleichungen 1 bis 7.

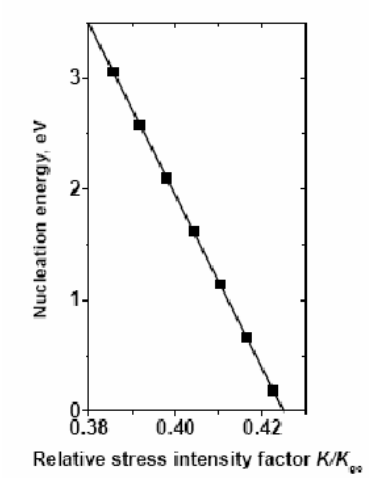

Bild 3: Bildungsenergie einer rechteckigen Versetzungsschleife über der relativen Spannungsintensität

Der effektive Spannungsintensitätsfaktor ergibt sich unter Berücksichtigung der Rückspannungen zu

$$K_\Sigma = K_I \cdot \left[1 - \sqrt{\frac{r_0}{L}}\right] \geq K_c \qquad \textbf{Gl 11}$$

K_c ist ein Schwellwert, ab dem spontan Versetzungsschleifen von der Rissspitze emittiert werden. Entsprechend Bild 3 gilt:

$$K_c \approx 0.43 \cdot K_{gc} = 0.43 \cdot \sqrt{\frac{4 \cdot G \cdot \gamma}{1-\nu}} \qquad \textbf{Gl 12}$$

mit: γ – freie Oberflächenenergie, K_{gc} – kritischer Spannungsintensitätsfaktor für Sprödbruch bei ideal sprödem Material (d. h. ohne Versetzungsbewegung). Gleichung 12 besagt unter anderem, dass in Eisen vor dem Bruch zumindest eine kleine plastische Verformung auftritt (quasi-sprödes Verhalten).

Das Spannungsfeld vor einem Aufstau von Versetzungen hängt von der externen Belastung, der Länge des Aufstaus, der Zahl der Versetzungen usw. ab. Die Schubspannung kann wie folgt abgeschätzt werden:

$$\sigma_H = 2 \cdot \sigma \cdot \sin(\theta) \cdot \cos(\theta/2) \cdot \sqrt{\frac{[L_O - r_0] \cdot \pi \cdot (1-\nu) \cdot \gamma}{G \cdot b^2}} \qquad \textbf{Gl 13}$$

Legt man die physikalischen Eigenschaften für kubisch-raumzentriertes Eisen zu Grunde (G = 82 GPa, γ = 2 J/m², ν = 0.29, b = 0.287 nm), so folgt aus Gl 10 unter Berücksichtigung von $1-\sqrt{r_0/L_O} \approx 0.43$ die Anzahl der Versetzungen zu $N \approx 32$ bei L_O = 1 µm, θ = 70.5° und K_I = 2.5 MPa$\sqrt{m}$. Die Schubspannung vor dem Aufstau ist ca. 20 mal größer als die externe Spannung σ.

Im **Anhang 3** werden Kerbschlagbiegeversuche an unbestrahlten RDB-Stählen fraktographisch ausgewertet mit dem Ziel, die erforderliche spezifische Energie für den Rissfortschritt bei verschiedenen Temperaturen zu bestimmen. Über die Beurteilung des Nutzens dieser Ergebnisse für die Entwicklung eines analytischen Modells für

den Spröd-duktil-Übergang konnte zwischen den russischen und den deutschen Partnern keine Einigkeit erzielt werden.

Im **Anhang 4** wird ein numerisches Modell entwickelt, das den Rissfortschritt in polykristallinen Eisenwerkstoffen unter Berücksichtigung der Kornstruktur des Gefüges beschreibt. Die numerische Simulation beruht auf der kinetischen Monte-Carlo Methode. Das Modell geht davon aus, dass der Rissfortschritt in einem polykristallinen Körper transkristallin von Korn zu Korn erfolgt. Ausgehend von der äußeren Belastung und der zufälligen Orientierung der Körner in der Umgebung der Rissfront wird dasjenige Korn ermittelt, das mit der höchsten Wahrscheinlichkeit als nächstes versagt. Als Kriterium zur Bestimmung der Orientierung des Rissfortschritts wird der Gradient der Verformungsenergie verwendet. Im Ergebnis liegt eine 3 dimensionale Bruchfläche vor. Das Höhenprofil der Bruchfläche ist vom Spannungszustand abhängig. Im Falle einer Scherbelastung bleibt die Rissfläche nahezu eben, während im Fall einer biaxialen Zugbeanspruchung eine starke Zerklüftung berechnet wird. Das Bild 4 zeigt die berechnete Bruchfläche für eine biaxiale Belastung ($\sigma_{zz} = 3\sigma_{xx}$).

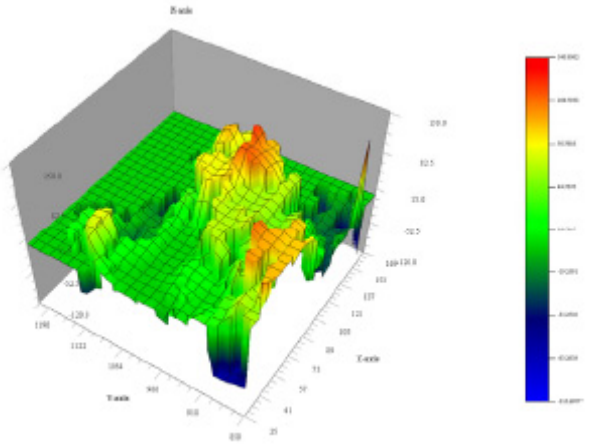

Bild 4: Simulierte Bruchfläche bei biaxialer Belastung

5.2 Untersuchung der Mikrostruktur von bestrahlten RDB-Stählen mit der Neutronenkleinwinkelstreuung

Das AP2 (SANS-Untersuchungen) wurde vom FZR bearbeitet. Die Ergebnisse sind im **Anhang 5** dargestellt. Es wurden Experimente mit der Neutronenkleinwinkelstreuung (small angle neutron scattering – SANS) an WWER-440 Grundwerkstoff, WWER-440 Schweißgut, an WWER-1000 Grundwerkstoff und an zwei Modelllegierungen durchgeführt und ausgewertet. Im Ergebnis liegen die Größenverteilungen und die Volumenanteile der strahleninduzierten Defekte für verschiedene Bestrahlungszustände (Fluenzen, Bestrahlungstemperaturen) vor. Anhand des so genannten A-Verhältnisses lassen sich zudem auch Aussagen über die Zusammensetzung der Defektcluster ableiten. Ferner wurde gezeigt, dass sich die strahleninduzierte Werkstoffschädigung durch Wärmebehandlung weitgehend wieder ausheilen lässt. Nach der thermischen Ausheilung ist der Werkstoff bei erneuter Bestrahlung weniger anfällig für strahleninduzierte Defekte.

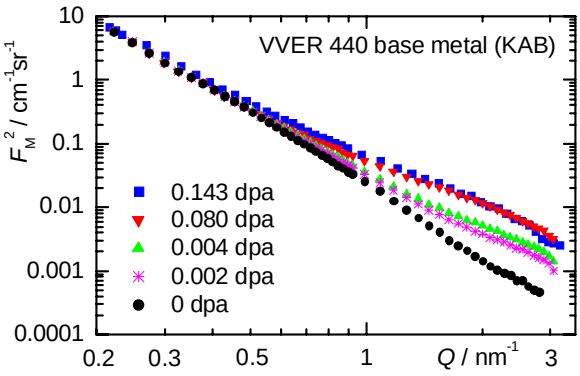

Bild 5: Magnetischer Sreuwirkungsquerschnitt für den Werkstoff 15Kh2MFA

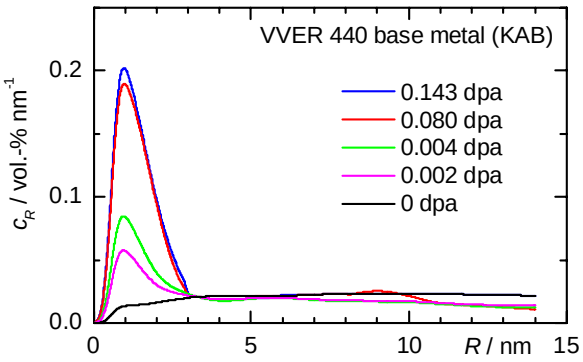

Bild 6: Volumenverteilungsfunktionen der Streuzentren berechnet aus den Kurvenverläufen der von Bild 5.

Das Bild 5 zeigt die Streukurven des Werkstoffs für 15Kh2MFA (Grundwerkstoff WWER-440) für verschiedene Bestrahlungszustände und Bild 6 die daraus ermittelten Größenverteilungsfunktionen für die bestrahlungsinduzierten Defekte.

Die Ergebnisse der SANS-Untersuchungen wurden mit der Änderung der mechanischen Eigenschaften (Härte, Streckgrenze und Sprödbruchübergangstemperatur) korreliert. Die Untersuchung der mechanischen Eigenschaften wurde außerhalb dieses Projekts durchgeführt.

Die Ergebnisse der SANS-Untersuchungen lassen sich wie folgt zusammenfassen:

- Nahezu unabhängig vom Werkstofftyp treten im wesentlichen Cluster mit Radien bis zu 3 nm auf. Ihr mittlerer Radius nach Strahlenbelastungen, welcher ein WWER-RDB-Stahl innerhalb seiner ausgelegten Gesamtbetriebszeit ausgesetzt ist, beträgt (1.0 ± 0.1) nm (Ausnahme Cu-reiche Eisenbasis-Modelllegierung ML-B).
- Der Volumenanteil an Clustern steigt mit der Strahlenbelastung monoton, aber im allgemeinen nicht linear an. Wegen der Konstanz des Clusterradius trifft diese Aussage auch auf die Anzahldichte zu. In Abhängigkeit von der chemischen Zusammensetzung der Werkstoffe wurden bei vergleichbarer Strahlenbelastung deutliche Unterschiede im Volumenanteil festgestellt.
- Der Cu-Gehalt der Werkstoffe beeinflusst den Volumenanteil an bestrahlungsinduzierten Clustern am stärksten, was die besondere Rolle dieses Elements bei der bestrahlungsbedingten Materialalterung bestätigt.
- Mindestens zwei Typen von Leerstellen/Fremdatom-Clustern wurden identifiziert, die sich in ihrer Zusammensetzung und ihrer Bildungskinetik unterscheiden. Das Vorliegen von reinen Cu-Ausscheidungen kann definitiv ausgeschlossen werden.
- Eine Wärmebehandlung oberhalb der Bestrahlungstemperatur reduziert den Volumenanteil an bestrahlungsinduzierten Clustern, oftmals bis hin zu deren vollständiger Auflösung.
- Bei relativ hohen Cu-Gehalten der Werkstoffe (über 0.2 Masse-%) tritt bei Ausheilwärmebehandlungen eine Vergröberung von Clustern in Konkurrenz zu deren Auflösung.

- Eine Ausheilwärmebehandlung beeinflusst die Strahlenanfälligkeit der Werkstoffe bei Wiederbestrahlung. Nach der Wärmebehandlung wurde bei erneuter Bestrahlung mit schnellen Neutronen eine geringere Strahlenanfälligkeit in Bezug auf die Anteil der im Werkstoff neu gebildeten Defekte festgestellt.

5.3 Modellierung der bestrahlungsinduzierten Gitterdefekte in kubisch raumzentriertem Eisen

Das AP3 wurde von den russischen Partnern bearbeitet. Im **Anhang 6** werden die Grundlagen eines numerischen Programms zur Simulation der Strahlendefekte auf der Nanometerskala beschrieben. Das Programm beruht auf der LKMC-Methode (LKMC – Lattice Kinetic Monte Carlo). Es wird die Diffusion von Cu-Atomen und Leerstellen in einer kubisch-raumzentrierten Eisenmatrix untersucht. Basierend auf interatomaren Bindungsenergien und Wechselwirkungsenergien werden die Sprungwahrscheinlichkeiten für Platzwechselvorgänge auf den Gitterplätzen berechnet.

Die Frequenz von Platzwechselvorgängen wird mit einer Arrhenius-Gleichung beschrieben:

$$P = P_0 \cdot \exp\left[-\left(E_{sp} - E_{in}\right)/kT\right] \qquad \textbf{Gl 14}$$

Dabei ist P_0 eine Konstante (Einheit s^{-1}), E_{sp} ist die Energie eines Atomsystems in der Sattelpunktkonfiguration (Energiemaximum während des Platzwechselvorgangs), E_{in} ist die Energie des Atomsystems vor dem Platzwechselvorgang und $k \cdot T$ sind die Boltzmannkonstante und die absolute Temperatur. Die Eingabeparameter P_0, E_{sp} und E_{in} hängen nicht nur von den am Platzwechsel beteiligten Atomen ab, sondern auch von deren näherer Umgebung. Die Tabelle 5-1 gibt eine Übersicht zu den Eingabeparametern, die zur Berechnung der Platzwechselfrequenzen benötigt werden.

Tabelle 5-1: Energieparameter verschiedener Defekte in kubisch-raumzentriertem Eisen

Parameter	Wert in eV
Bildungsenergie für Leerstellen (vacancies – V)	1.28
Migrationsenergie für Leerstellen in der Eisenmatrix	0.65
Cu-Atom Entmischungsenergie in Eisen	0.59
V-Cu Austauschbarriere	0.53
Bindungsenergie für 2 V in nächster Nachbarschaft	0.14
Bindungsenergie für 2 V in zweitnächster Nachbarschaft	0.28
Bindungsenergie für 2 V in drittnächster Nachbarschaft	-0.02
Bindungsenergie Cu-V in nächster Nachbarschaft	0.17
Bindungsenergie Cu-V in zweitnächster Nachbarschaft	0.19
Bindungsenergie Cu-V in drittnächster Nachbarschaft	0.04
Bindungsenergie Cu-Cu in nächster Nachbarschaft	0.14
Bindungsenergie Cu-Cu in zweitnächster Nachbarschaft	0.03
Bindungsenergie Cu-Cu in drittnächster Nachbarschaft	-0.01

Es wird eine Simulationszelle von ca. 500 000 Gitterplätzen mit periodischen Randbedingungen verwendet (Bild 7). Die Ausgangssituation für die Simulation ist durch den Zustand nach einer Stoßkaskade gegeben, die ihrerseits durch eine PKA (primary knock-on atom) ausgelöst wird. Da die Strahlendosis in den RDB von LWR einen Wert von 0.15 dpa nicht überschreitet, kann man annehmen, dass sich die Stoßkaskaden nicht überlappen. Die Kaskaden können daher unabhängig voneinander untersucht werden. Bei den Berechnungen wird angenommen, dass die Cu-Atome und die Leerstellen die Gitterplätze der Eisenmatrix einnehmen.

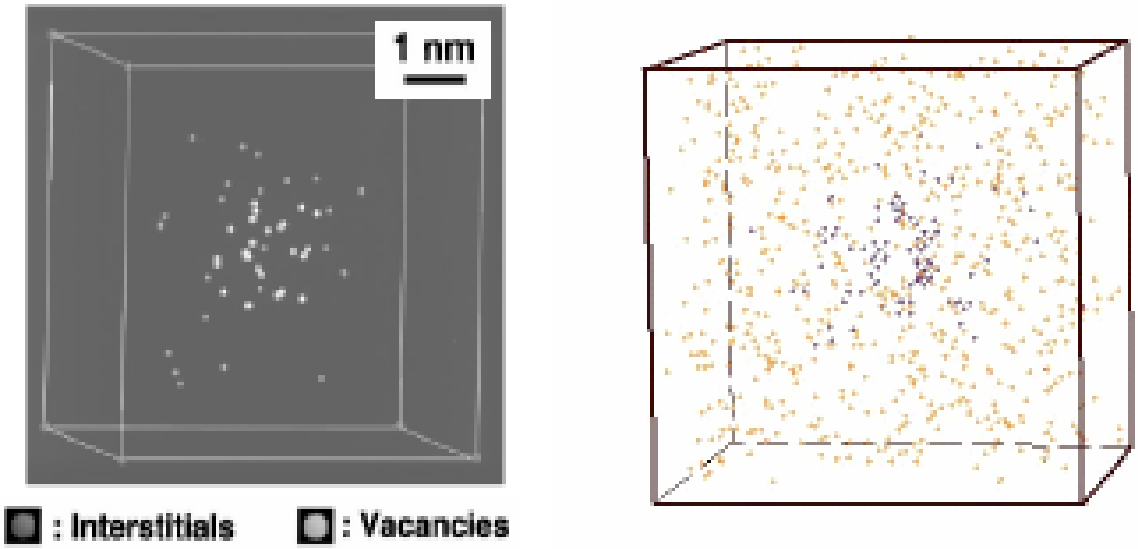

Bild 7: Links: Typische Konfiguration von Strahlendefekten nach einer Stoßkaskade (Ergebnis einer molekulardynamischen Simulation); rechts: Verteilung der Cu-Atome (gelb) und Leerstellen (dunkel) in einer LKMC-Simulationszelle

Im **Anhang 7** sind die Ergebnisse von Simulationsrechnungen mit dem LKMC-Code beschrieben. Es wurden Sensitivitätsstudien zum Einfluss des Cu-Gehalts auf die Stabilität von Defekt-Clustern durchgeführt. Die Berechnungen zeigen, dass die Anwesenheit von Cu-Atomen zur Bildung von langlebigen Defekten führt. Dabei werden die Leerstellen in Cu/Leerstellen-Cluster eingefangen. Leerstellen in reinem Eisen sind bei Bestrahlungstemperaturen von 270 °C dagegen nicht stabil, die Lebensdauer liegt zwischen 10^{-2} s und 1 s. Die kritische Cu-Konzentration, ab welcher stabile Defekte entstehen, beträgt ca. 0.1 Masse%. Das Rechenprogramm erlaubt neben der Untersuchung der Diffusionsvorgänge auch die Simulation von Streukurven, die auch bei SANS-Messungen anfallen (vgl. AP2, Anhang 5). Es besteht eine qualitative Übereinstimmung der experimentellen Streukurven und der Einhüllenden der simulierten Streukurven.

Im Bild 8 ist dargestellt, wie ein Leerstellencluster in reinem Eisen nach der Stoßkaskade innerhalb von ca. 1 s aufgelöst wird. Die Kinetik der Auflösung hängt von der initialen Konfiguration der Cluster ab. Die Zeit von einer Sekunde stellt eine obere Grenze für die Überlebenszeit reiner Leerstellencluster in reinem Eisen dar.

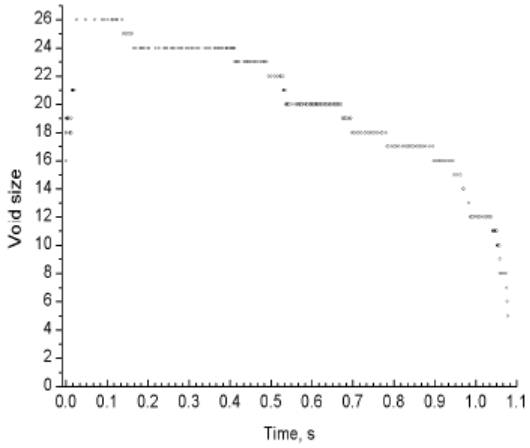

Bild 8: Kinetik der Entstehung und Erholung eines Leerstellenclusters nach einer Stoßkaskade

Bild 9 zeigt für einen hohen Cu-Anteil (1%) in der Eisenmatrix die räumliche Verteilung der Cu-V-Cluster. Es zeigt sich, dass sich die verteilten Cu-Atomen zu größeren Clustern vereinen und dass sich die Leerstellen an die größeren Cu-Cluster anlagern. Cluster von bis zu 7 bis 10 Cu-Atomen sind zusammen mit einer Leerstelle noch beweglich. Bei weiterem Wachstum werden sie unbeweglich und sind hinreichend stabil um über größerer Zeiträume hinweg zu überleben

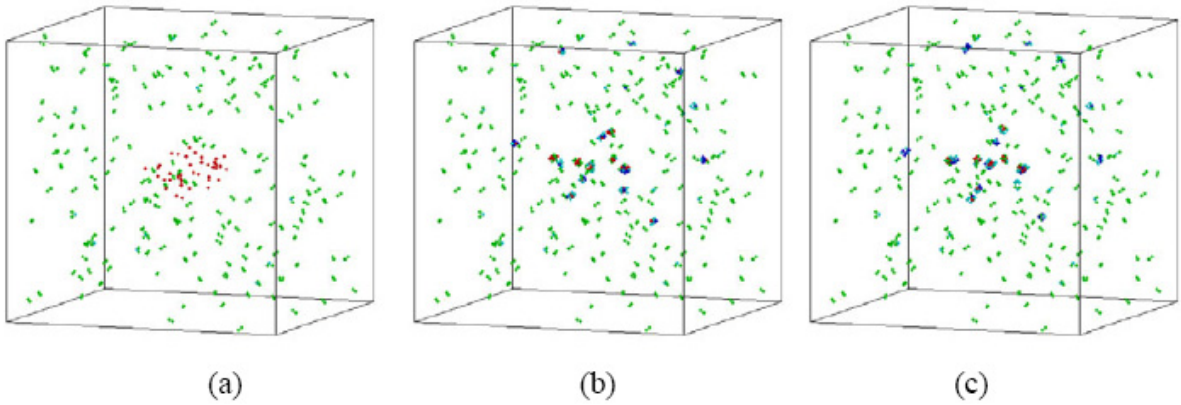

Bild 9: Abfolge von räumlichen Verteilungen von Cu-V-Clustern während der Kaskadenerholung für 1at% Cu; a) anfänglich, b) nach ca. 2.5 ms, c) nach ca. 10 ms; rot: Leerstellen, grün: 2Cu (Dimere), blau: nCu (n>2, Cu-Cluster); Cu-Monomere sind nicht dargestellt

Die Beweglichkeit von 1V-7Cu-Clustern ist eine wichtige Eingangsinformation für die Langzeitvorhersage der Defektdichte mit ratentheoretischen Modellen.

Das Bild 10 zeigt die Streukurven, die sich aus der berechneten Clusterverteilung ergeben. Diese Streukurven können mit SANS-Messungen verglichen werden.

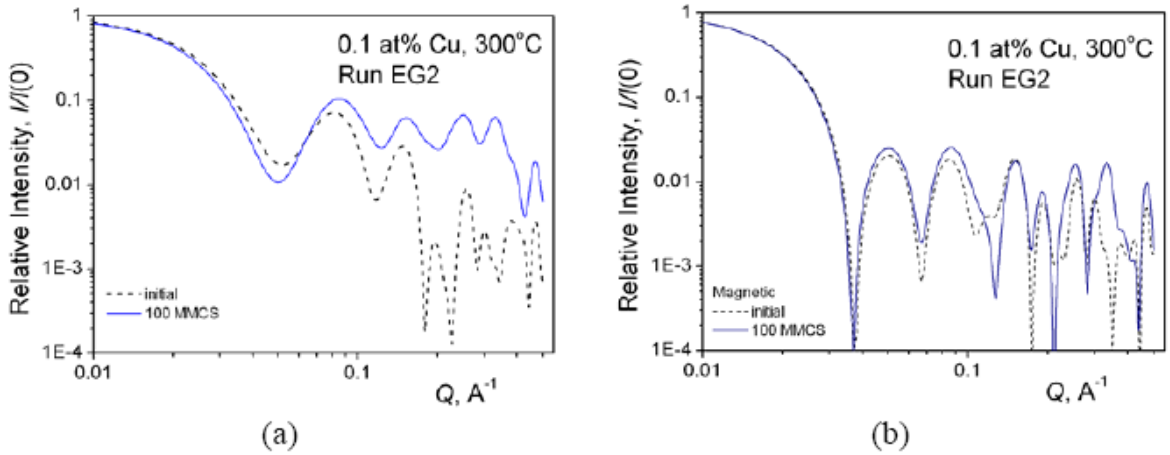

Bild 10: Simuliertes SANS-Signal, berechnetes aus den Vakanzen und Cu-Atomen einer LKMC-Simulationszelle; a) Berechnung aus den Kernstreulängen von Fe und Cu; b) Berechnung aus den magnetischen Streulängen von Fe und Cu; gestrichelte Kurven: initiale Verteilung, durchgezogene Kurven: nach 10^8 MC-Schritten

6 Zusammenfassung und Ausblick

Um den Einfluss von bestrahlungsinduzierten Gitterdefekten auf die mechanischen Eigenschaften zu ermitteln, wurden analytische Berechnungen zum Einfluss von Hindernissen auf die Beweglichkeit von Versetzungen und damit auf die Ausbildung einer plastischen Zone an der Rissspitze durchgeführt. Es wird demonstriert, dass sich die an der Rissspitze entstehenden Versetzungen an dem Hindernis (bestrahlungsinduzierte Punktdefekte) aufstauen. In Abhängigkeit der Rissbelastung K_I und der Entfernung des Hindernisses von der Rissspitze werden die Versetzungsdichte und das durch den Versetzungsstau verursachte Spannungsfeld berechnet.

Mit Hilfe von SANS-Experimente an verschiedenen WWER-Stählen und Modelllegierungen wurden Größenverteilungen und die Volumenanteile der strahleninduzierten Defekte für verschiedene Bestrahlungszustände (Fluenzen, Bestrahlungstemperaturen) ermittelt. Es wurde gezeigt, dass sich die strahleninduzierte Werkstoffschädigung durch Wärmebehandlung weitgehend wieder ausheilen lässt. Nach der thermischen Ausheilung ist der Werkstoff bei erneuter Bestrahlung weniger anfällig für strahleninduzierte Defekte. Die Ergebnisse der SANS-Untersuchungen wurden mit der Änderung der mechanischen Eigenschaften (Härte, Streckgrenze und Sprödbruchübergangstemperatur) korreliert.

Mit der kinetischen Gitter-Monte-Carlo-Methode wurden numerische Sensitivitätsstudien zum Einfluss des Cu-Gehalts auf die Stabilität von Defekt-Clustern durchgeführt. Die Berechnungen zeigen, dass die Anwesenheit von Cu-Atomen zur Bildung von langlebigen Defekten führt. Dabei werden Leerstellen in Cu/Leerstellen-Cluster eingefangen. Leerstellen in reinem Eisen sind bei Bestrahlungstemperaturen von 270 °C dagegen nicht stabil, die Lebensdauer liegt zwischen 10^{-2} s und 1 s. Die kritische Cu-Konzentration, ab welcher stabile Defekte entstehen, beträgt ca. 0.1 Masseprozent.

Das bearbeitete Vorhaben diente zur Erweiterung des Kenntnisstands der sicherheitsrelevanten Versprödung des Reaktordruckbehälters. Es wurde ein Beitrag geleistet zur Modellierung der Änderung der mechanischen Eigenschaften als Folge strahleninduzierter mikrostruktureller Defekte. Es handelt sich hierbei um ein Gebiet, auf dem zur Zeit international sehr intensiv geforscht (z. B. EU-Projekt PERFECT)

wird. Die neutronenbestrahlungsinduzierte Minderung der Bruchzähigkeit bzw. Verschiebung der Spröd-duktil-Übergangstemperatur von RDB-Stählen ist ein komplexes Multiskalenphänomen mit zahlreichen offenen Fragen. Insbesondere auf der Nanometer- und Mikrometerskala wird international versucht, physikalisch begründete Zusammenhänge zwischen den Strahlendefekten und den mechanischen Eigenschaften zu ermitteln und die Berechnungsmodelle schrittweise für die Anwendung auf reale Stähle zu ertüchtigen. Das Vorhaben stellt einen Betrag zu diesen Bemühungen dar. Die aufgeworfenen Fragen sind nicht restlos beantwortet. Es sind weiterführende Untersuchungen erforderlich, in denen die Ergebnisse des Vorhabens nutzbringend verwendet werden können.

Die physikalische Modellierung der Defektkinetik in einer kubisch-raumzentrierten Eisenmatrix erlaubt derzeit noch nicht die Berücksichtigung aller wesentlichen Legierungselemente von typischen RDB-Stählen. Daher kann auch deren Einfluss auf die Versprödung (Verschiebung der Sprödbruchübergangstemperatur) modellmäßig nicht erfasst werden. Wohl aber lässt sich dieser Einfluss mit empirischen Korrelationen beschreiben, die aus den SANS-Untersuchungen einerseits und bruchmechanischen Experimenten andererseits abgeleitet werden.

7 Literatur

[1] G.R. Odette: Radiation Induced Microstructural Evolution in Reactor Pressure Vessel Steels, Mat. Res. Soc. Symp. Proc. Vol. 373 (1995) 137-148

[2] G.R. Odette, C.L. Liu, B.D. Wirth: On the Composition and Structure of Nanoprecipitates in Irradiated Pressure Vessel Steels, Mat. Res. Soc. Symp. Proc. Vol. 439 (1997) 457-469

[3] G.R. Odette, G.E.Lucas: Recent Progress in Understanding Reactor Pressure Vessel Steel Embrittlement, Radiation Effects&Defects in Solids, 144 (1998) 189-231

[4] G.R.Odette, B.D. Wirth, D.J. Bacon, N.M. Ghoniem: Multiscale-Multiphysics Modeling of Radiation-Damaged Materials: Embrittlement of Pressure Vessel Steels, MRS Bulletin, March 2001, 178-181

[5] Berichte über vom Bundesministerium für Wirtschaft und Technologie geförderte Forschungsvorhaben auf dem Gebiet der Reaktorsicherheit, Fortschrittsbericht, Gesellschaft für Anlagen- und Reaktorsicherheit (GRS)mbH, Berichte zum Vorhaben-Nr. 1501012, GRS-F-1/1996 - GRS-F-2/2000

[6] H.-W. Viehrig, H. Richter: Untersuchung des Zusammenhanges zwischen bruchmechanischen und mechanisch-technologischen Kennwerten bei bestrahlten Reaktordruckbehälterstählen, Reaktorsicherheitsforschung, Vorhaben-Nr.: 1500919, Abschlussbericht, April 2000, FZR- FWSM - 6/2000

[7] H.-W. Viehrig, J. Böhmert, H. Richter: Common German/Russia Irradiation Experiment at Rheinsberg NPP-Results of the Mechanical Testing,, Proc., IAEA Spec. Meeting, Madrid, IWG-LMNPP-99/2, 271-282

[8] H.-W. Viehrig, J. Böhmert, J. Dzugan, H. Richter: Master Curve Evalution of Irradiated Russian VVER Type Reactor Pressure Vessel Steels, 20th International Symp. on Radiation Effects on Materials, ASTM STP 1405, S.T. Rosinski et al. (Eds.), Consh., PA, 2001, 109

[9] H.-W, Viehrig, J. Böhmert, J. Dzugan: Beitrag zur Bewertung des Bestrahlungsverhaltens russischer WWER-Reaktordruckbehälterstähle, 26. MPA-Seminar “Sicherheit und Verfügbarkeit in der Energietechnik”, Staatliche Materialprüfanstalt Stuttgart, 2000, Sammelband, 20.1-20.20

[10] J. Böhmert, A. Kruykov, Yu.A. Nikolaev, Yu.N. Korolev, D.Yu. Erak, S.S. Gerashenko: Ursachen der Versprödung von WWER-440-Reaktordruckbehälter. Reaktorsicherheitsforschung, Vorhaben-Nr.:1501020, Abschlussbericht, Dez. 1998

[11] J. Böhmert, M. Große, A.Kruykov, Yu.A. Nikolaev, D.Yu. Erak, A. Ulbricht: Composition Effects on the Radiation Embrittlement of Iron Alloys. 20th Intern. Symp on Radiation Effects on Materials, ASTM-STP 1405, S.T. Rosinski et al. (Eds.), Consh., PA, 2001, 383

[12] V.A. Borodin, V.M. Manichev: The Effect of Internal Stress Fields on Fracture of Structural Materials under Irradiation. J. Nucl. Mat. 225 (1995) 33

[13] R.E. Voskoboinikov: Degradation of Mechanical Properties of Structural Reactor Materials Induced by Formation on Stress Concentrators. J. Nucl. Mat. 270 (1999) 309

[14] P. Vladimirov, V.A. Borodin: Evolution of Copper Precipitates in Stressed Materials. Paper on the 10th International Conference on Fusion Reactor Materials, Oct. 2001, Baden-Baden

Analytical Description of Brittle-to-Ductile Transition in bcc Metals.

Nucleation of dislocation loop at the crack tip

Roman E. Voskoboinikov

Dresden 2001

Abstract

Nucleation of dislocation loop at the crack tip in a material subjected to uniaxial loading is investigated. Analytical expression for the total energy of rectangular dislocation loop at the crack tip is found. Dependence of the nucleation energy barrier on dislocation loop shape and stress intensity factor at the crack tip is determined. It is established that the energetic barrier for dislocation loop nucleation strongly depends on the stress intensity factor. Nucleation of dislocation loop is very sensitive to structural environment (forest dislocations, precipitates, clusters of point defects, *etc*) modifying stress field at the crack tip.

Keywords: dislocation; crack; mode I loading; stress intensity factor; ductile-to-brittle transition; energetic barrier for nucleation.

PACS: 62.20.Mk; 81.40.Np; 46.30.Nz

1 Introduction and overview

The ductile-to-brittle transition (DBT) is a classic phenomenon exhibited by almost all materials with *possible* exception of fcc metals. The change in fracture behaviour from (quasi)brittle cleavage to ductile failure is always accompanied by significant increase of dislocation density at the near crack surface region [1]. A number of experimental observations unambiguously demonstrates cold-working of crack surfaces due to nucleation of dislocations at the crack tip [1, 2].

There are two possible ways of energy release from the crack tip region during the fracture process. The first one is formation of a new surface that results in crack growth. The second one is the local plastic flow at the near crack tip region. There are two time scales involved. Depending on the relation between typical time of crack growth (τ_{cr}) and typical time of deformation (τ_d) one of the following limiting cases can be realized. Provided typical time of crack surface formation is significantly less than that of deformation ($\tau_{cr} \ll \tau_d$) brittle cleavage of material occurs. Comparable time scales ($\tau_{cr} \simeq \tau_d$) result in ductile failure. High deformation rate at the crack tip region ($\tau_{cr} \gg \tau_d$) leads to crack arrest when any energy absorbed by solid is dissipated through local plastic deformation at the crack tip.

In order to establish particular process taking place one should estimate typical times. Assuming that typical time of crack growth is independent on the structural environment evolution and is taken into consideration as an external parameter the typical time of deformation is evaluated. It consists of the time of dislocation nucleation (τ_f) and the time of dislocation motion (τ_m):

$$\tau_d = \tau_f + \tau_m. \tag{1}$$

So, in the existing models DBT is considered either as a competition between crack propagation and thermally activated generation of a dislocation (assumption $\tau_f \gg \tau_m$) [3]-[6] or as a thermally activated motion of dislocation (assumption $\tau_f \ll \tau_m$) [7, 8]. The latter limiting case is realized in covalent crystals (*e.g.* in silicon) where temperature dependent dislocation motion occurs at temperature range up to the melting point. The former case is more appropriate for metals at relevant temperatures because of athermal pattern of dislocation motion at DBT temperature range.

According to general approaches of statistical mechanics typical time of the process (τ_d) is connected with appropriate activation energy (W_Σ) through Arrehnius dependence:

$$\tau_d \sim \exp\left(-\frac{W_\Sigma}{kT}\right). \tag{2}$$

So, the aim of current consideration comes to evaluation of the nucleation energetic barrier for dislocation at the crack tip.

2 Recent models

2.1 2D model of equilibrium of edge dislocation at the crack tip

Equilibrium of edge dislocation at the crack tip region is considered within two dimensional geometry (plain strain) in the framework of force balance approach [4]. Material with crack is subjected to mode I loading in the direction normal to the crack plane. Edge dislocation is set at the distance r from the crack tip. Slip plane of dislocation makes angle θ with the crack plane, see fig.1.

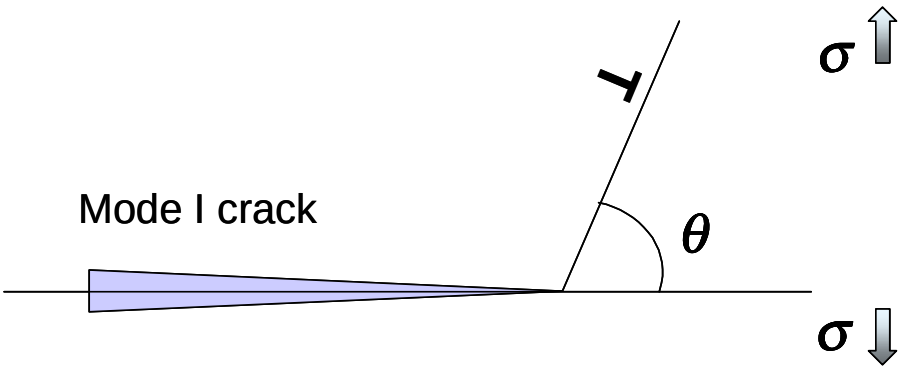

Figure 1: Geometry of 2D approach to evaluation of equilibrium position of edge dislocation emitted by mode I crack.

The equilibrium position for the edge dislocation comes from the force balance between the stress field from the crack tip that pushes dislocation away and the mirror forces from free surface of the crack that attract dislocation back to the

surface. The main drawback of this approach is related to the geometry applied. Two dimensional consideration supposes infinite solid, crack and edge dislocation in the direction normal to the plane of figure 1. Therefore, the total energy of the edge dislocation is also infinite. It means that infinite dislocation cannot be emitted from the crack tip by thermal fluctuations.

2.2 3D model of dislocation loop generation from a crack tip

Advanced model of dislocation loop nucleation at the crack tip has been proposed recently [5]. Material with crack is subjected to mode II loading in the direction parallel to the plane of crack. Circular dislocation loop is nucleated at the crack tip. Slip plane of the dislocation coincides with crack plane, see figure 2.

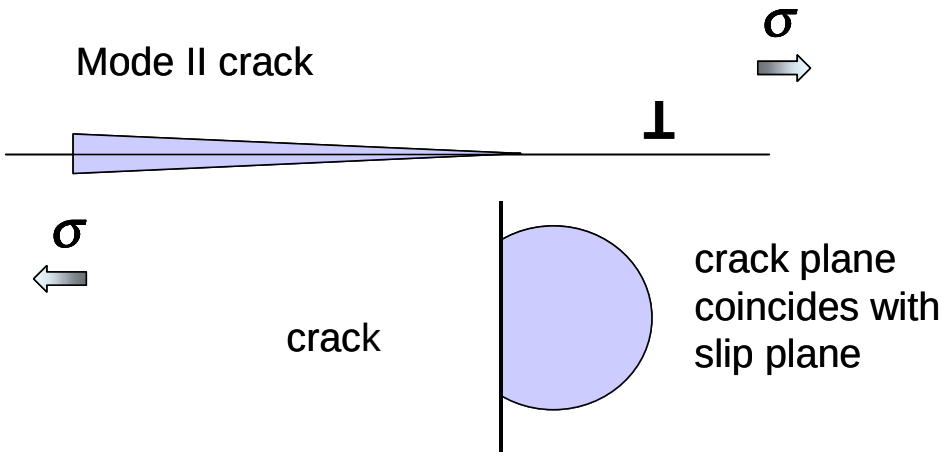

Figure 2: Geometry of 3D approach to evaluation of the energy of circular dislocation loop emitted by mode II crack.

Nucleation energy barrier for circular dislocation loop formation at the crack tip region has finite value. However, the circular shape of the loop can be less preferable from the energetic point of view in comparison with *e.g.* rectangular one.

3 Nucleation of dislocation loop at the crack tip

Within the general problem of ductile-to-brittle transition we propose to consider nucleation of rectangular dislocation loop at the crack tip. Geometry of the problem is shown in figure 3. Material with wedge crack is loaded with external stress σ normal to the crack surface. Rectangular dislocation loop with height a (pure screw segments) and width L (pure edge segment) is nucleated at the crack tip. Slip plane of the loop makes angle θ with the plane of the crack. The most preferable direction of the loop nucleation is determined by the maximum of actual stress and should be established within the problem treatment.

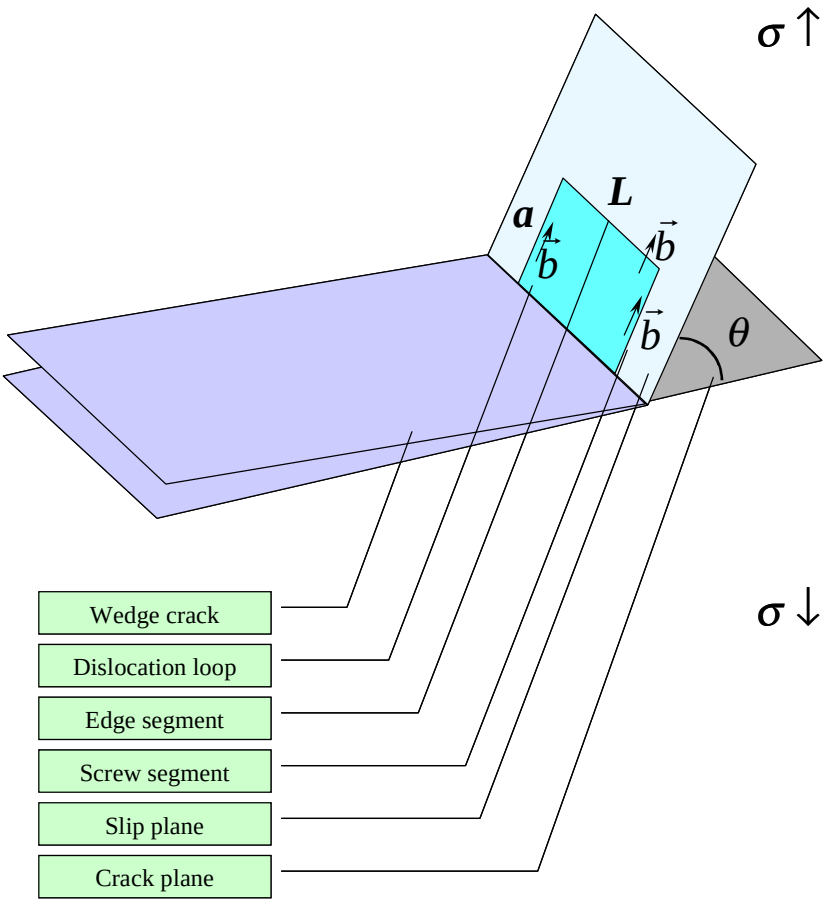

Figure 3: Geometry of the suggested approach to evaluation of nucleation energy of dislocation loop at the crack tip.

Total energy of dislocation loop at the crack tip includes several terms:

$$W_\Sigma = W_\sigma + W_l + 2W_f + W_i, \tag{3}$$

where W_σ is the energy of the edge segment of rectangular dislocation loop in the actual stress field; W_l is the energy of ledge formation; W_f is formation energy of a screw segment of rectangular dislocation loop and W_i is the energy of interaction of the screw segments of the loop.

In order to calculate the first term of Eq.3 the actual stress field and the most preferable direction of loop nucleation have to be found.

Asymptotic behavior of shear stress $\sigma^c_{r\theta}(r,\theta)$ at the crack tip region is given by the following relation [9]:

$$\sigma^c_{r\theta}(r,\theta) = \frac{K_I}{\sqrt{\pi r}} \sin\theta \cos\frac{\theta}{2}. \tag{4}$$

Dependence of $\sigma^c_{r\theta}$ is shown in fig.4 and appropriate contour plot is given in fig.5.

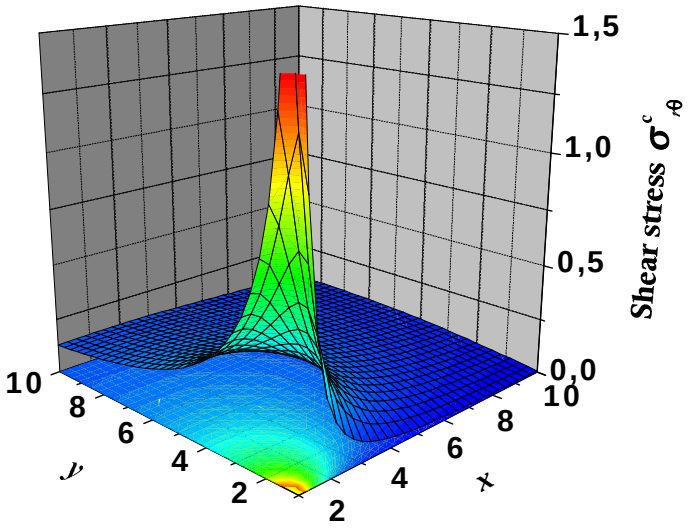

Figure 4: 3D shear stress.

Mirror forces $\sigma^m_{r\theta}(r,\theta)$ from the crack surface act on the edge dislocation and attract it back to the crack. The value of mirror forces (per unit length) versus edge

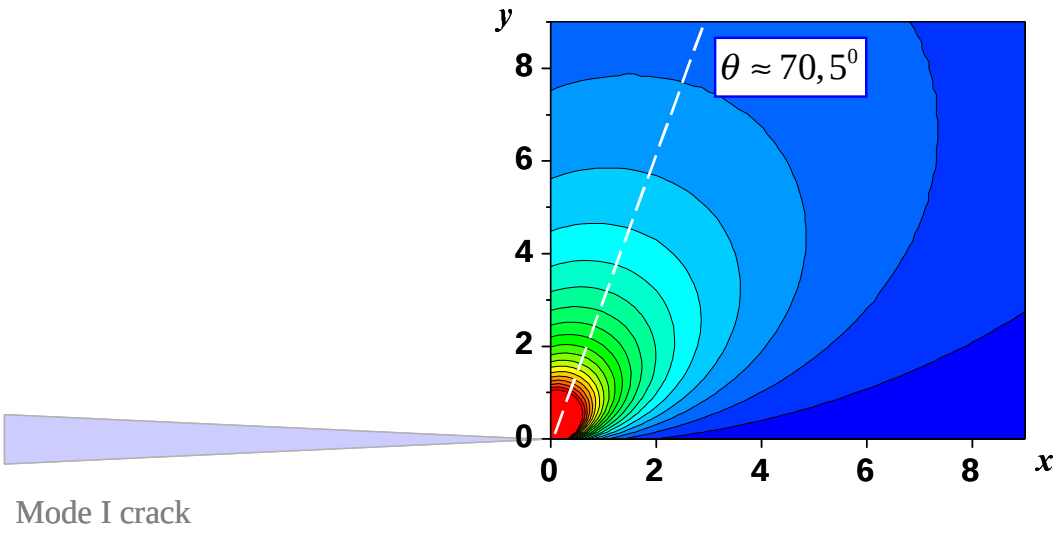

Figure 5: Shear stress contour plot.

dislocation position is given by the following relation [9]:

$$\sigma_{r\theta}^{m}(r,\theta) = \frac{L_I}{\sqrt{\pi r}} \sin\theta \cos\frac{\theta}{2}, \tag{5}$$

where

$$L_I = -\frac{b\mu}{2(1-\nu)\sqrt{\pi r}} \sin\theta \cos\frac{\theta}{2}. \tag{6}$$

Dependence of $\sigma_{r\theta}^{m}(r,\theta)$ is shown in fig.6 and appropriate contour plot is given in fig.7. The dependence is more sharp than $\sigma_{r\theta}^{c}(r,\theta)$, and $\sigma_{r\theta}^{m}(r,\theta)$ quickly decreases with increase of the distance r from the crack tip.

The energy of the edge segment of dislocation loop in the actual stress field in the crack vicinity is equal to:

$$W_\sigma = bL \int_{\xi_{pn} b}^{a} \left(\sigma_{r\theta}^{c} + \sigma_{r\theta}^{m}\right) dr = \frac{\mu b^3 L}{2\pi b} \left[\frac{4\sqrt{\pi} K_I}{\mu\sqrt{b}} \left(\sqrt{\frac{a}{b}} - \sqrt{\xi_{pn}} \right) - \frac{\sin\theta\cos\frac{\theta}{2}}{1-\nu} \ln\frac{a}{e\left(\xi_{pn} b\right)} \right] \tag{7}$$

The energy of ledge formation is given by the following relation:

$$W_l = bL\gamma \tag{8}$$

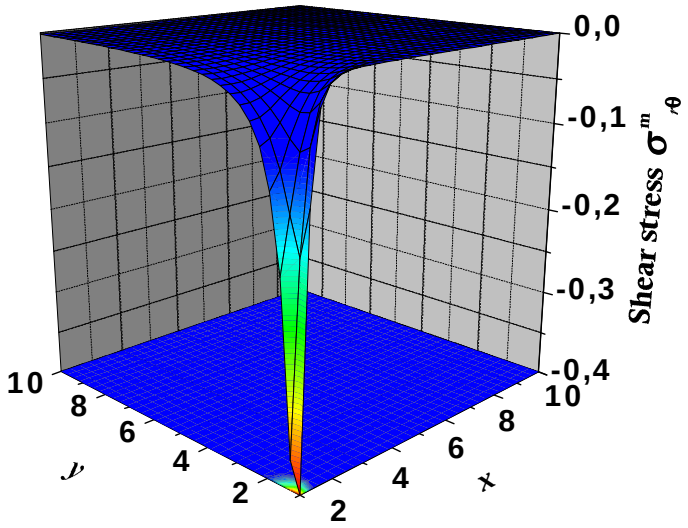

Figure 6: 3D mirror stress.

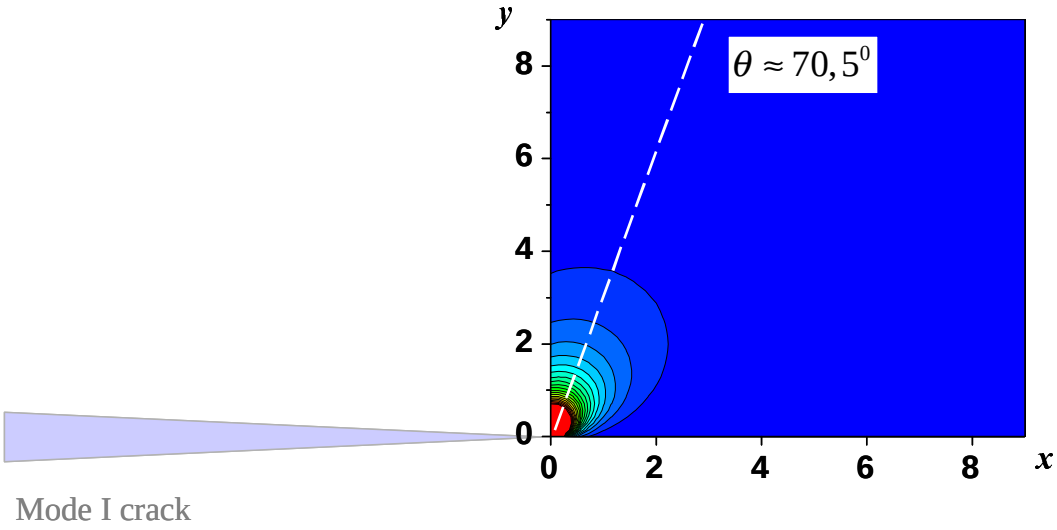

Figure 7: Mirror stress contour plot.

The energy of formation of screw segments of the dislocation loop is equal to [10]

$$W_f = \frac{\mu b^2 a}{4\pi} \ln \frac{a}{e\,(\xi_{pn} b)}. \tag{9}$$

And the energy of interaction of screw segments of the dislocation loop is given by [10, 11]

$$W_i = \frac{\mu b^2 a}{4\pi}\left\{\ln\frac{a+\sqrt{L^2+a^2}}{L} - \frac{2-\nu}{1-\nu}\left[\sqrt{1+\frac{L^2}{a^2}} - \frac{L}{a}\right]\right\}. \qquad (10)$$

4 Nucleation energy barrier

The energy of the formation of rectangular dislocation loop (3) *vs* its height (a) and width (L) for stress intensity factor $K_I = 0.4K_{gc}$ is shown in figure 8.

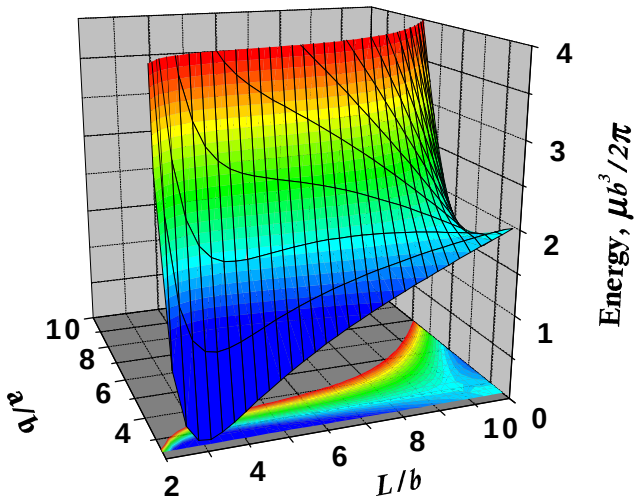

Figure 8: Formation energy of rectangular dislocation loop at the crack tip (no nucleation).

Substitution of typical values of iron into Eq.3 results in the nucleation energy barrier (the energy corresponding to the saddle point of the surface) of the order of several eV. So, there is no nucleation of dislocation at this level of stress concentration at the crack tip.

Small increase of the stress intensity factor up to $K_I = 0.42K_{gc}$ leads to significant decrease of the nucleation barrier to the value of approximately 0.8 eV. Appropriate dependence of the total energy is shown in figure 9.

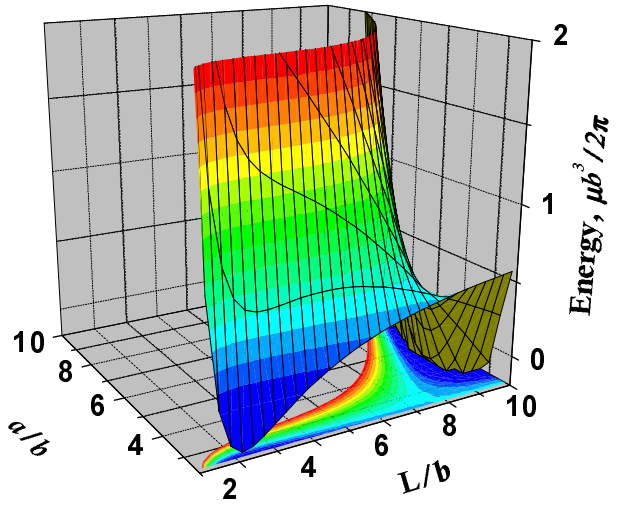

Figure 9: Formation energy of rectangular dislocation loop at the crack tip (nucleation through thermal fluctuations). Stress intensity factor $K_I = 0.42K_{gc}$.

Further increase of actual stress intensity factor results in disappearance of the nucleation barrier, see fig. 10, and therefore spontaneous nucleation of dislocation loops at the crack tip occurs.

5 Discussion

Investigation of dislocation loop nucleation at the mode II crack tip within Peierls concept proposed by J.P.Rice [5] gives stress intensity factor of $K_{II} = 0.9K_{gc}$ leading to spontaneous dislocation loop nucleation. Our consideration results in approximately two times less value: $K_I \approx 0.43K_{gc}$. With the exception of loading geometry the main difference of the suggested approach in comparison with that of J.P.Rice is in the shape of emitted loop. 3D model [5] proposed by J.P.Rice suggests circular shape of the loop with one describing parameter (dislocation loop radius R) whereas rectangular dislocation loop with "width" a and "length" L is proposed in the current model. It is obvious, that this particular scheme allows to generate more preferable loop configuration from the energetic point of view.

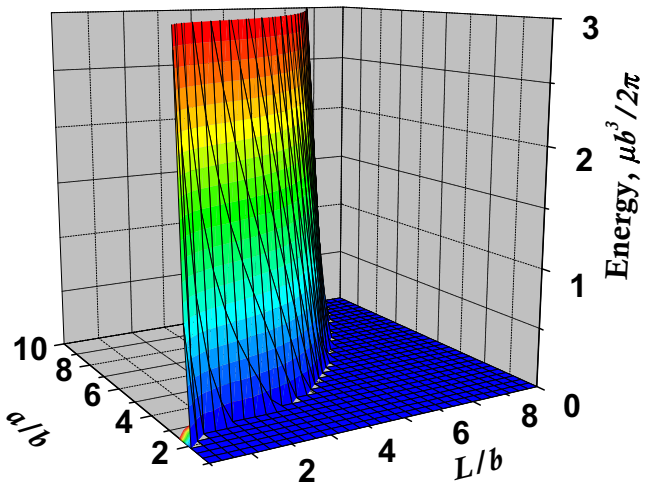

Figure 10: Formation energy of rectangular dislocation loop at the crack tip (spontaneous nucleation). Stress intensity factor $K_I = 0.46K_{gc}$.

According to the obtained analytical results spontaneous nucleation of dislocation at the crack tip occurs provided stress intensity factor achieves value $K_I \gtrsim 0.43K_{gc}$. It is significantly less than the critical stress intensity factor K_{gc}. So, one can conclude that that crack propagation is always accompanied by ejection of dislocation (at least in iron), *i.e.* quasi-brittle fracture takes place. This preliminary conclusion is consistent with experiments that demonstrate noticeable cold-working of crack surfaces. Experimentally measured values of the specific surface energy are approximately two orders of magnitude higher in comparison with that of the ideal surface: $\gamma \simeq 10^2\gamma_{ideal}$.

Nucleation energy barrier demonstrates extremely sharp dependence on the stress intensity factor, see fig. 11. 10 per cent increase of the actual stress intensity factor $K_I \approx 0.43K_{gc}$ in the vicinity of crack tip increases nucleation energy barrier from near zero values up to several eV and lock dislocation loop nucleation. Such behaviour entails very high sensitivity of the dislocation nucleation (and therefore fracture toughness of material) on the structural surrounding at the crack tip. Any structural inhomogeneities like precipitates, voids, gas bubbles, grain boundaries,

forest dislocations and their pile-ups affect stress distribution at the crack tip and influence on nucleation of dislocation loops.

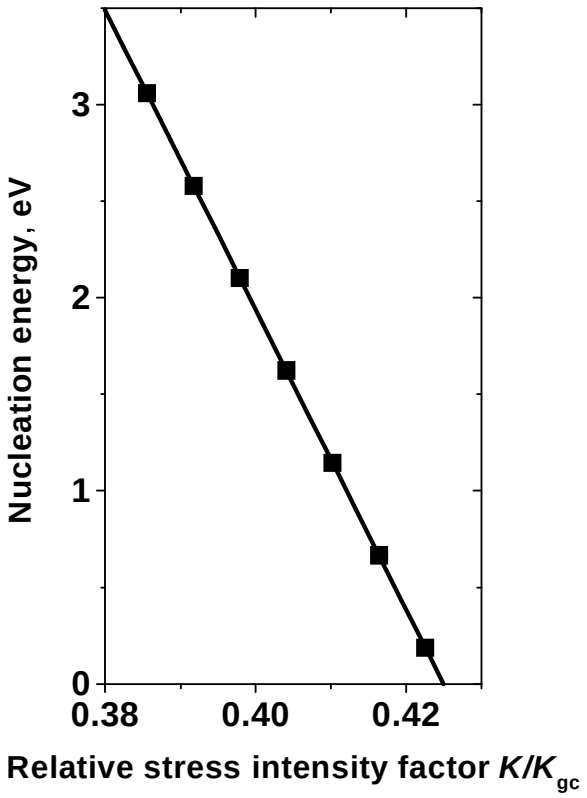

Figure 11: Nucleation energy barrier vs stress intensity factor.

6 Further considerations

Structural inhomogeneities can affect dislocation loop nucleation at the crack tip in two ways. The first one is the direct influence on the stress distribution at the crack tip region. However, another indirect effect also occurs. All structural imperfections decelerate or lock moving dislocations. Forming pile-ups modify stress field in the crack vicinity and prohibit further ejection of dislocation loops. Effect of stress intensity factors on the nucleation of dislocation loops and dynamic screening

of crack tip by moving dislocations is the problems for further consideration in the framework of the general problem of ductile to brittle transition of solids:

- Nucleation of dislocation loop at the crack tip in the presence of forest dislocations in surrounding.
- Effect of finite dislocation velocity.
- Effect of weak obstacles.
- Effect of strong obstacles.
- Reasons for linear dependence of nucleation energy barrier on stress intensity factor.

7 Conclusions

- Spontaneous nucleation of dislocation loops in metals is possible at stress intensity factors of the order of $0.4K_{gc}$. Ejection of at least one dislocation is possible in accordance with experimental observations.
- The shape of the loop is of fundamental importance for nucleation.
- Nucleation energy barrier exhibits strong dependence on the stress concentration at the crack tip region.
- Nucleation of dislocation loop at the crack tip is very sensitive to structural environment (dislocation density, precipitates, *etc.*)

References

[1] B.R.Lawn, B.Hochey and S.Wiederhorn, J.Mater.Sci., **15**(1980)p.1207.

[2] H.Vehoff and P.Newmann, Acta Metall., **28**(1980)p.265.

[3] H.Vehoff, in High-Tempareture Ordered Intermetallic Alloys V, ed. I.Baher *et.al.*, MRS Symposia Proc. No 288 (Material Research Society, Pittsburgh, 1993)p.71.

[4] J.P.Rice and R.Thompson, Philos. Mag., **29**(1974)p.73.

[5] J.P.Rice, J.Mech.Phys.Solids, **40**(1992)p.239.

[6] J.P.Rice and G.E.Beltz, J.Mech.Phys.Solids, **42**(1994)p.333.

[7] P.B.Hirsch, S.G.Roberts and J.Samuels, Proc. Roy. Soc. London A, **421** (1989) p.25

[8] P.B.Hirsch and S.G.Roberts, Philos. Mag. A **64**(1991)p.55

[9] J.Weertman, Dislocation Based Fracture Mechanics (World Scientific Publishing, 1996)524p.

[10] J.P.Hirth and J.Lothe, Theory of Dislocations (Krieger, Melbourne,FL, 1992)

[11] R. de Wit, Sol. State Physics, **10**(1960)p.279

Effect of obstacles for dislocation motion on the formation of plastic zone in the vicinity of Griffith-Inglis crack

Roman E.Voskoboynikov[1]

Abt. Material- u. Komponentensicherheit

Institut für Sicherheitsforschung Forschungszentrum Rossendorf e.V.

Postfach 510119 D - 01314 Dresden

[1] E-mail:*r.voskoboinikov@fz-rossendorf.de*

Abstract

Formation of dislocation pile-up in the vicinity of crack tip in a material subjected to uniaxial loading is investigated. Analytical expression for the dislocation density in the pile-up is found. Dependence of the number of dislocation in the pileup on the applied stress, intrinsic material properties and distance from the crack tip to the obstacle is determined. Stress field ahead dislocation pile-up is evaluated.

Keywords: dislocation; pile-up; crack; mode I loading; stress intensity factor

1 Introduction and overview

It is well established that neutron irradiation at homologous temperatures below $0.4T_m$ (where T_m is the melting temperature) causes a substantial amount of hardening, drop of toughness and a severe reduction in the ductility of fcc, bcc and hcp metals and alloys. Degradation of mechanical properties of metals subjected to irradiation is substantially determined by change (reduction) of the mobility of dislocations. Being weak obstacles for dislocation motion at steady state conditions clusters of point defects, dislocation loops, vacancy voids, etc. created in displacement cascades and/or due to supersaturation of solid solution with point defects might effectively pin dislocations at dynamic loading that occurs e.g. during Charpy V-notch impact testing. Additional barriers require higher temperature for dislocation emission and motion in comparison with initial (unirradiated) state. Suppressed dislocation motion yields reduced energy consumption during plastic flow. A drop in the upper shelf energy in Charpy tests as well as an upward shift of ductile-to-brittle transition temperature of irradiated samples of ferritic (bainitic) steels are clear macroscopic manifestations of the phenomena.

Ductile-to-brittle transition (DBT) is a fundamental phenomenon exhibited by almost all crystalline materials with *possible* exception of fcc metals. The change in fracture behaviour from (quasi)brittle cleavage to ductile failure is always accompanied by significant increase of dislocation density at the near crack surface region [1]. A number of experimental observations unambiguously exhibit noticeable cold-working of crack surfaces due to nucleation of dislocations at the crack tip [1, 2]. Typical micrographs manifesting dominant role of dislocations and dislocation pile-ups in an order of magnitude increment of material toughness as temperature increases above ductile-to-brittle transition temperature are shown in Fig.1.

There are several models dealing with nucleation of dislocation (half-)loop at the crack tip [3]-[5]. The keystone for all the models is the critical stress intensity factor for ejection of dislocation half-loop. It depends on the applied stress, loading geometry, stress concentrators *etc.* Dislocation pile-ups generated at the crack tip also affect effective stress intensity factor. *Shielding* of the crack tip by emitted dislocations depends on the number of dislocations in the pile-up, length of the pile-up, strength of the obstacles pinning dislocation line, their concentration and

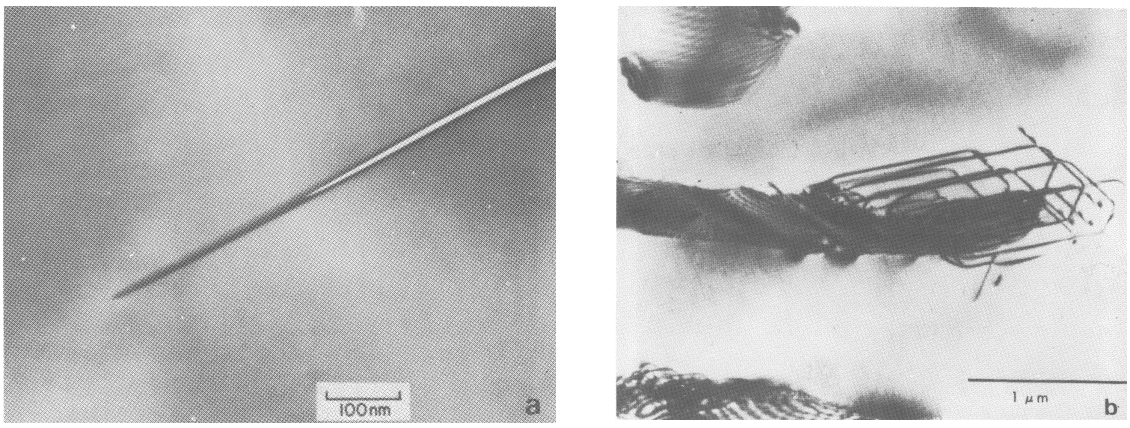

Figure 1: Change in fracture behaviour from brittle cleavage (a) to ductile failure (b) is accompanied by increase of dislocation density at the near crack surface region.

so on. Self-consistent consideration of dislocation pile-up created at the crack tip accompanied by evaluation of the number of dislocations in the pile-up, back stress of the pile-up, stress field in the head of pile-up *vs* concentration of obstacles for dislocation motion, strength of the obstacles, applied stress and intrinsic properties of material is the subject of current issue.

2 Analytical treatment of dislocation pile-up pushed against an obstacle by stress field from the crack tip

Geometry of the problem under consideration is shown in Fig.2. Uniform infinite material with crack is subjected to uniaxial loading σ. Direction of applied stress constitutes right angle with crack plane. Edge dislocations are ejected from the crack tip and form linear pile-up. Pile-up makes angle θ with the plane of crack propagation. The dislocation at the head of pile-up is stopped by an obstacle for dislocation motion. In order to make an upper bond estimate of the number of dislocations in the pile-up let us assume that the obstacle for dislocation motion has an infinite strength. The distance between the obstacle and the crack tip is

equal to L. It is experimentally established that in close vicinity of crack surface there is *dislocation-free zone*. Size of this zone, r_0, depends on the number of ejected dislocations and/or applied stress and initially unknown and to be evaluated within solving of the problem.

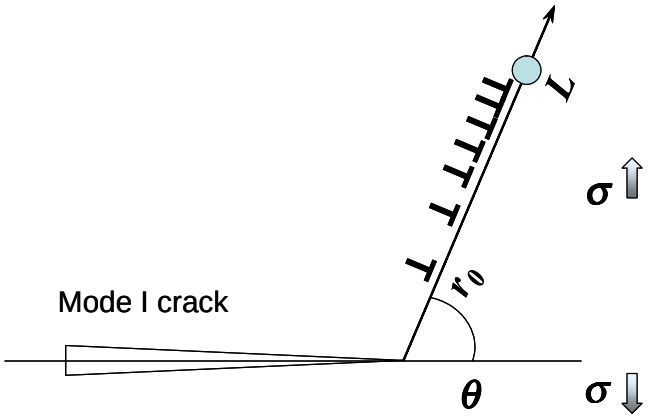

Figure 2: Geometry of the problem under consideration

According to [6] dislocation density $\rho(r)$ in the pile-up pushed against an obstacle by shear stress $\sigma_{r\theta}(r)$ is given by the following relation:

$$\rho(r) = -\frac{1}{\pi^2} \cdot \frac{2(1-\nu)}{\mu b} \sqrt{\frac{r-r_0}{L-r}} \int_{r_0}^{L} \sqrt{\frac{L-\xi}{\xi-r_0}} \frac{\sigma_{r\theta}(\xi)}{\xi-r} d\xi, \tag{1}$$

where μ is corresponding shear modulus, ν is the Poison ratio and $\sigma_{r\theta}(r)$ is actual shear stress in the pile-up slip plane. The integral in (1) is defined by its principal value.

Shear stress $\sigma_{r\theta}(r)$ in the vicinity of the crack tip is equal to [7]:

$$\sigma_{r\theta}(r) = \frac{K_I}{2\sqrt{2\pi r}} \sin\theta \cos\frac{\theta}{2}, \tag{2}$$

where $K_I = \sqrt{\pi a}$ is the stress intensity factor and a is the crack half-length. Dependence of shear stress $\sigma_{r\theta}(r)$ *vs* angle and distance from the crack tip is shown in Fig.3. It can be simply exhibited (see, *e.g.* [7]) that the maximum shear stress is achieved at $\theta \approx 70,5°$, see contour plot Fig.4 for illustration. Below we consider general case of arbitrary angle $0 \le \theta \le \pi/2$. and for quantitative estimates the most preferred angle ($\theta \approx 70,5°$) of dislocation half-loop nucleation is substituted.

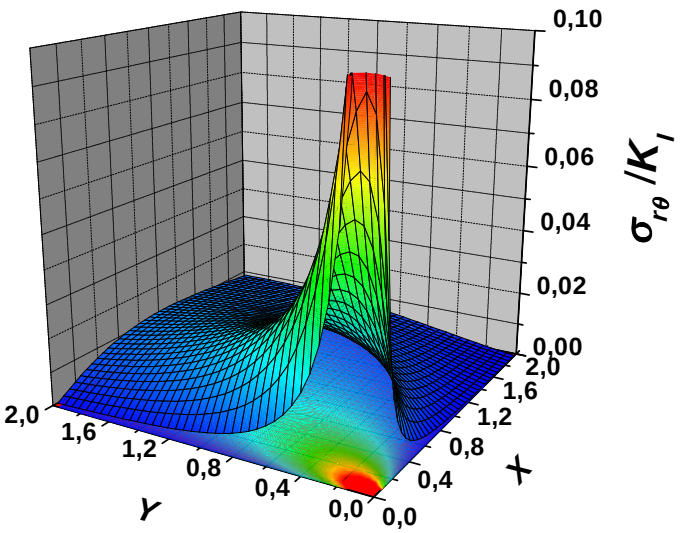

Figure 3: Shear stress $\sigma_{r\theta}(r)$

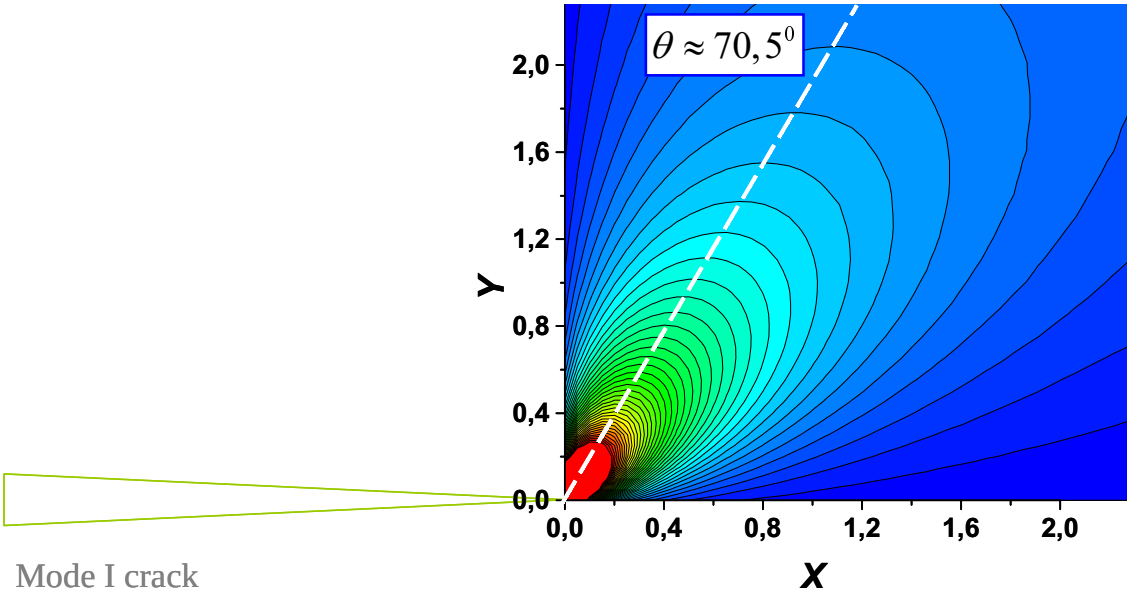

Figure 4: Contour plot of shear stress $\sigma_{r\theta}(r)$ shown in Fig.3

Provided the dislocation density in the pile-up is evaluated the total number N of dislocations ejected by the crack is given by the following relation:

$$N = \int_{r_0}^{L} \rho(r) dr. \tag{3}$$

Let us now consider the integral in Eq.(1). It can be taken accurately for a wide range of rational functions $\sigma_{r\theta}(r)$ by use complex analysis techniques. However, in our case the integral can be estimated if function $\sigma_{r\theta}(r)$ is substituted by its average value over the range $r_0 \le r \le L$:

$$\langle \sigma_{r\theta} \rangle = \frac{1}{L - r_0} \int_{r_0}^{L} \sigma_{r\theta}(r)\, dr = \frac{2K_I}{\sqrt{2\pi}} \sin\theta \cos\frac{\theta}{2} \frac{1}{\sqrt{L} + \sqrt{r_0}}. \tag{4}$$

The substitution is valid until all dislocations lay far enough from the crack tip where dependence of shear stress on the distance from the crack tip is not very strong. Effectively, such simplification leads to slight underestimate of dislocation-free zone (quantitative measure is r_0) and insignificant overestimate of stress field in the head of pile-up.

Substituting average stress $\langle \sigma_{r\theta} \rangle$ instead of actual dependence $\sigma_{r\theta}(r)$ in Eq.(1) we get the dislocation density in the pile-up:

$$\rho(r) = \frac{2(1-\nu)}{\mu b} \sqrt{\frac{r - r_0}{L - r}} \frac{2K_I}{\sqrt{2\pi}} \sin\theta \cos\frac{\theta}{2} \frac{1}{\sqrt{L} + \sqrt{r_0}}. \tag{5}$$

Back stress from the pile-up pushed against an obstacle is equal to [6]:

$$\sigma_B = -\sigma_{r\theta} \left(1 - \sqrt{\frac{r - r_0}{r - L}} \right),\ 0 \le r \le r_0, \tag{6}$$

and the effective stress intensity factor at the crack tip is given by

$$K_\Sigma = K_I \left(1 - \sqrt{\frac{r_0}{L}} \right) \ge K_c \tag{7}$$

Analytical treatment of the problem of nucleation of rectangular half-loop at the crack tip [5] results in

$$K_c \approx 0.43 K_{gc}, \tag{8}$$

see Fig.5. Here K_{gc} is the stress intensity factor of the Griffith crack:

$$K_{gc} = \sqrt{\frac{4\gamma\mu}{1-\nu}}, \tag{9}$$

where γ is the surface free energy. Substitution of Eq.(8) into Eq.(7) lead to the relation of the distance L from the crack tip to the obstacle for dislocation motion and the size of dislocation free zone r_0 for quasi-equilibrium dislocation pile-up generated at the crack tip vicinity:

$$1 - \sqrt{\frac{r_0}{L}} \geq 0.43 \quad \text{or} \quad \frac{r_0}{L} \approx \frac{1}{3} \tag{10}$$

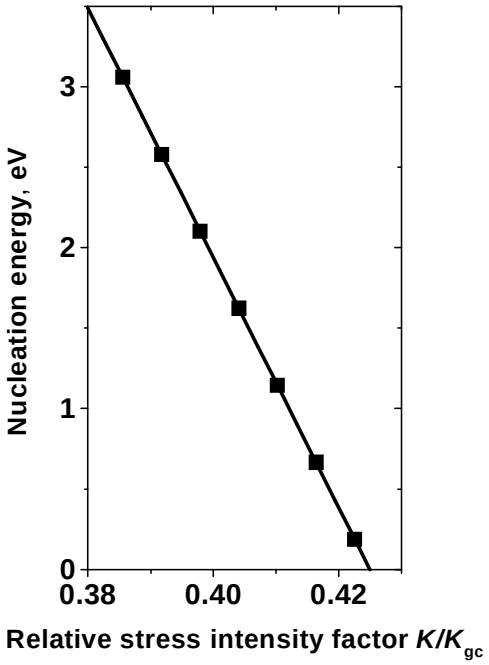

Figure 5: Nucleation energy of rectangular dislocation half-loop against the effective stress intensity factor at the crack tip. See also [5]

Integration of dislocation density Eq.(5) over the pile-up length results in the following expression for the number of dislocation in the pile-up:

$$N = \frac{2\pi\,(1-\nu)}{\mu b}\frac{K_I}{\sqrt{2\pi}}\sin\theta\cos\frac{\theta}{2}\left(1-\sqrt{\frac{r_0}{L}}\right)\sqrt{L}, \tag{11}$$

or taking into account size of dislocation free zone Eq.(10)

$$N = \frac{\pi\,(1-\nu)}{\mu b}\frac{K_I}{\sqrt{2\pi}}\sin\theta\cos\frac{\theta}{2}\sqrt{L}. \tag{12}$$

Formation and equilibrium of the dislocation pile-up in the vicinity of mode I crack was treated under assumption of infinite strength of the obstacle for dislocation motion. However, real strength of obstacles for dislocation motion is finite and its value depends on the nature of obstacles, their size, spatial distribution and so on. Provided strength of the obstacles is less than the actual shear stress pushing dislocation, the obstacle becomes dislocation-transparent i.e. cannot pin dislocations anymore. In the case of our quasi-static consideration it means that if shear stress in the head of pile-up exceeds the strength of the obstacle the head dislocation (closest to the obstacle) is 'pushed through' the obstacle and moving away. Shielding from the pile-up falls down, force balance at the crack tip is broken and leads to spontaneous nucleation of one more dislocation. As soon as the dislocation is ejected the status quo is restored but the stress in the head of the pile-up increases as well and the next dislocation can be pushed through the obstacle. Stress field ahead of pile-up depends on external loading, length of pile-up, number of dislocations in the pile up *etc.* Let us now estimate the value of this stress.

It was shown [6] that stress field ahead of pile-up can be estimated using following relation

$$\sigma_H = \sigma \left(\frac{L - r_0}{d} \right), \tag{13}$$

where d is the distance between the first and the second dislocation in the pile-up:

$$d = \frac{\mu b}{\pi (1 - \nu) N \sigma}. \tag{14}$$

Substituting the number of dislocation in the pile-up (11) and actual stress (4) one gets stress ahead of pile-up against intrinsic properties of material, applied stress and average distance between obstacles:

$$\frac{\sigma_H}{\sigma} = \sqrt{\frac{L}{\Lambda} \left(1 - \frac{r_0}{L} \right)}, \tag{15}$$

where

$$\Lambda = \frac{\mu b}{\pi (1 - \nu)} \frac{b}{4\gamma} \frac{1}{\left(\sin\theta \cos\frac{\theta}{2} \right)^2}.$$

Let us now estimate the number of dislocations in the dislocation pile-up and stress field ahead of the pile-up. Taking typical elastic constants for iron $\mu = 82\, GPa$, $\gamma = 2\, J \cdot m^{-2}$, $\nu = 0.29$ and the Burgers vector $b = 0.287\, nm$ according to Eqs.(12)

and/or (11) we get the dislocation number in the pule up: $N \simeq 32$ (for $L = 1\,\mu m$). The distance between the first and the second dislocation in the pile-up is equal to $d \simeq 4b$ and shear stress ahead of the pile-up is $\sigma_H \simeq 10\sqrt{5}\sigma$ i.e. more than 20 times larger than external loading.

3 Resume

The issue deals with analytical treatment of dislocation pile-up pushed by mode I crack stress field against an obstacle for dislocation motion. In the framework of phenomenological approach dislocation density in the pile-up is evaluated. Within the force balance approach the number of dislocation *vs.* applied stress, distance between the obstacle and crack tip *etc.* is calculated. The estimate of shear stress ahead of dislocation pile-up is conducted.

References

[1] B.R.Lawn, B.Hochey and S.Wiederhorn, J.Mater.Sci., **15**(1980)p.1207.

[2] H.Vehoff and P.Newmann, Acta Metall., **28**(1980)p.265.

[3] J.P.Rice and R.Thompson, Philos. Mag., **29**(1974)p.73.

[4] J.P.Rice, J.Mech.Phys.Solids, **40**(1992)p.239.

[5] R.E.Voskoboinikov, Analytical description of brittle to ductile transition in bcc metals. Nucleation of dislocation loop at the crack tip, Wissenschaftlich-Technische Berichte FZR-344, Marz 2002.

[6] J.P.Hirth and J.Lothe, Theory of Dislocations, 2nd Edition (Krieger, 1992) 857p.

[7] J.Weertman, Dislocation Based Fracture Mechanics (World Scientific Publishing, 1996)524p.

EMBRITTLEMENT OF REACTOR PRESSURE VESSEL STEELS: A LOOK ON THE MESOSCOPIC LEVEL

Stay report by Dr. Vladimir A. Borodin
(RRC Kurchatov Institute, Moscow)
FZ Rossendorf, 19 May - 04 July 2002

1. Introduction

Among various macroscopic manifestations of the effect of radiation on reactor structural materials, irradiation embrittlement remains the least understood. Indeed, good fundamental knowledge is achieved for such effects as radiation swelling or radiation creep, at least in those parameter ranges which are of practical relevance, and corresponding theories are able not only to explain qualitative trends of material behaviour, but even dare to give quantitative predictions, which are correct within an order of magnitude. Qualitatively new problems in these fields appear rarely and are related usually to some particular details of material behaviour out of the common parameter range.

The situation with radiation embrittlement is more complicated, which may seem strange form a foreigner's point of view. Indeed, in contrast to irradiation creep and swelling, which were discovered only after a certain time of reactor operation, the problem of mechanical stability of reactor structural materials, first of all - steels, was addressed from the very beginning of reactor design. In fact, the necessity to guarantee a specified limit of material strength is one of the principal factors that determine selection and development of reactor steels, including reactor pressure vessel (RPV) steels (see. e.g. [1]). As a result, the enormous amount of experimental data on mechanical properties of various steels is accumulated using quite different testing techniques. It is found that the radiation embrittlement in the range of sufficiently low homologous temperatures (~0.1-0.2 T_m, where T_m is the melting temperature) is a common feature of metals with fcc and hcp lattice, no matter what kind of processing they are subjected to (thermomechanical processing, irradiation, etc.). Of the most practical relevance are PVR steels (with Cr, Mo and Mn additions at a level of 1-2 wt%) and ferritic-martensitic steels considered for fusion applications (9-12% Cr for the currently considered fusion applications).

On the other hand, the effect of irradiation at the micro-level (at length scales from nanometers to at least micrometers) was extensively investigated through the last four decades. The irradiation creates in material point defects (vacancies and interstitials), which accelerate migration of alloy constituents and allow to create new microscopic defects in addition to those existed prior to irradiation. In particular, interstitials created by irradiation can cluster, creating dislocation loops and thus increasing dislocation density. The effect of loops is two-fold. On the one side, very small loops (< 2-3 nm) are immobile and serve as dislocation glide barriers. On the other hand, loops of higher size are readily converted into glissile configurations and can contribute to dislocation motion. Vacancies in bcc iron do not cluster at temperatures of interest for pressure vessels (i.e. below 300^{o}C), but are sufficiently mobile at the reactor operation temperatures and contribute to impurity redistribution and precipitation in the metallic matrix.

The most important impurities are currently assumed to be copper [2] and phosphorus [3]. It is more or less accepted that collision cascades induce copper clustering, even though the exact mechanism is not completely clear. Experimental measurements indicate that cascade-produced copper clusters are not pure copper precipitates, such as formed during high temperature annealing (>600 ^{o}C), but rather loose agglomerates (copper enriched zones) of individual copper atoms or small copper clusters, possibly connected to microvoids. On the other hand, phosphorus has a trend to precipitate at grain boundaries and, as demonstrated recently, at precipitate-matrix interfaces (interphase boundaries), which results in the weakening of grain and precipitate boundaries [3]. Accumulation of phosphorus at grain boundaries is known to be very dangerous and leads to brittle intergranular fracture. The acceleration of phosphorous diffusion by irradiation is a risk factor, especially when the

irradiation time tends to the exploitation limit of ~ 20000 h. A possibility to avoid this risk is to capture phosphorus at interphase boundaries in the grain bulk, which is often the case in RPV steels. The most important precipitates for phosphorous segregation seem to be metal (vanadium, chromium, niobium) carbides. Indeed, as shown by fractographic studies of several US and Russian steels [3], the only steel with pronounced brittle intergranular fracture is Russian steel 25Kh3NM, which, in contrast to other Russian steels, contains no vanadium, but in contrast to American steels (which are also vanadium-free) contains several weight percent of chromium. As a result one can expect chromium carbide formation, which usually occurs on grain boundaries, and no pronounced carbide formation in the bulk.

The results above indicate that, in addition to copper and phosphorous, carbon may be an important factor in the effect of radiation on the microstructure development. Additionally, the importance of sulphur is possibly underestimated. Indeed, sulphur can precipitate together with manganese in big MnS precipitates. Their number density is possibly too small to noticeably affect plasticity, but they are important for fracture, because, as well as carbides, they serve as crack initiation places [4].

The effect of microstructure variation by irradiation, as well as by any other treatment (thermomechanical processing, aging, etc.), on the modification of mechanical properties of steel includes at least two aspects, namely - .the modification of the material plasticity and the modification of fracture properties. From physical point of view, plasticity and fracture are stipulated by different microdefects. Indeed, the defects responsible for plasticity are dislocations, while fracture occurs as a result of crack propagation. The crack propagation, however, often involves dislocation emission from the crack tip and crack interaction with already existing dislocations and is thus related to plastic properties. Note that all other microstructural defects do not play direct role in either plasticity, or fracture, but they affect these processes indirectly, as moderators of dislocation movement and crack propagation.

The difference between these two processes - plasticity and fracture - largely determines the methods of their investigation. Plastic flow is a long-term process and the in-reactor plastic behavior of meals is definitely different from that observed in post-irradiation tests. On the other hand, the rupture of an overloaded construction occurs extremely fast on the time scale of reactor operation and the material microstructure has practically no time to change during crack propagation, Therefore, it is possible to separate the test procedure in two parts: first to modify material microstructure by irradiation and then test the irradiated samples out of reactor. In other words, irradiation serves as a means to create a material with a certain microstructural “record” and this record is later on reveled in mechanical testing.

Generally speaking, at the test stage it is not very important, in which way that or other microstructural record was created, as long as one is able to get more or less correct information about it. By microstructure we mean the defects at the length scale from nanometers to micrometers, that is - point defects and their complexes, dislocations, precipitates, etc. In fact, rather nice predictions for the defect microstructure evolution at this scale. can be given by general theoretical considerations (this field of activity is currently very developed and is often considered as the essence of radiation embrittlement theory, see e.g. [2]). On the other hand, where theoretical prediction fail, direct experimental information can often be obtained and gives important clues.

And here comes the question, which is a motivation for the current investigation:

Are the available information on steel microstructural development and the accumulated knowledge in the fracture theory sufficient in order to predict the macroscopic (i.e. directly measurable) steel behaviour?

In the framework of the currently popular multi-scale modeling approach [5] this question can be reformulated like this:
Is the behaviour of material at the length scale of centimeters to meters completely determined by microstructure evolution at the level of micrometers? Or do there exist some specific dependencies of material behavior in the length scales gap from micrometers to centimeters?
The second case seems to be more real, having in mind a simple observation [6] that brittleness of big structures (in particular, reactor components) is more pronounced than in test samples (typically, at centimeter length scale).

In the current investigation we address the question above for the case of impact bending tests. During the stay the main attention was paid to Charpy V-notch testing. This choice was due to two main reasons:

1. As stated above, material fracture involves generally simultaneous contributions from two competing processes -plastic flow and fracture itself. However, in large-scale constructions the plastic behaviour is of relatively less importance than in smaller scale samples. Moreover, the strength is in any case the result of crack propagation rather than plastic flow, no matter if he structure big or small. Correspondingly, when one is interested in fracture properties, it makes sense to reduce the contribution of plasticity as much as possible. From this point of view impact tests are definitely preferable to low-rate loading (e.g. creep-rupture) tests, which can demonstrate no brittleness of RPV steels don o very low temperatures [7].
2. Since in any case the modeling cannot be expected to give perfect quantitative predictions, the addressed material behavior should demonstrate pronounced features that would allow model verification already at qualitative level. Charpy V-notch impact tests demonstrate such a pronounced qualitative feature, that is the transition from ductile to brittle material rupture with the decrease of temperature.

2. Ductile-to-brittle transition in impact testing

A typical picture of ductile-to-brittle transition in RPV steel is shown in Fig. 2.1. It is seen that the energy required to break a standard Charpy-V sample depends in a step-like fashion on the temperature, changing from the values of the order of 5-10 J at the lower temperature end (lower shelf, LS) to 150-250 J at the high-temperature end (upper shelf, US). The modification of the curve shape as a result of irradiation and/or thermomechanical processing is usually described in terms of two parameters, namely - ductile-to-brittle transition temperature (DBTT) and the upper shelf energy (USE). An interesting feature of the curve, which draws very little attention from engineers, is weak variation of the LS energy not only from one to another sample of the same steel, but also from one to another steel.

In contrast to LS and US energy, which are physical parameters, DBTT selection is made on the *a priori* basis, as a temperature at which the trend curve drawn through the test data points reaches a certain pre-defined value (e.g. 28 J or 41 J or 47 J, etc.). Having in mind that the scatter of experimental points in the DBT region can be quite large and that there is no physical justification for the shape of the trend curve, it makes little sense to model either DBTT or its shifts resulting from microstructural modification. More reasonable would be the

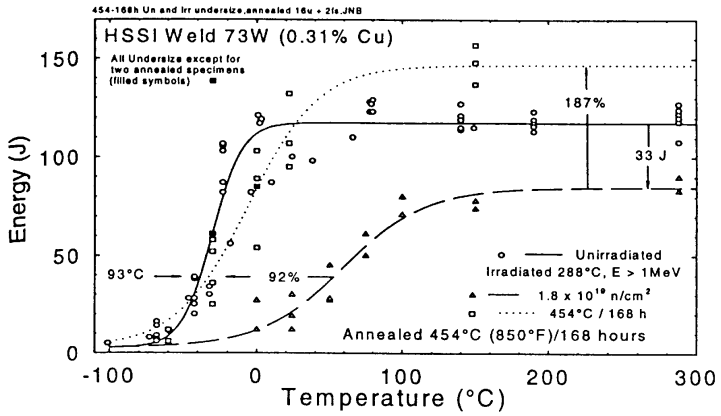

Fig. 2.1 A typical picture of Ductile-to-brittle transition and its variation as a result of irradiation and post-irradiation annealing (from [6]).

modeling of the trend curve as a whole. In this case, the parameters characterizing the DBT region are, evidently, the width of the DBT region and the slope of the trend curve.

Let us consider in more detail, which processes contribute to the energy consumed in Charpy tests. Roughly, there are two main contributions to the energy consumption. The first one, which will be referred below as “service energy”, includes the energy required to create n the sample stresses, sufficiently high to initiate crack propagation. The second contribution includes the energy released during the crack propagation. Evidently, in order to extract from Charpy test information about crack propagation, it is necessary to separate these two contributions.

Strangely enough, no theoretitians seems to care about this, trying to explain the curve as a whole from the point of view of crack dynamics. This can be very misleading, however, if the "suvice energy" contributes noticeably to the total energy consumption during Charpy-V test. Threfore, one of the main tasks of the stay was to estimate theoretically the relative contributions into Charpy energy from different possible mechanism and to propose experiments to be done in the frame of the project in order to separate the service energy and the energy related to crack propagation.

2.1 Service energy

This energy, E_{serv}, can again be subdivided into two contribution: the energy E_{def} required to deform the sample and the energy consumed by the accompanying processes in the equipment, E_{eq}, so that

$$E_{serv} = E_{eq} + E_{def}.$$

2.1.1 Equipment loss

This energy includes mainly the friction loss and is a characteristic of test machine. Its rough estimate for FZR machines is E_{eq} ~1-2 J (according to Dr. H.-W. Viehrig).

Additional contribution at high temperatures can come from the friction between the bended sample and the anvil. In the US region the fracture surface demonstrates the presence of the

"final zone", which results in very pronounced sample bending, until it practically embraces the striker (Fig. 2.2). Correspondingly the sample ends slide along the corners of the anvil, with quite noticeable deformation of sample surface (see Fig. 2.3). How much energy is consumed for this process is not clear.

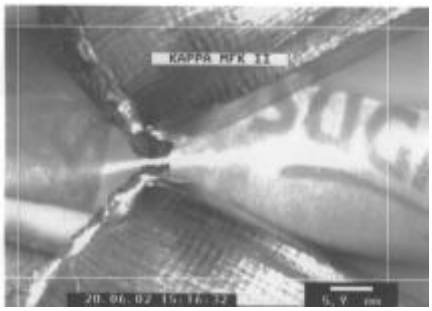

Fig. 2.2. The final plastic deformation of the sample is localized in the very narrow region at the end of fracture surface. The angle between the sample halves is practically that of the striker tip. Sample I323, A508, -19oC (middle of DBT).

Fig. 2.3. Deformation of the sample ends during the drag along anvil corners. Sample 7.1, 15Kh2MFA, 23^{o}C (upper shelf),

2.1.2. Sample deformation

Sample deformation before crack initiation occurs according to the classic 3-point bending scheme (Fig.2.4).

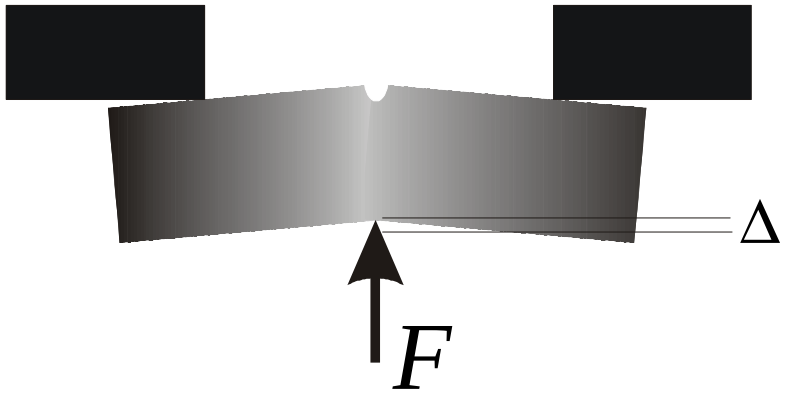

Fig. 2.4. Three-point bending test. *F* is the applied force and Δ - the sample deflection with respect to initial surface position.

The deformation energy E_{def} consists of contributions from elastic deformation, E^{el}_{def}, and plastic deformation, E^{pl}_{def}, their relative importance being dependent on the value of applied load F. The general behavior can be nicely illustrated by the results of computer simulations, performed by Dr. M.Werner (FZR) with the help of finite element program ANSYS, as shown in Figs. 2.5 and 2.6. At low applied loads (< 1.5 kN) the sample deforms purely elastically At higher loads (1.5 to ~ 10 kN) two plastic zones appear. One zone is located

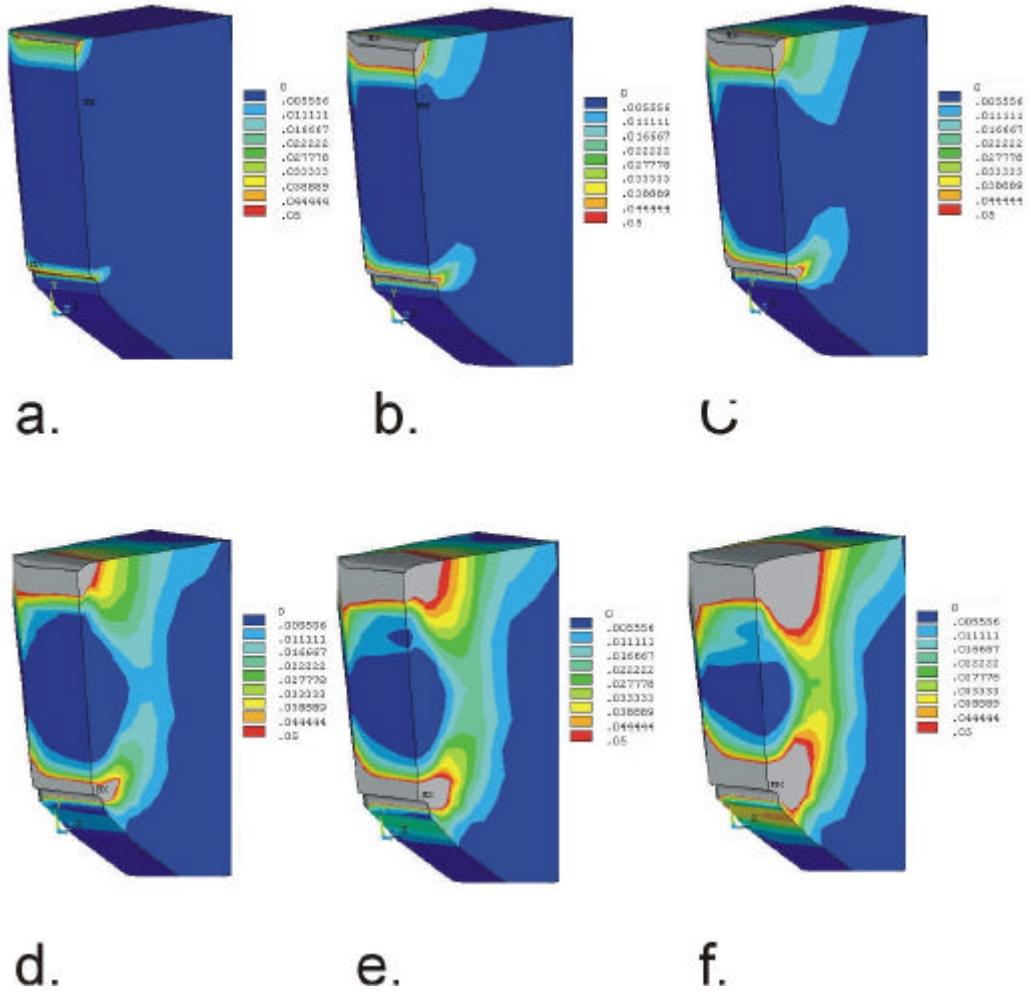

Fig. 2.5. Level map of equivalent deformation distribution in Charpy-V sample as a function of applied load: 8 kN (a), 10 kN (b), 10.5 kN (c), 11 kN (d), 11.5 kN (e) and 12 kN (f). The plastic zone initiation level corresponds to equivalent deformation of 0.4%

close to the notch, while another is adjacent to the line of load application (Fig. 2.5a). Nonetheless, the central layer of the sample remains elastic and, as a result, the deflection of the sample on a line under the striker tip, Δ, only slightly deviates from the linear elasticity predictions. Then, on the rather narrow load range (from 10 to 11.5) the plastic zones protrude from both sides and meet each other, making a unique plastic zone through the whole sample thickness (Figs. 2.5 b-e). This unique plastic zone makes bending easy (i.e. initiates plastic bending instability) and deflection Δ increases quite sharply with the load (Fig 2.6).

It is interesting that due to the geometrical restrictions, plastic zone has, in a certain range of applied loads, a characteristic “barrel-like” shape. From the point of view of the further crack propagation it means that where the crack is initiated in a sample with such shape of plastic zone, it will propagate at the initial and final parts of fracture cross-section through plastic regions, while the middle of the sample is passed in the material, which does not flow plastically. This picture is consistent with experimental observations of fracture surface structure in the DBT region.

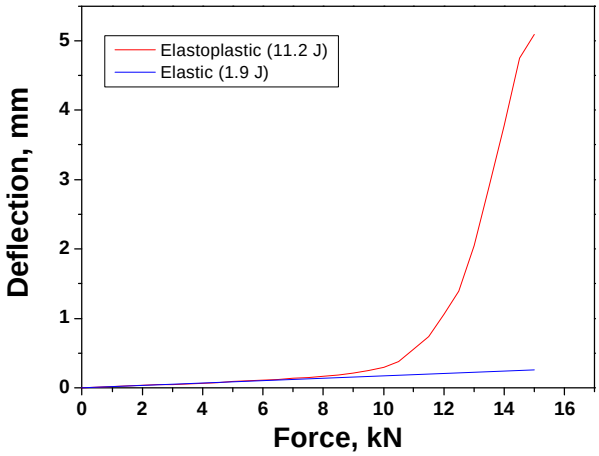

Fig. 2.6. Charpy-V sample deflection under the action of external central force *F*, as calculated using ANSYS program (finite element method) with $\sigma_{0.2}$ = 650 MPA and multi-linear hardening behavior of simulated material (red curve, results by M. Werner). The elastic contribution to the defelection (corresponding to infinite yield stress) is given by blue line.

The estimates of elasto-plastic energy consumed in order to reach the applied force of 15 kN (a typical fracture load for Charpy-V specimens, according to Dr. H.-W. Viehrig) are given by the integral under red curve in Fig. 2.6 and constitute 11.2 J, indicative that the energy consumed for sample bending in the US region is of the order of 10 J. Note that contribution to this value from elastic bending energy is only ~ 2 J. On the contrary, at loads below ~ 8-9 kN the elastic contribution dominates in the total energy of bending.

Certainly, the particular values of the energy consumed for sample bending depend on the particular value of the yield stress and on the particular hardening law used. On the other hand, the order of value of corresponding energies seem to be correct. In order to check it for the most uncertain part, that is - plastic contribution, we used also an alternative approach, based on purely analytical considerations.

Indeed, the energy required to cause plastic deformation ε_{ij} by the action of external stresses σ_{ij} in a cylindrical region with the cross section Σ and the height equal to the sample width *W* can be written down as

$$E_{pl} = W \int_{\Sigma} ds \left(\int s_{ij}\, de_{ij} \right), \qquad (1)$$

where *i*,*j* = 1...3 and summation over repeated subscripts is implied (Einstein summation rule). For the accurate estimate of this value one has to know such badly known things as stress distribution in the plastic zone, the yield stress σ_y (which can depend on the rate of external loading in the case of impact testing), he hardening law and the size of the plastic zone. On the other hand, when only order of magnitude estimate is required, we can approximate $\boldsymbol{E}_{pl}$ as

$$E_{pl} \approx (W\ S)\ s_y\ e_{max}, \qquad (2)$$

where ε_{max} is the maximum plastic deformation in the fracture cross-section. Experimental observations indicate that $\Sigma \sim 0.2$ cm^2, and $\varepsilon_{max} \sim 0.1$. Testing standard requires W = 1 cm. Finally, the yield stress can be assumed of the order of 800 MPa, taking into account possible dynamic hardening. Put together, this gives the order of magnitude estimate $E_{pl} \approx 15$ J, which is consistent with the numerical estimates.

Summing up, the total service energy at US constitutes ~ 10 % of the typical energy consumed, which means that at the upper shelf the Charpy energy is indeed consumed mainly by crack propagation. On the other hand, at LS the service energy is ~ 4-5 J, constituting a noticeable, if not dominant part of the energy consumption. This means that Charpy energy curve is not a convenient means to study crack propagation in the brittle regime, unless one has reliable methods to remove the service energy contribution from the total Charpy energy. Possibly it is better to replace (or at least support) the studies of brittle crack propagation with alternative approaches. Very perspective seems in this respect fracture toughness testing, as related to the "master curve" concept. This remains, however, the task for the future work.

2.1.2 Energy of crack propagation

Generally, there are two modes of material rupture, that is - by purely ductile localized flow (necking) and by crack propagation. For RPV materials something like necking is met only in the ductile fracture regime (US) at the length scale ~ 5 mm (the so-called dimple rupture). The dominant fracture mode is via crack propagation. Depending on the overall material plasticity, the crack propagation occurs either as cleavage, or as a ductile rupture, involving formation of microvoids in front of the crack tip and their coalescence with the crack tip. Finally, the cleavage can be either perfectly brittle, or involve a formation of plastic zone at the propagating crack tip. The latter type of behavior is called either "ductile crack propagation", or quasibrittle fracture (the latter term is adopted below).

The approach to the estimation of crack propagation energy, which is adopted here, relates very much on ideas and results presented in recent fractographic studies in RRC Kurchatov Institute [3]. The central idea of the approach is that any possible fracture mode (indexed as m) create fracture surface with its own specific surface energy, γ_m, so that the total energy of fracture E_{Cr} can be calculated as a weighted sum of these specific energies over all possible fracture modes,

$$E_{Ch} = S \sum_m f_m g_m$$

where S is the specimen cross-section (0.8 cm^2 for a standard Charpy-V specimen) and the weights f_m are the relative fractions of corresponding modes in the fracture surface area.

Since each of different modes of material fracture is characterized by rather specific appearance of the fracture surface, the fractional areas of different fracture modes can be determined by direct observations of fracture surface using scanning electron microscopy (SEM).

During the visit the main work on the topic of crack propagation was related to the study of fracture surfaces. Therefore below we only briefly summarize the current state of the art concerning the specific surface energies and then describe in more detail the microscopy of fracture surface.

2.1.2.1. Specific surface energies

In the simplest, though often adopted, approach one can assume only two regimes of crack propagation, namely - brittle and ductile. In the brittle regime it is assumed that the crack propagation occurs via atomic bond breaking and thus the specific energy of brittle crack propagation is simply the surface tension, which for α-iron constitutes 2 J/m^2 [9,10].

Correspondingly, the energy released during crack propagation at very low temperatures, where brittle fracture dominates in the fracture surface, is only 1.6×10^{-2} J. This estimate is consistent with our earlier statement that in the LS domain the main contribution to Charpy energy comes from service energy.

On the other hand, in the case of ductile fracture the typical ractographic pattern is the dimple rupture (Fig. 2.7). The scheme of crack propagation in this regime assumes that at high temperatures the crack can not propagate by cleavage, because high plasticity of material leads to efficient stress relaxation at the tip of propagating crack. On the other hand. plastic flow of material near the crack tip, associated with stress relaxation, results in the formation of cavities in front of the crack tip (Fig. 2.8). As a rule, the formation of these microcavities occurs on precipitates (Fig. 2.9), which either crack or detach from the matrix along their surface (the latter is especially the case where phosphorus segregates on precipitate surfaces [11]). After a microvoid is formed, the ligament between it and the crack thins out and finally breaks due to plastic flow (a kind of local "necking"). As a result, the crack front shifts forward and the process repeats on the next inclusion.

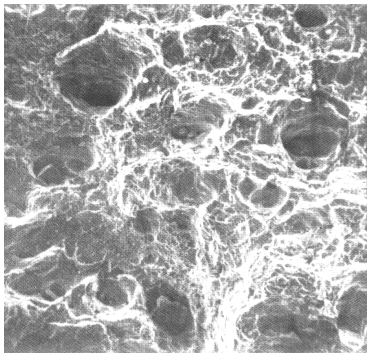

Fig. 2.7. An example of dimple fracture mode. Correlation of individual dimples with precipitates is clearly seen. From [11].

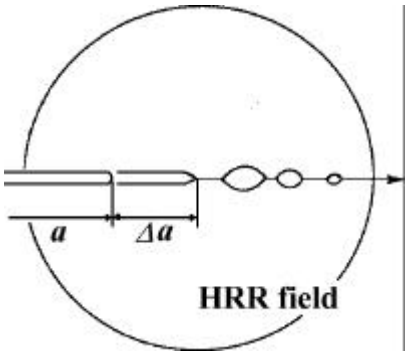

Fig. 2.8. Crack propagation mode, leading to dimple rupture. The crack grows by separate increments, due to coalescence with microcracks in front of crack tip.

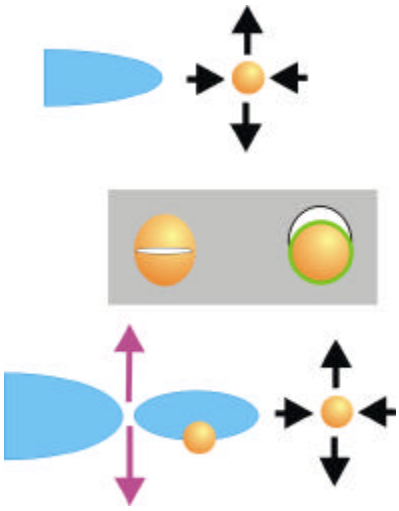

Fig. 2.9. A scheme of microcavity nucleation and evolution, resulting in dimple fracture surface.
Upper row: Plastic flow creates stresses acting on a nearby precipitate,
Middle row: Microcavity nucleates as a crack, either inside or at the surface of precipitate
Lower row: Plastic flow in the ligament between crack and microcavity removes the ligament, while plastic flow in front of microcavity loads another inclusion.

Unfortunately, currently I am not familiar with estimates of the energy releases in relation of such kind of fracture, were these analytical or experimental. However, in order to get an order-of-magnitude estimate we can apply the same approach, as that used in section 2.1.1.

Indeed, we can use equation , where S = H×Δ, where H ~ 0.8 cm is the thickness of Charpy-V sample and Δ is the width of the region, involved in plastic flow in the ligament (see Fig. 2.10), which, according to the typical dimple size, must be of the order of 10 μm.. Assuming again the yield stress ~ 800 MPa and estimating ε_{max} ~ 1 we get

$$g_{pl} \approx 8 \text{ kJ/m}^2$$

so that the total energy release due to completly dimple rapure at the US shoud be of the order of 0.8 J.

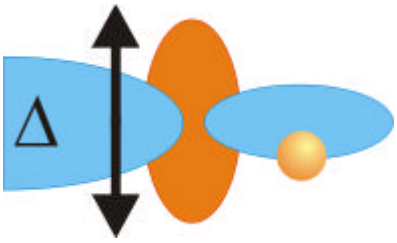

Fig. 2.10. A sketch of local plastic zone (red) during the plastic cavity growth (both crack and cavity are in blue, crack producing inclusion is yellow).

This estimate is at least two orders less than the energy released at the US in reality (~ 150-200 J) and this is a big problem, how one can reconcile this enormous difference with the reality. Possibly the answer is that, according to our SEM observations, but contrary to common knowledge, the dimple rupture is not the only, and maybe even not the most energy consuming mode of Charpy-V specimen fracture at US.

Indeed, if only two fracture modes (brittle and ductile) would contribute to the Charpy energy, equation would predict linear dependence of Charpy energy on the ductile fraction of fracture surface. A preliminary estimate (Fig. 2.11) shows that this is probably not the case. More detailed investigations on this topic will be performed further in the course of the project.

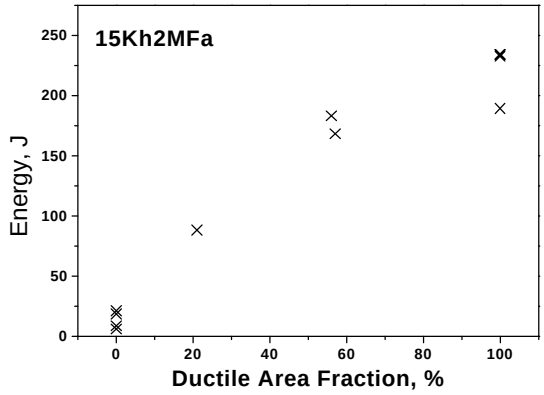

Fig.2.11. Dependence of Charpy fracture energy on the relative area of ductile fracture in the fracture surface. Steel 15Kh2MFA.

2.1.2.2. Fracture surface investigation with optical microscopy and SEM
Strangely enough, fractographic studies of broken Charpy-V samples are rather seldom in the literature (see e.g. [3,4,11]) and usually give only fragmentary picture of fracture surface properties.. The idea of current study was to obtain the information on the structure of fracture surfaces in different temperature intervals, using for each sample a ladder of different magnification levels, from x10-20 (stereo optical microscope, SEM) to x50000 (SEM), in order to have a sound basis for multi-scale modeling of crack propagation in the length scale range from ~0.1 μm to ~ 1 cm. The advantage of stereo optical microscopy is that, regardless of rather low magnification levels (which allows to discern only features exceeding ~ 50 μm), it gives 3-dimentional information, which is extremely important for adequate modeling of fracture relief, but which is nearly completely lost during SEM investigations.

All samples were previously tested in FZ Rossendorf in controlled Charpy impact tests and covered the range from LS, through DBT region, and to US. SEM was performed predominantly on samples from steel A508 (with only one sample of Russian steel 15Kh2MFA, in order to study a special effect in US region), while optical microscopy studies included, in addition to A508, also sets of samples from steels A533 and 15Kh2MFA, in order to compare behavior of different types of steel.

The results of microscopic studies are still to be processed, and so only preliminary results are reported here.

The main observations can be summarized as follows:

- Lower shelf

The fracture surface relief is very rough in all samples and for all investigated steels. The reason for that is the grain structure, which is manifested at the level of 50 μm and corresponds most probably to prior austenitic grains (PAGs). Within each individual grain the fracture surface (facet) is perfectly smooth (if not consider the ripples) down to the length scale of at least 0.1 μm. On the other hand, from grain to grain the orientations of cleavage surfaces vary and the resulting landscape at the length scale of millimeters looks like “hills and valleys”. In fact, the absolute majority of neighbouring facets are disoriented with respect to one another, though the disorientation angle is usually not high (noticeably less then 90^o). There exist also places, when several neighbouring PAGs lay within the same plane and the flat surface can include from 4 to sometimes 20-30 grains. But surely such multi-grain flat areas do not dominate. It is interesting, however, that even within these multi-grain clusters the grains are nicely distinguished, because grain boundary regions do not shine in the light of optical microscope like the rest of the flat surface. SEM microscopy reveals that the reason for that might be the ductile nature of rupture at the grain boundaries, even though the grains themselves are broken in cleavage.

The absolute majority of brittle fracture faces is inclined with respect to the overall direction of the crack propagation. Moreover, even in fracture toughness tests, where the initial crack is created by fatigue and the dynamic crack starts more or less uniformly along the crack line, the initial direction of brittle crack is inclined at approximately 45 degrees to the sample mid-plane and only later the crack turns in the direction of striker tip (i.e. moving again at approximately 45^oC), see Fig. 2.12. It looks like the crack likes to move at an inclined angle to the load. It is interesting, that the “multi-grain” cleavage areas are also laying on the slopes of "hills".

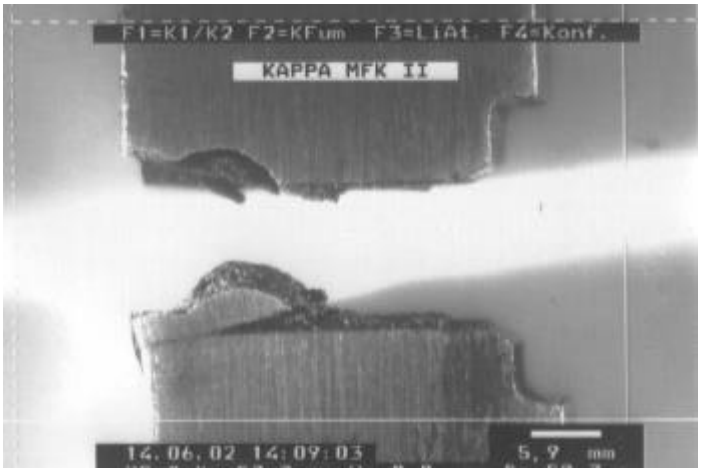

Fig. 2.12. A side view on the fracture plane in a static fracture toughness test. Sample L161, A508, +20^{o}C (possibly- the temperature of COD measurement?).

Very pronounced features are multi-cracking and cross-cutting, especially in A508, but in other steels as well. Cracks parallel to the fracture surface are observed, which are stopped in the material and did not lead to the cracking. Sometimes there appear “ligaments” between two sub-cracks, propagating in parallel, and these ligaments are broken along very smooth surfaces (cross-cuts, see Fig. 2.13), having the height of some tens of PAGs and the length up to millimeters. In contrast to the cleavage surface, these cross- cuts do not shine brightly. The planes of “cross-cuts” are always practically normal to the fracture surface, but the cross cut normal can have arbitrary direction with respect to the sample boundaries. From geometrical considerations, the mechanism of the fracture leading to cross-cuts must to be pure shear. Generally, the lower is the temperature, the more pronounced is multi-cracking and the bigger are cross cuts. In Charpy samples there is also a trend that multicracking is most pronounced close to the notch and becomes less pronounced (though does not vanish completely) to the end of fracture surface.

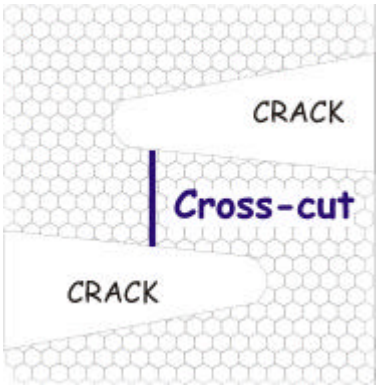

Fig. 2.13. A scheme of “cross-cut” formation.

Sometimes in-between the cracks, connected by a cross-cut, another crack is located. It is then crossed through, without any deflection of the cross-cut surface. As a result a cross-section of propagating crack is recorded. One such crack is shown in Fig 2.14. The cross-cut is runs nearly parallel to the fracture surface and along the sample edge, so that the figure presents a longitudinal portrait of propagating crack. It is not very clear in the figure, but the a crack

propagates through an ensemble of “minicracks”, which are inclined at approximately 45^{o} to the main crack propagation. On the average, however, the crack remains parallel to the fracture surface in this place.

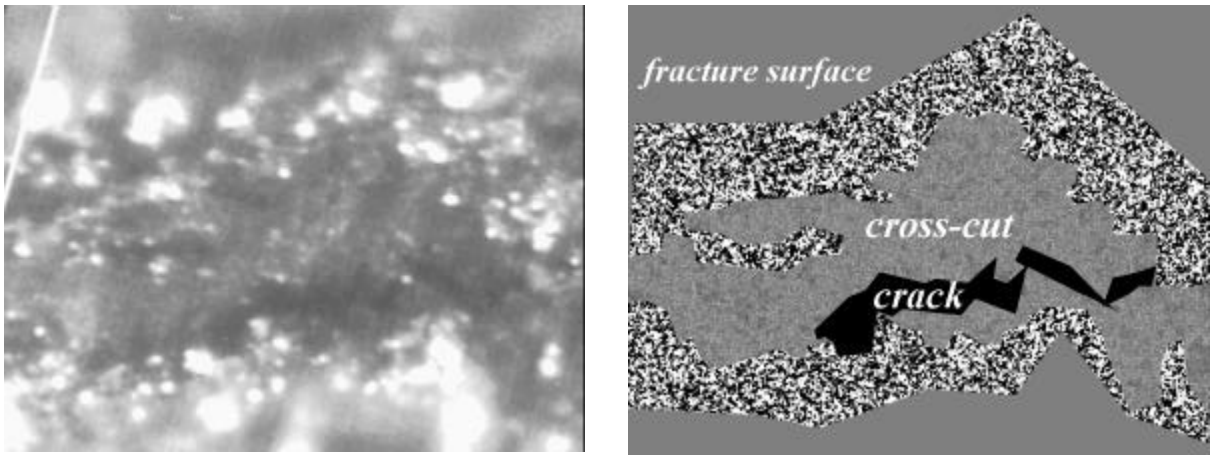

(a) (b)

Fig. 2.14. Longitudinal crack through a cross-cut - optical micrograph (a) and a comment (b).

DBT

It is well known from the literature that the fracture surface in this temperature range is a mixture of ductile and brittle sections, which is in agreement with the stress distribution pattern in Charpy samples, as discussed in sect. 2.1.2. It is tempting to state that the crack propagation in he plastic region occurs in ductile mode and the crack propagation in the elastic part- in brittle mode. The picture observed in reality looks, however, more complicated.

It can be seen that initially material deforms plastically at the notch, with formation of plastic flow ripples at the notch tip surface and shrinkage of sample cross section immediately under the notch. However, the cracks do not propagate through the plastic zone. When the stress in the plastic zone becomes too high, the cracks are starting either in the central part of the notch (steel A 508), or from the sides of the notch (A533B and 15Kh2MFA, possibly more ductile than A 508) and "cut off" the plastic zone from the remaining part of material. For the case of the central crack, the "torn off" plastic zone looks like a characteristic "tooth" on one of the sample halves (see Fig. 2.15). The microscopy data on samples tested in DBT region are not yet processed, but from the crack geometry and SEM observations (Fig. 2.16) one can make a preliminary conclusion that these are ductile shear cracks. In contrast to any other fracture modes, these cracks are extremely flat with roughness becoming noticeable at the length scales of 10-20 mm. It is interesting also, that the crack propagation seems to limited by their task to relieve plastic strains at the notch. As long as these cracks propagate sufficiently deep into the sample (1-2 mm), they stop.

The fracture crack initiates from the tips of these “by-pass” cracks. The surface of the fracture crack is brittle, with all features typical for this fracture mode - rough relief, multi-cracking, cross-cuts.

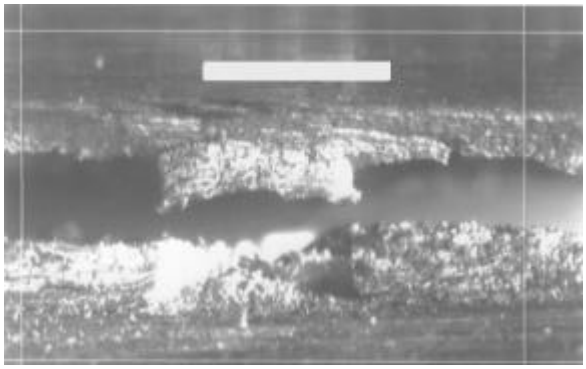

Fig. 2.15. The plastic zone region ("tooth") torn off by a flat crack started from the notch (on the lower sample half. Note that the cracks are present also above the tooth, which means that cracking occurs at both sides of the plastic zone, but only one of these cracks propagates further. Sample I 312, steel A508.

The higher is the temperature (and the lower is the yield stress), the more pronounced become plastic features (e.g. the width of the plastic "tooth" or the size of the side shear crack) and the less pronounced become the brittle crack features (multi-cracking, cross-cuts).

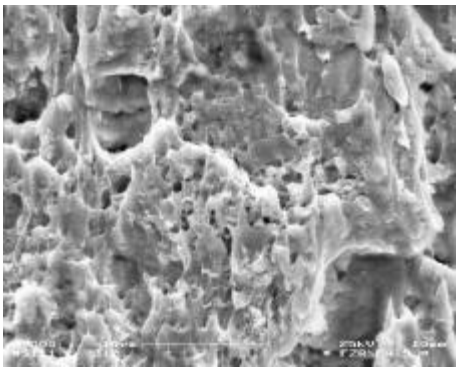

Fig. 2.16. Typical fracture surface of the initial crack bypassing the plastic zone "tooth". Sample I 312, steel A508.

A new feature of DBT samples, as compared to LS, is the “side lips”, running along the side edges of the fracture surface. From general theoretical consideration (plain stress conditions on the sample surface, in contrast to plain strain conditions in the bulk) and from direct microscopic observations (Fig. 2.17) it can be concluded that these are the edge plastic zones. In fact, plasticity in this zone is noticeable at temperatures as low, as the beginning of DBT. The presence of "lips" in the fracture surface means that, again, the crack does not go into the plastic zone, but tries to bypass it. Their surface of the lips looks visually quite different from either quasi-brittle, or ductile fracture in central regions. Preliminary analysis of SEM observations indicates that the fracture mode at the lip surface is ductile shear. Again, the higher is the temperature, the more pronounced are side lips. In fact, they provide an easy means to sort broken samples with respect to test temperatures.

Fig. 2.17. Plastic zone (lip) along the side edge of fracture surface.
Sample I 320, steel A508.

Upper shelf

Funny enough, but the sequence of fracture events remains the same as in the DBT region, but the details change. Initial plastic flow at the notch occurs practically along the whole notch and involves sometimes (in A508) a sequence of shallow cracks in the middle of the plastic flow zone. Quite noticeable cavity formation can be observed in the flow region. The initial "bypass" cracks are much more pronounced and deep than in the DBT region. However, their features (flat cracks with ductile shear micro-relief) remain. Again, the normal crack starts only from the end of a by-pass crack.

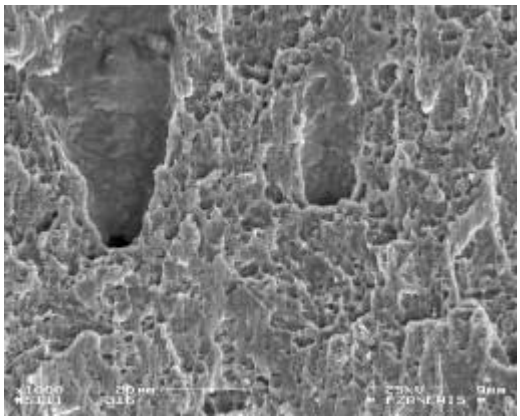

Fig. 2.18, The fracture surface of initial by-pass crack in the US region.
Note the big cavities, due most probably to plastic flow, that are cut by the crack. Sample I 316, steel A508.

The expected surface microscopy of fracture surface in the Us region (“dimple” rupture) is observed only locally, at least in steel A508 (other steels were not studied due to limited visit time). In fact, the fracture surface morphology looks unfamiliar (Fig. 2.19) and remains to be identified.

One more interesting feature of the fracture surface, appearing already in the upper DBT region is the "final zone" on the fracture surface. The fracture crack seems to stop in the sample, not reaching the striker tip (in fact, often aiming past the tip) and leaving a thin ligament (< 1 mm width) which undergoes extremely efficient plastic bending (until the striker is practically embraced by the sample). Only then the ligament finally breaks, an the most strange thing is that the fracture surface of the final crack is brittle (Fig.2.20), even though the nominal test temperature may lay far inside the US region. This particular feature

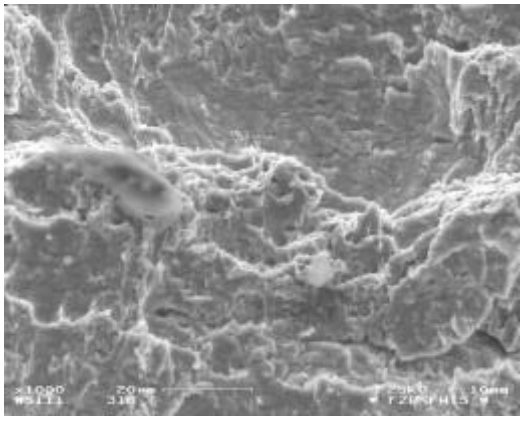

Fig. 2.19. Fracture surface in the region of ductile crack propagation. Dimple fracture mode is observed, but is not dominant. Sample I 316, steel A 508.

is typical for all steels studied (A508, A 533 and 15Kh2MFA) and for different tests. It is interesting to note, for example that the shape of the fracture surface in the final zone of a sample in dynamic fracture toughness test looks very similar to the fracture surface of static fracture toughness test (cf. Figs. 2.21 and 2.12).

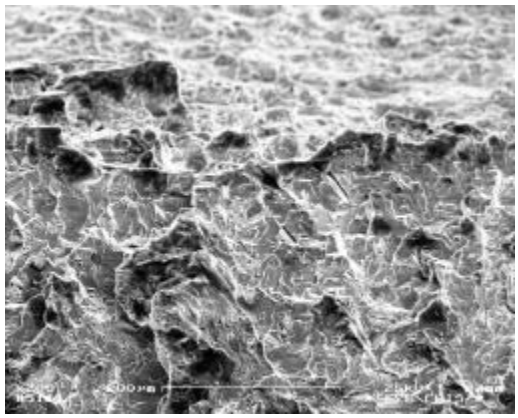

Fig. 2.20. Fracture surface in the final zone of the sample tested high in the US region. Sample I 316, steel A 508.

Fig, 2.21.. A side view on the final zone of fracture surface in a dynamic fracture toughness test. Note that the surface of the lower sample half practically follows the shape of striker tip. Sample H145, steel A508.

References

[1] N.N.Alekseenko, A.D.Amaev, I.V.Gorynin, V.A. Nikolaev, Radiation damage of VVER pressure vessel steels (Energoizdat, Moscow, 1981) (in Russian)
[2] G.R. Odette and G.E. Lucas, Rad. Eff. Def. Sol. 144 (1998) 144.
[3] B.A. Gurovich, E.A. Kuleshova,Yu.A. Nikolaev,Ya.I. Shtrombakh, J.Nucl.Mater.246 (1997) 91.
[4] M. Mäntylä, A. Rossoll, I. Nedbal, C. Prioul, B.Marini, J.Nucl.Mater. 264 (1999) 257.
[5] G.R. Odette, B.D. Wirth, D.J. Bacon, N.M. Ghoniem, MRS BULLETIN/MARCH 2001, 176.
[6] Report NEA/CSNI/R(2001)6, 2001
[7] J.Böhmert, G. Müeller, J Nucl.Mater. 301 (2002) 227.
[8] S.K. Iskander, R.K. Nanstad, C.A. Baldwin et al. Effect of Radiation on Materials: 20th Int. Symp. ASTM STP 1406 (ASTM, West Conshohocken, 2001) p. 302.
[9] A.T.Price, H.A.Hall, A.P.Greenough, Acta met. 12 (1964) 49.
[10] H.Jones, M.G.Leak, Met.Sci.J 1 (1967) 211.
[11] B.A. Gurovich, E.A. Kuleshova, Ya.I. Shtrombakh, O.O.Zabusov, E.A.Krasikov, J.Nucl.Mater.279 (2000) 259.

REPORT

on a visit of Dr. Maria G. Ganchenkova (Moscow Engineering Physics Institute, Moscow, Russia) to Forschungszentrum Rossendorf, Institut für Sicherheitsforschung

Research topic: **Kinetics and physical mechanisms of crack propagation in polycrystalline solids**

The project is related to the effects of radiation on mechanical properties of metals, in particular - ferritic steels. The guaranteed mechanical stability of steels (in particular - material resistance to fracture) is an important factor for reliability of nuclear facilities and for environmental safety. The high practical relevance of the material property degradation problem promotes the cooperative research in different industrially developed countries.

Due to the complex nature of the effects of irradiation on metals, basic research is a prerequisite for proper selection of materials and prediction of their property degradation in radiation environment. It was only recently realized that the effect of irradiation on fracture of steels is a multi-scale problem. The idea is that the radiation damage is a sum total of processes occurring simultaneously at different length scales. An important advantage of this approach is the clear understanding that the processes at each length scale are quite different in their nature and require different investigation approaches. In order to provide overall consistency, studies at each particular level should incorporate the knowledge obtained at the lower scale levels. At present, irradiation effects on material structure are intensively studied at the length scales from nanometers to ~1 micrometers. On the other hand, the fracture of relevant structures occurs at length scales above a few centimeters. Typical material testing techniques involve smaller, but still macroscopic samples (typical length scale of 1 mm to 1 cm). There remains a gap, which embraces the range from micrometers to millimeters. An appropriate understanding of the medium-scale effects on crack propagation mechanisms in relevant materials is necessary to add the missing link between the microscopic theories and the experimental observations.

In order to explain the experimentally observed topology of the fracture surface, one must consider some other factors, that govern the mode of crack propagation in addition to the external loads. For example, the facet orientation can be sensitive not so much to the global stress distribution, but rather to the local stress distribution at the tip of propagating crack. On the other hand, it can be related to the rather complicated microstructure of the primary austenitic grains, which includes the planes of possibly weaker interatomic bonding (preferred crystallographic planes, bainitic lath boundaries) and various phase inclusions (carbides, oxi-nitrides, sulphides) induced by steel preparation and operation conditions. In other words, the change of orientation of fracture facets from grain to grain can be defined by many factors, introducing inherently stochastic aspect in the crack propagation process. Respectively, all parameters measured in fracture tests (stress intensity factors, energy consumption during crack propagation, etc,) will be necessarily fluctuating. For the better understanding of the basic factors determining the peculiarities of crack propagation , it would be highly desirable to have a tool that might allow the evaluation of relative contributions of different factors to the resulting fracture surface topography. At present, only very limited attention is paid to the modeling of crack propagation in polycrystalline metals, but even a simplest two-dimensional model of this kind [1] demonstrates that the account of polycrystallinity can provide a reasonable explanation of the experimentally observed scatter of mechanical test output results.

The aim of this work is the development of a numerical model of stochastic crack propagation in polycrystalline materials, which would be able to reproduce a three-dimensional shape of the fracture surface.

Description of the model

The model describes crack propagation in a polycrystalline material as a sequence of individual grain fracture events. When a crack breaks a grain, the neighbours of this grain are to sustain additional load, which was earlier applied to the broken grain. As a result of this increased load, one of the neighbors can also break, again redistributing the load over its neighbors, and so on, grain by grain. This is a typical stochastic process, which is treated here in terms of a "continuous time" kinetic Monte-Carlo (MC) approach. The approach is assumed that external loading is symmetric with respect to an average fracture plane, regarded as the base plane for crack propagation. Since the model is currently aimed at simulation of transgranular fracture, we adopt pseudo-3D description of the polycrystalline structure of simulated material.

Array of grains

The cross-section of a standard Charpy sample is a rectangle of 1.0 cm by 0.8 cm, while the typical grain size falls in the range of ~ 10-50 micrometers,. It means that the size of the array of grains varies from approximately 200x200 to 1000 x 1000 elements, which is quite reasonable from the point of view of the modern computational possibilities. We define the x-y plane as a plane normal to the load direction and divide the area into equal elementary figures, squares or hexagons, as shown in Fig. 1.

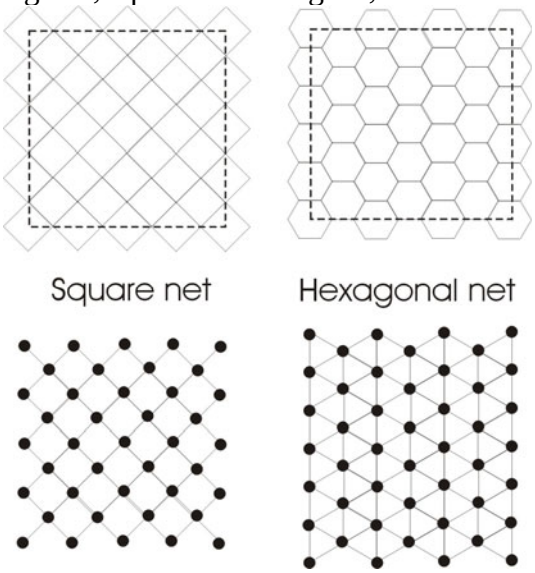

Upper row: two versions of fracture cross-section (dashed rectangle) separation into elementary areas.

Lower row: Equivalent networks.

Figure.1 Fracture cross-section separation into elementary areas.

In the model, a stack of grains in z-direction is modeled as a uniform prism, whose base is a selected elementary shape (i.e. a square or a hexagon) and which is infinite in z-direction. The whole array of grains is, thus, an array of neighbouring prisms (Fig. 2).

Fracture events

The propagation of a crack in the array of grains is considered as a sequence of individual fracture events. In each individual prism (grain) the crack is considered as a plane, cutting the prism at a certain height and having some inclination with respect to the base plane (see Fig. 3). In the applied continuous-time Monte-Carlo scheme each MC step (= fracture event) is

successful. This is achieved by dealing with probabilities (per unit time) to break the grain in the next MC step. For each grain we define 4 or 6 partial probabilities to start fracture from a certain edge of this grain. Evidently, a partial probability is non zero only in the case when the corresponding neighbour grain is already broken (Fig. 2). The sum of partial probabilities over all edges in the grain defines the integrated probability (the grain fracture probability) that this grain fails in the next fracture event.

The sum of fracture probabilities over all grains gives the total probability P_{tot} that something happens within the unit time. This means that in the time interval $dt = 1/P_{tot}$ at least one event will happen for sure. Which particular event will happen depends on its relative probability with respect to P_{tot}. Therefore, we can select an event according to its relative probability (i.e. events with zero probability are never selected), and assume that the selected grain breaks from the selected side. Correspondingly, for this grain we fix the heights of crack intersection with the grain corners (see Fig.2), set all partial probabilities for this grain equal to zero and recalculate the cracking probabilities for all its neighbours.

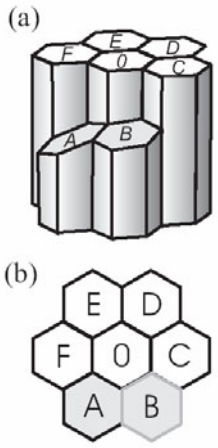

Figure 2 Illustration to the definition of cracking probabilities. The figure shows several prismatic grains on the base plane. The central grain (marked with 0) has two neighbours that are already broken (A and B; only lower halves of these grains are shown, in order to make visible the fracture facets). Hence this grain is a potential candidate for fracture. The crack facet in grain 0 can start only from one of the broken neighbour grains, but not from those unbroken (C to F).

Criteria of grain fracture

Generally, a crack in a virgin grain is allowed to propagate with any orientation of a fracture facet, satisfying the restriction that the facet originates as a continuation of a facet in one of its already broken adjacent grains. Additionally, the probability of fracture for an individual grain depends on such parameters as external loading scheme, sample geometry and instantaneous crack configuration.

Even taking into account the above mentioned restrictions, we have sufficient freedom in selecting crack propagation direction inside the grain that is going to be broken at the current MC step. Therefore, we need to introduce an additional criterion that allows to fix the facet orientation in the newly broken grain. For example, we can base this criterion on the strain energy density dependence on the angle between the current and previously broken grains [1]. This criterion assumes that the crack propagates in the direction where the strain energy density has a minimum and this density falls below a certain critical value. In the case of the plane stresses the criterion is expressed as

$$\begin{aligned}
&\textit{Energy density: } S = a_{11}K_I^2 + 2a_{12}K_I K_{II} + a_{22}K_{II}^2 + a_{33}K_{III}^2 \\
&\textit{Where} \qquad a_{11} = (1/16\mu)\left[(1+Cos(\theta))(k-Cos(\theta))\right] \\
&\qquad\qquad a_{12} = (1/16\mu)2Sin(\theta)\left[Cos(\theta)-(k-1)\right] \\
&\qquad\qquad a_{22} = (1/16\mu)\left[(k+1)(1-Cos(\theta))+(1+Cos(\theta))(3Cos(\theta)-1)\right] \\
&\qquad\qquad a_{33} = (1/4\mu) \\
&\qquad\qquad k = (3-\nu)/(1+\nu)
\end{aligned} \qquad (1)$$

where μ is the share modulus, and ν the Poisson ratio. For a common case of the loading scheme, the criteria of crack propagation is defined by more complicated expressions, which obtained, however, based on the same principles as for those denoted as Eq. (1).

Correspondingly, the crack propagation angle is strictly fixed by the local geometry of the crack facets in the grains surrounding the grain considered in the current MC step. Alternatively, the crack propagation angle can be selected among the available possibilities weighted according to the Gibbs distribution over strain energy densities at corresponding angles between the originating and the newly formed facets. It should be noted that the mentioned criteria are formulated in terms of the local stress distribution around the crack tip in the coordinate system related to the facet that initiates the crack at the current MC step.

Simulations of crack propagation in a polycrystalline material

Based on the described algorithm, a kinetic MC code has been developed and tested for the internal consistency, assuming at this stage artificial grain fracture probabilities. In particular it was checked that the crack in a new grain starts only provided this grain already had broken neighbours and that the new facet had a common edge with the facet in the grain, which was chosen by MC algorithm as the predecessor.

The profile of the forming crack was tested in dependence of the load state and shows reasonable behaviour. Fig. 3 demonstrates the spatial profile of the crack surface, composed from individual hexagonal facets for two cases of external loading, either pure shear ($\sigma_{zz} = -\sigma_{xx}$, $\sigma_{yy}=0$, Fig.5a), or biaxial tension ($\sigma_{zz} = 3\sigma_{xx}$, $\sigma_{yy}=0$, Fig.5b). It can be seen that the general orientation of the fracture surface corresponds to the loading scheme, and the profile shape is sensitive to the loading scheme. In particular, in the case of pure shear the crack remains practically flat, even though it is split into several "branches" that run parallel to each other at somewhat different heights. In the case of biaxial loading the roughness of the surface is much bigger and one can find several points, starting from which the crack breaks into branches propagating at considerably different inclinations. This feature qualitatively reproduces the crack propagation behavior of real steel samples that demonstrate quite pronounced branching of crack propagating in a brittle model.

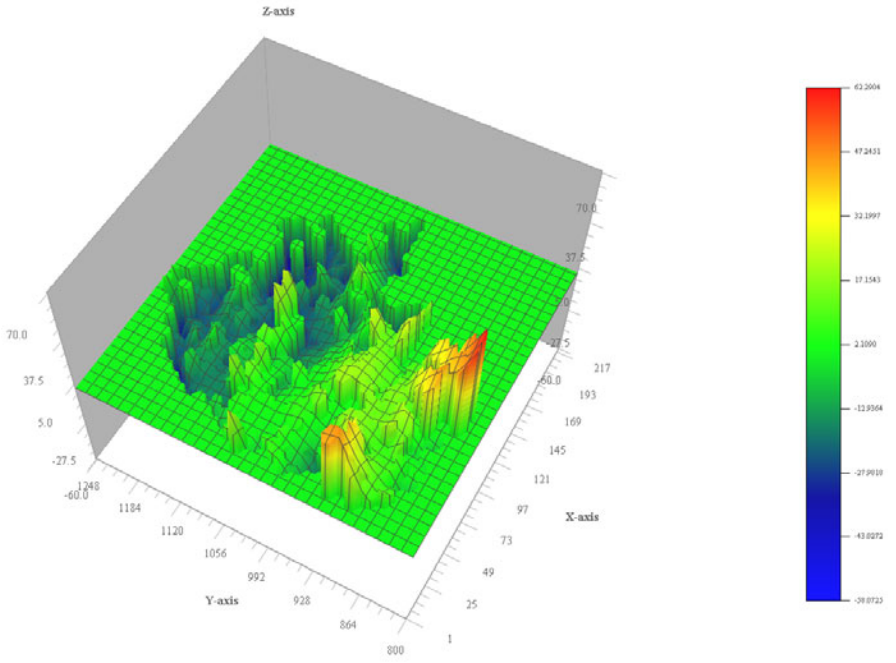

(a)

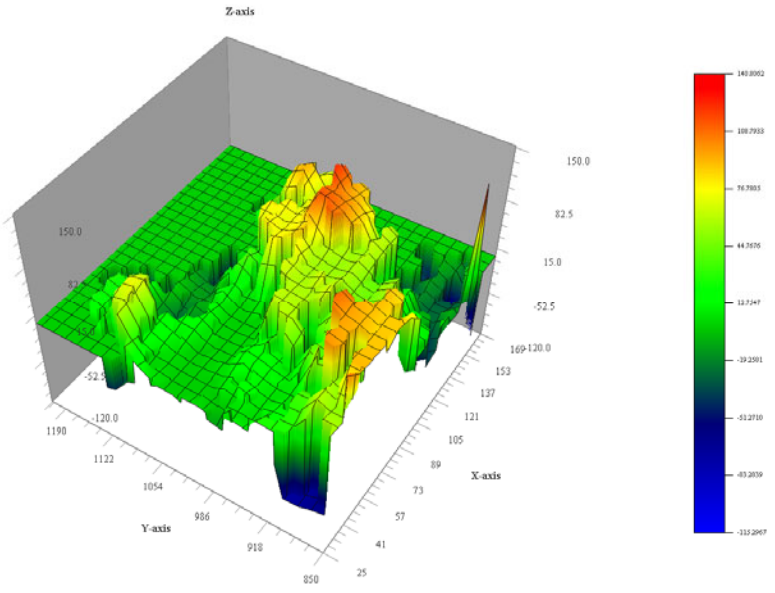

(b)

Fig.3 Examples of crack profile simulation at different external loads: (a) pure shear; (b) biaxial loading. The horizontal plane is the "base plane" for prismatic grains. Only the broken grains are shown.

In addition to the qualitative features, the simulations allow to obtain more qualitative information. Indeed, for any simulated shape of the fracture surface it is possible to define the

total area of fracture facets and, multiplying it by the specific surface energy, to estimate the energy consumed during the crack propagation. Performing several MC runs at the same external parameters, the scatter of the consumed energy can be estimated. Finally, performing MC runs at different temperatures, one can estimate the temperature dependence of both the average value and the scatter of consumed energy. However, it makes little sense to present such quantitative data for the currently used criterion for selection of new facet orientation.

Perspective plan

The application of the currently developed model of crack propagation in polycrystalline materials to specific conditions of ferritic steel embrittlement under irradiation requires noticeable upgrade of both the current simulation program and the physical models, underlying it. At its present state the program is adopted to the case of transgranular material fracture. In this situation grain boundaries do not require detailed description, because their main role is to act as a barrier for micro-cracks. Therefore, the shape of grains is described using quite simple approximations, while neither the spatial orientation of grain boundaries, nor spatial correlations between the boundaries of neighbour grains are considered explicitly. The situation changes drastically, when one wants to include more details of fracture,, such as preferential formation of impurity precipitates at the grain boundaries. The intrinsic steel impurities, such as carbon, tend to precipitate under irradiation due to radiation enhancement of carbon mobility, and there is a strong tendency for precipitating carbides to nucleate preferentially along special planes (grain and martensite lath boundaries). As a result, grain boundary weakening often occurs. The account of a realistic grain-boundary structure becomes therefore the essential part of the model. The planned work will be oriented on the development of the current model and simulation tools in such a way that they were able to treat simultaneously transcrystalline and intercrystalline fracture.

Reference

[1] G. Pluvinage, Mecanique elastoplastique de la rupture (CEPADUES,1995).

Mikrostrukturanalyse von bestrahlten Reaktordruckbehälterstählen

Andreas Ulbricht und Jürgen Böhmert
Forschungszentrum Rossendorf e.V.

1 Einleitung

Das Material eines Reaktordruckbehälters (RDB) erfährt insbesondere im kernnahen Bereich durch die Bestrahlung mit schnellen Neutronen strukturelle Veränderungen auf der Nanometer-Skala, die mit zunehmender Neutronenfluenz zu einer fortschreitenden Verschiebung der Spröd-duktil-Übergangstemperatur des Stahles führen. Diese Übergangstemperaturverschiebung ist sicherheitsrelevant. Die demnach erforderliche Überwachung des Bestrahlungsverhaltens erfolgt auf der Grundlage von kerntechnischen Regelwerken durch die mechanische Prüfung voreilend bestrahlter Einhängeproben. Es gibt eine Reihe von Argumenten, diese Vorgehensweise auch weiterhin durch anwendungsorientierte Grundlagenforschung zu begleiten. Hierzu zählen:

- die Übertragbarkeit der an den Voreilproben gewonnenen Messergebnisse auf das Bauteil, die auf Annahmen beruht, z.B. den Flussdichteeinfluss betreffend, sowie
- das nach wie vor unvollständige Detailverständnis der Natur und der Bildungsmechanismen der nanometer-skaligen bestrahlungsinduzierten Atom- bzw. Defektcluster.

Unter den experimentellen Methoden zeichnet sich die Neutronen-Kleinwinkelstreuung (SANS)[(1)] dadurch aus, dass sie als einzige eine statistisch abgesicherte Größenverteilung der bestrahlungsinduzierten Cluster zu bestimmen gestattet. Zusätzlich lassen sich mit SANS bei Messung im Sättigungsmagnetfeld über das Verhältnis von magnetischem und nuklearem Streuanteil Aussagen über die Zusammensetzung der Cluster gewinnen.

Im Bericht werden die Ergebnisse der SANS-Experimente von ausgewählten Proben zusammengefasst.

2 Experimentelles

2.1 Material

Folgende Werkstoffe wurden im Rahmen des Projektes mit SANS untersucht:

- ein WWER-440 Grundwerkstoff 15Kh2MFA (Charge KAB),
- ein WWER-440 Schweißwerkstoff Sv10KhMFT (Charge VTT),
- ein WWER-1000 Grundwerkstoff 15Kh2NMFAA (Charge D) und
- zwei Eisenbasis-Modelllegierungen (Charge ML-A, ML-B).

Angaben zur chemischen Zusammensetzung dieser Werkstoffe enthält die Tabelle 1. Der russische RDB-Stahl Charge KAB gilt als Prototypmaterial der WWER-440/230-Generation. Mit dem Schweißwerkstoff (VTT) stand erstmalig für SANS-Untersuchungen ein Material zur Verfügung, dass nach einer Neutronenbestrahlung ausgeheilt und wiederbestrahlt wurde. Der WWER-1000 Grundwerkstoff (Charge D) wurde im Forschungsreaktor Rez (Tschechien) bei einer um eine Größenordnung höheren Neutronenflussdichte im Vergleich zu der aller anderen Werkstoffe bestrahlt. Die ausgewählten Eisenbasis-Modelllegierungen dienten der Untersuchung des Einflusses bestimmter Legierungs- und Verunreinigungselemente auf die Bildung

(1) engl.: Small-Angle Neutron Scattering.

Tab. 1 Chemische Zusammensetzung der untersuchten Werkstoffe (Angaben in Masse-%, Rest Fe).

Charge	C	Mn	Si	Cr	Ni	Mo	V	S	P	Cu
KAB	0.14	0.55	0.24	2.60	0.24	0.62	0.27	0.013	0.011	0.22
VTT	0.06	1.14	0.40	1.63	0.11	0.48	0.20	0.016	0.035	0.14
D	0.16	0.59	0.26	2.22	1.27	0.63	0.09	0.012	0.005	0.03
ML-A	0.01	0.39	0.15	-	0.01	-	-	0.004	0.002	0.01
ML-B	0.01	0.49	0.25	-	0.01	-	-	0.005	0.012	0.42

Tab. 2 Bestrahlungsbedingungen der untersuchten Werkstoffe.

Charge	Reaktor	Bestrahlungs-temperatur T / °C	Neutronenfluenz, Φ / 10^{21} cm^{-2}	Flussdichte, φ / 10^{12} cm^{-2}s^{-1}
KAB (I-1)	WWER2 Rheinsberg	255	0.0023	0.10
KAB (I-2)			0.004	0.17
KAB (I-3)			0.009	0.13
KAB (I-4)			0.080	3.4
KAB (I-5)			0.143	5.5
VTT (I)	WWER-440 Loviisa	270	0.035	0.42
VTT (IAI-1)			0.013	0.42
VTT (IAI-2)			0.025	0.42
VTT (IAI-3)			0.038	0.42
D (I-1)	LVR-15 NRI Rez	290	0.029	29.5
D (I-2)			0.097	34.0
ML-A (I-1)	WWER-440 Rovno-1	270	0.010	0.4
ML-A (I-2)	WWER-440 Kola-3	270	0.080	3.0
ML-B (I-1)	WWER-440 Rovno-1	270	0.010	0.4
ML-B (I-2)	WWER-440 Kola-3	270	0.080	3.0

bestrahlungsinduzierter Cluster in einer Eisen-Matrix. Die Bestrahlungsbedingungen der ausgewählten Werkstoffe sind in der Tabelle 2 zusammengefasst.

2.2 SANS-Experimente

Die SANS-Experimente wurden an den deutschen Neutronenstreuzentren, dem HMI BENSC Berlin und der GKSS Geesthacht, durchgeführt. Für die Untersuchungen wurden etwa 1 mm dicke scheibenförmige Proben verwendet, die sich während der Messungen in einem Sättigungsmagnetfeld senkrecht zur Richtung des einfallenden Neutronenstrahls befanden, um den magnetischen und nuklearen Streubeitrag (Indizes: mag und nuc) zu trennen. Aus der gestreuten Intensität, dem kohärenten makroskopischen Streuwirkungsquerschnitt pro Raumwinkelelement,

$$\frac{\mathrm{d}\Sigma}{\mathrm{d}\Omega}(\vec{Q}) = \frac{1}{V_\mathrm{G}} \left| \int_{V_\mathrm{G}} \Delta\eta(\vec{r})\ \mathrm{e}^{-\mathrm{i}\vec{Q}\vec{r}}\ \mathrm{d}^3\vec{r} \right|^2 = \int c_R \Delta\eta^2 V S_\mathrm{K}\ \mathrm{d}R, \qquad (1)$$

konnte nach Fouriertransformation, die auf den Volumenanteil bezogene Größenverteilung der Streuzentren c_R berechnet werden. In Gl. (1) ist $\vec{Q}$ der Streuvektor, V_G das Gesamtvolumen der durchstrahlten Probe, $\Delta\eta(\vec{r})$ die Abweichung von der mittleren Streulängendichte des Materials am Ort $\vec{r}$, V das Volumen eines einzelnen Streuers mit dem Radius R und S_K die Einteilchen-

streufunktion, der sogenannte Formfaktor des Streuers. Die Integration über alle Größen R liefert den Volumenanteil c.

Informationen zum Streukontrast $\Delta\eta^2$ sind notwendig, um Volumenanteil bzw. Anzahl der Cluster berechnen zu können. Ausgehend vom bekannten ferromagnetischen Verhalten der Grundsubstanz wurde angenommen, dass die Cluster kein magnetisches Moment besitzen. Damit lässt sich aus dem magnetischen SANS-Wirkungsquerschnitt der Volumenanteil der Cluster bestimmen. Mit Hilfe des A-Verhältnisses

$$A = \frac{\dfrac{\mathrm{d}\Sigma}{\mathrm{d}\Omega}_{\perp}}{\dfrac{\mathrm{d}\Sigma}{\mathrm{d}\Omega}_{\parallel}} = \frac{\dfrac{\mathrm{d}\Sigma}{\mathrm{d}\Omega}_{\mathrm{mag}}}{\dfrac{\mathrm{d}\Sigma}{\mathrm{d}\Omega}_{\mathrm{nuc}}} + 1 \tag{2}$$

der Streuintensität senkrecht und parallel zur Magnetisierungsrichtung der Probe, können zusätzlich Aussagen über die chemische Zusammensetzung gewonnen werden. Theoretisch lässt sich das A-Verhältnis aus den Streulängen b_i und den Atomanteilen v_i, aus denen die Cluster (C) und die Matrix (M) zusammensetzt sind, wie folgt berechnen:

$$A = 1 + \left(\frac{\sum_i v_i^{\mathrm{C}} b_{i,\mathrm{mag}}^{\mathrm{C}} - \sum_i v_i^{\mathrm{M}} b_{i,\mathrm{mag}}^{\mathrm{M}}}{\sum_i v_i^{\mathrm{C}} b_{i,\mathrm{nuc}}^{\mathrm{C}} - \sum_i v_i^{\mathrm{M}} b_{i,\mathrm{nuc}}^{\mathrm{M}}} \right)^2 . \tag{3}$$

Eine ausführliche Beschreibung der angewandten Mess- und Auswertemethoden ist in der Dissertation [1] enthalten, die im Rahmen dieses Projektes entstand.

3 Ergebnisse

Der WWER-440 Grundwerkstoff, Charge KAB, wurde im unbestrahlten Zustand sowie in fünf bestrahlten Zuständen mit Neutronenfluenzen von $(0.002 - 0.143)\cdot 10^{21}$ cm^{-2} (Neutronenenergie $E_\mathrm{n} > 0.5$ MeV) untersucht. Die Abbn. 1 und 2 zeigen die kohärenten Streuwirkungsquerschnitte sowie die daraus berechneten Größenverteilungen der Streuzentren skaliert mit dem magnetischen $\Delta\eta^2_{\mathrm{mag}}$ und dem nuklearen Streukontrast $\Delta\eta^2_{\mathrm{nuc}}$. Der Streuwirkungsquerschnitt ist erhöht ab Streuvektoren mit $Q > 0.5$ nm^{-1} für die bestrahlten Zustände (Abb. 1). Dies trifft sowohl für den magnetischen als auch für den nuklearen Streubeitrag zu. Je höher die Strahlenbelastung (Neutronenfluenz bzw. dpa = displacements per atom), desto ausgeprägter ist der Effekt. Die Größenverteilung der Streuzentren (Abb. 2) zeigt eine bimodale Charakteristik. Vor allem im bestrahlten Zustand tritt eine feindisperse Verteilungspopulation im Größenbereich kleiner 3 nm auf. Ihr Maximalwert liegt etwa bei einem Radius von 1 nm. Der Volumenanteil dieser Population (Abb. 2) nimmt mit der Strahlenbelastung zu, ohne das eine merkliche Veränderung der Streuzentrengröße festzustellen ist. Die zweite Population ist durch ein breites Größenspektrum gekennzeichnet, deren flach verlaufendes Maximum zwischen 5 und 10 nm sich allerdings aus den Messungen nicht hinreichend genau definieren lässt. Diese Population tritt bereits im unbestrahlten Zustand auf und wird durch Bestrahlung mit schnellen Neutronen nicht erkennbar beeinflusst. Die Skalierung in Abb. 2(b) auf absolute Einheiten erfolgte unter der Annahme von nicht-magnetischen Streuzentren. Zum Zweck der besseren Vergleichbarkeit der Größenverteilungen wurde für den Kernstreukontrast in Abb. 2(a) der gleiche Wert gewählt. Die unbekannte atomare Zusammensetzung der bestrahlungsinduzierten Cluster macht eine explizite Kernstreukontrastberechnung unmöglich und gestattet somit nur eine Skalierung in willkürlichen Einheiten.

Der WWER-440 Schweißwerkstoff, Charge VTT, stand neben einem bestrahlten Zustand (0.035 dpa) zusätzlich im ausgeheilten und mit drei verschiedenen Fluenzen (0.013 - 0.038 dpa)

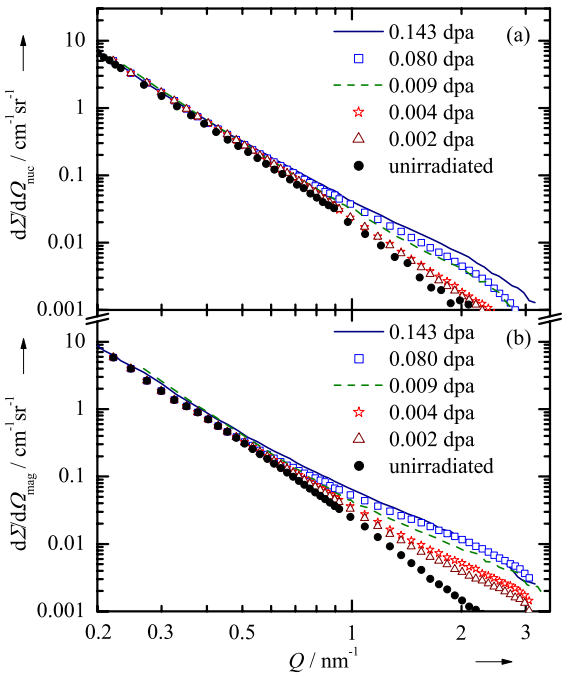

Abb. 1 Kohärente Streuwirkungsquerschnitte für den Werkstoff 15Kh2MFA (Charge KAB) nach unterschiedlichen Neutronenexpositionen: **(a)** nuklearer und **(b)** magnetischer Streuanteil.

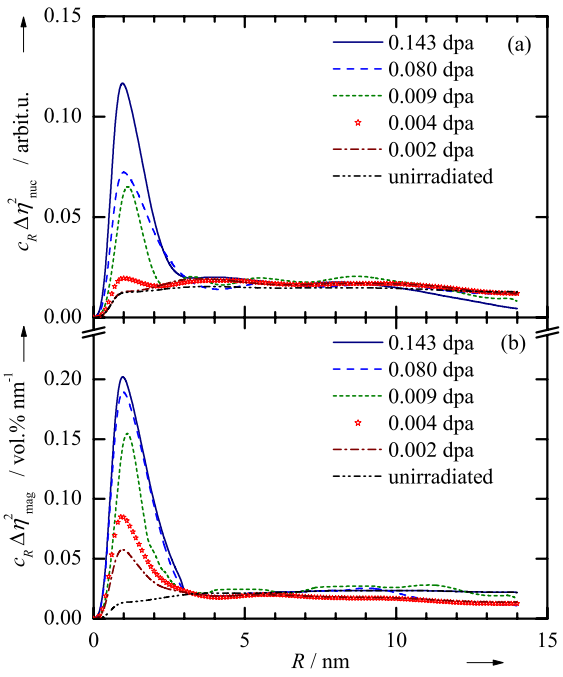

Abb. 2 Volumenverteilungsfunktionen der Streuzentren berechnet aus den Kurvenverläufen der Abb. 1 skaliert mit dem **(a)** Kernstreukontrast $\Delta\eta^2_{\mathrm{nuc}}$ und **(b)** magnetischen Streukontrast $\Delta\eta^2_{\mathrm{mag}}$.

wiederbestrahlten Zuständen zur Verfügung. Die Ergebnisse vor und nach der ersten Bestrahlung zeigen die Abbn. 3 und 4. Das Wiederbestrahlungsverhalten ist in den Abbn. 5 und 6 zusammengefasst. Ein Vergleich der Größenverteilungen in Abb. 4 und 6 lässt erkennen, dass nach einer Ausheilwärmebehandlung und Wiederbestrahlung des Materials deutlich weniger Strahlendefekte bei vergleichbarer Strahlenbelastung gebildet werden. Auffällig ist eine deutliche Differenz im Verlauf der nuklearen und magnetischen Verteilungskurven. Mit dem magnetischen Streukontrast werden offensichtlich zusätzlich größere Inhomogenitäten (2.5 bis 4.5 nm Radius) nachgewiesen, die sich bereits bei der ersten Ausheilglühung gebildet haben und sich durch die Wiederbestrahlung nicht ändern.

Die Ergebnisse zum WWER-1000 Grundwerkstoff, Charge D, sind in den Abbn. 7 und 8 dargestellt. Der grundsätzliche Verlauf der Streukurven bzw. der daraus abgeleiteten Verteilungskurven entspricht dem der bei WWER-440 Werkstoffen gefundenen Charakteristik. Der Volumenanteil der Strahlendefekte wächst tendenziell mit der Fluenz bei gleichbleibender Größe der Strahlendefekte.

Für die Eisenbasis-Modelllegierung (ML-A) sind die gemessenen Streuwirkungsquerschnitte und die daraus berechneten Größenverteilungen der Streuzentren in den Abbn. 9 und 10 dargestellt. Die Streuintensität des unbestrahlten Referenzzustandes ist im gesamten Q-Bereich um etwa eine Größenordnung geringer als bei den Stählen. Grund hierfür ist das Fehlen von Karbiden, die wesentlichen Einfluss auf die Untergrundstreuintensität haben. Trotz der deutlich anderen Materialzusammensetzung entspricht der Verlauf der Streukurve und der daraus ermittelten Größenverteilung dem an den anderen Materialien beobachteten. So werden auch in der Modelllegierung ML-A bestrahlungsinduzierte Cluster mit einem mittleren Radius von 1.0 nm nachgewiesen, deren Anteil mit der Bestrahlung zunimmt.

Die Abbn. 11 und 12 zeigen die Ergebnisse für die Modelllegierung ML-B einschließlich des nach Bestrahlung ausgeheilten Zustandes. Die Modelllegierung ML-B weist einen wesentlich höheren Anteil an bestrahlungsinduzierten Defekten auf als die Modelllegierung ML-A. Zwischen den beiden Bestrahlungszuständen 0.01 und 0.08 dpa sind die Unterschiede im Anteil

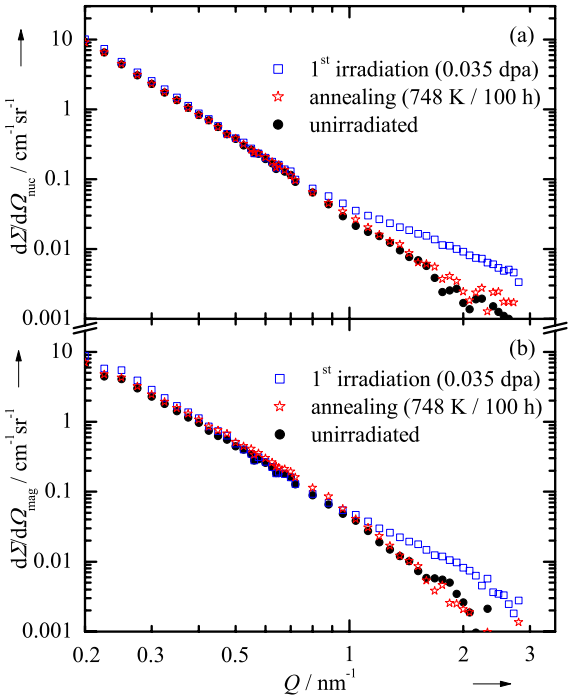

Abb. 3 Kohärente Streuwirkungsquerschnitte für den Schweißwerkstoff Charge VTT (1. Bestrahlung): **(a)** nuklearer und **(b)** magnetischer Streuanteil.

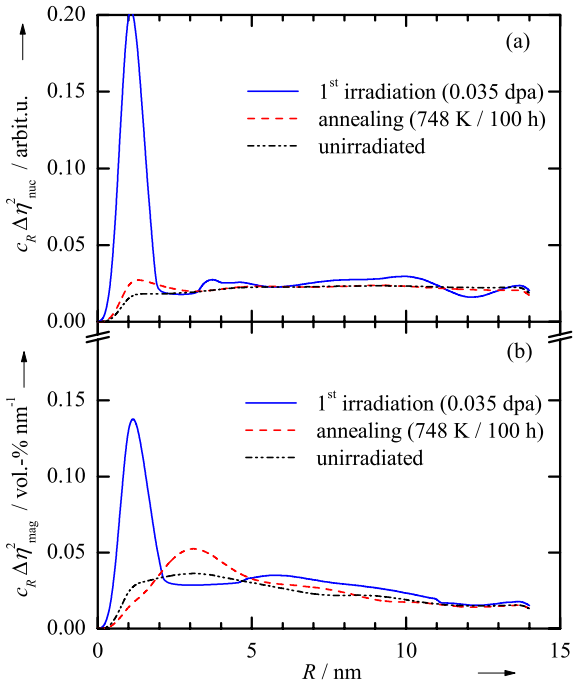

Abb. 4 Volumenverteilungsfunktionen von Streuzentren berechnet aus den Streukurvenverläufen der Abb. 3 skaliert mit dem **(a)** Kernstreukontrast $\Delta\eta^2_{\mathrm{nuc}}$ und **(b)** magnetischen Streukontrast $\Delta\eta^2_{\mathrm{mag}}$.

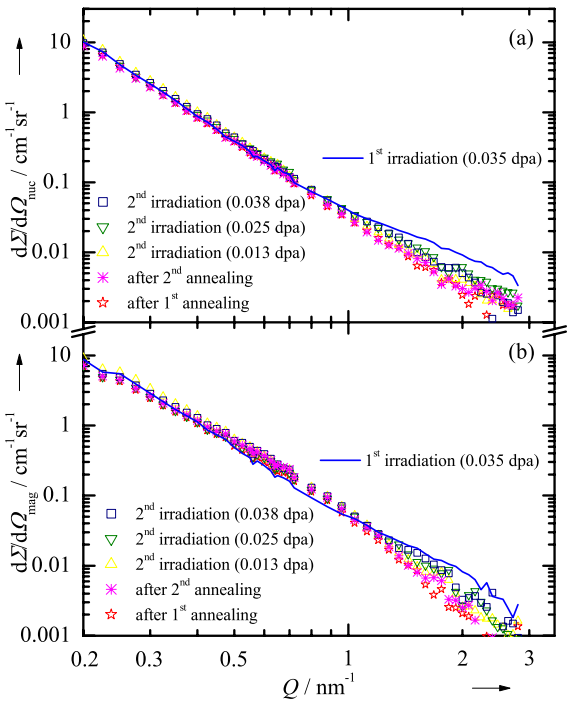

Abb. 5 Kohärente Streuwirkungsquerschnitte für den Schweißwerkstoff Charge VTT (2. Bestrahlung): **(a)** nuklearer und **(b)** magnetischer Streuanteil.

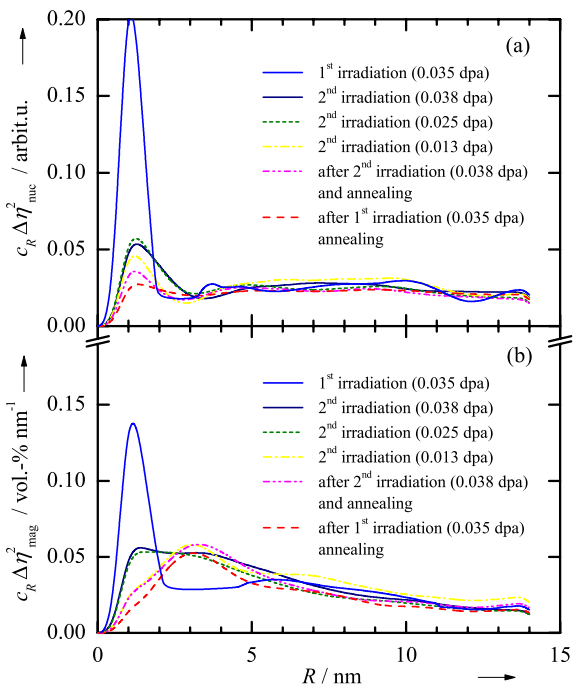

Abb. 6 Volumenverteilungsfunktionen von Streuzentren berechnet aus den Streukurvenverläufen der Abb. 5 skaliert mit dem **(a)** Kernstreukontrast $\Delta\eta^2_{\mathrm{nuc}}$ und **(b)** magnetischen Streukontrast $\Delta\eta^2_{\mathrm{mag}}$.

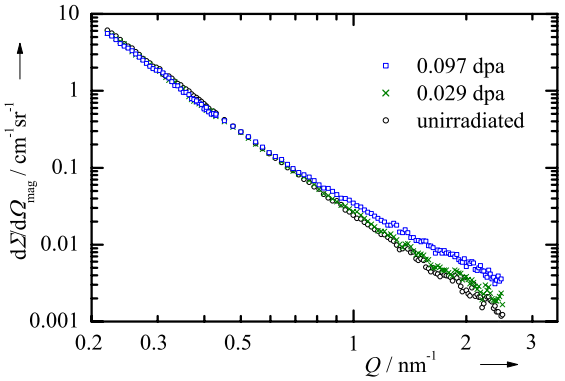

Abb. 7 Kohärente magnetische Streuwirkungsquerschnitte für den Werkstoff 15Kh2NMFAA (Charge D).

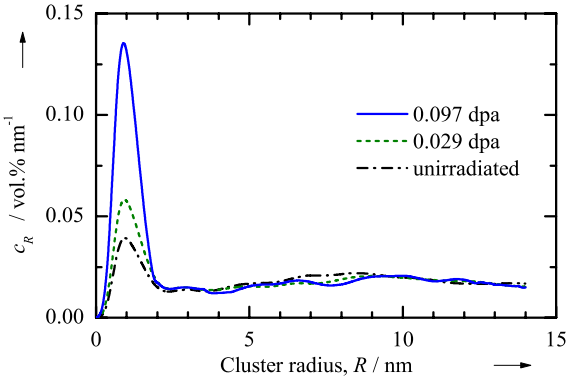

Abb. 8 Volumenverteilungsfunktionen von Streuzentren berechnet aus den Streukurvenverläufen der Abb. 7 für nicht-magnetische Teilchen.

dieser Strahlendefekte marginal. Es scheint einen Sättigungseffekt zu geben. Der mittlere Teilchenradius beträgt 1.2 ± 0.1 nm mit der Tendenz eines sehr geringen Teilchenwachstums mit zunehmender Strahlenbelastung. Der magnetische Streubeitrag ist im Verhältnis zum nuklearen Streubeitrag deutlich erhöht. Nach der Wärmebehandlung bei 475 °C werden wesentlich größere Streuzentren mit Radien bis zu 6 nm beobachtet. Ihr mittlerer Radius beträgt 2.5 nm. Den größten Volumenbeitrag stellen Teilchen mit einem Radius von 3 nm (siehe Maximum in der Volumenverteilungsfunktion der Abbildung 12).

Die aus den SANS-Messungen gewonnenen Parameter, Volumenanteil bestrahlungsinduzierter Cluster Δc, mittlerer Radius $\overline{R}$ und A-Verhältnis sind in Tab. 3 zusammengestellt. Zusätzlich enthält die Tabelle ausgewählte Ergebnisse der mechanischen Materialprüfung.

Tab.3 Ergebnisse der SANS-Experimente: bestrahlungsinduzierter Volumenanteil nicht-magnetischer Cluster Δc, mittlerer Clusterradius $\overline{R}$ und A-Verhältnis; Ergebnisse der mechanischen Prüfung: Änderung der Streckgrenze $\Delta R_{p0.2}$, der Härte ΔHV10 und der Sprödbruchübergangstemperatur $\Delta T_{T(48J)}$ in Bezug auf den unbestrahlten Referenzzustand.

Charge	Φ / 10^{21} cm^{-2}	Δc / Vol.-%	$\overline{R}$ / nm	A-Verhältnis	$\Delta R_{p0.2}$ / MPa	ΔHV10	$\Delta T_{T(48J)}$ / K
KAB (I-1)	0.0023	0.06 ± 0.01	1.0 ± 0.1	3.8 ± 0.2	51	32	50
KAB (I-2)	0.004	0.10 ± 0.01	1.0 ± 0.1	4.2 ± 0.2	118	30	
KAB (I-3)	0.009	0.16 ± 0.01	1.0 ± 0.1	3.7 ± 0.2	134	44	
KAB (I-4)	0.080	0.26 ± 0.01	1.0 ± 0.1	3.1 ± 0.1	190	69	108
KAB (I-5)	0.143	0.27 ± 0.01	1.0 ± 0.1	2.9 ± 0.1	234	74	
VTT (I)	0.035	0.09 ± 0.01	1.0 ± 0.1	1.6 ± 0.2	170	31	112
VTT (IAI-1)	0.013	0.02 ± 0.006	1.0 ± 0.1	2.2 ± 0.1	78	24	50
VTT (IAI-2)	0.025	0.04 ± 0.007	1.0 ± 0.1	2.2 ± 0.1	118	23	76
VTT (IAI-3)	0.038	0.05 ± 0.007	1.0 ± 0.1	2.2 ± 0.1	83	29	116
D (I-1)	0.029	0.02 ± 0.005	1.0 ± 0.1	2.8 ± 0.1	33	9	18
D (I-2)	0.097	0.09 ± 0.01	1.0 ± 0.1	2.8 ± 0.1	102	40	58
ML-A (I-1)	0.010	0.02 ± 0.005	1.0 ± 0.1	1.7 ± 0.1	196	94	101
ML-A (I-2)	0.080	0.10 ± 0.01	1.0 ± 0.1	1.7 ± 0.1	256	123	126
ML-B (I-1)	0.010	0.31 ± 0.01	1.2 ± 0.1	5.3 ± 0.3	212	66	121
ML-B (I-2)	0.080	0.32 ± 0.01	1.2 ± 0.1	5.0 ± 0.3	189	79	121

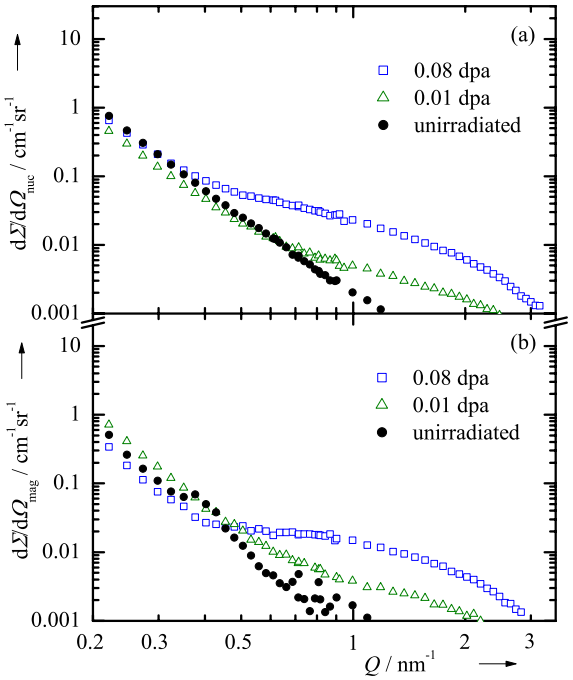

Abb. 9 Kohärente Streuwirkungsquerschnitte für die Eisenbasis-Modelllegierung ML-A: **(a)** nuklearer und **(b)** magnetischer Streuanteil.

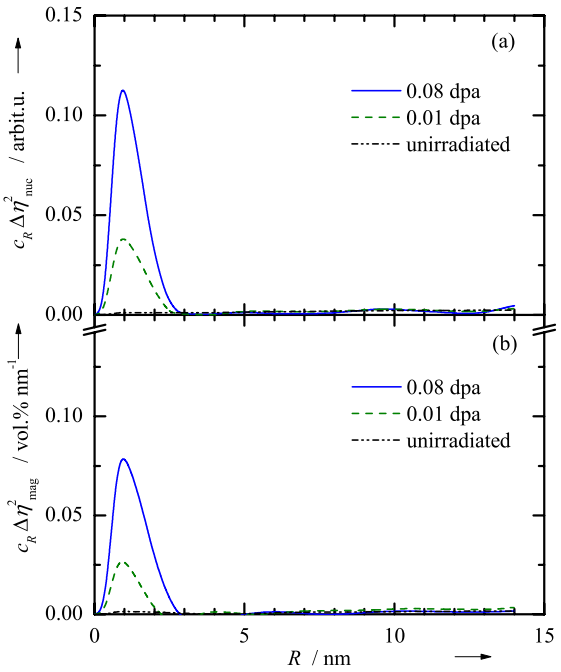

Abb. 10 Volumenverteilungsfunktionen von Streuzentren berechnet aus den Streukurvenverläufen der Abb. 9 skaliert mit dem **(a)** Kernstreukontrast $\Delta\eta^2_{nuc}$ und **(b)** magnetischen Streukontrast $\Delta\eta^2_{mag}$.

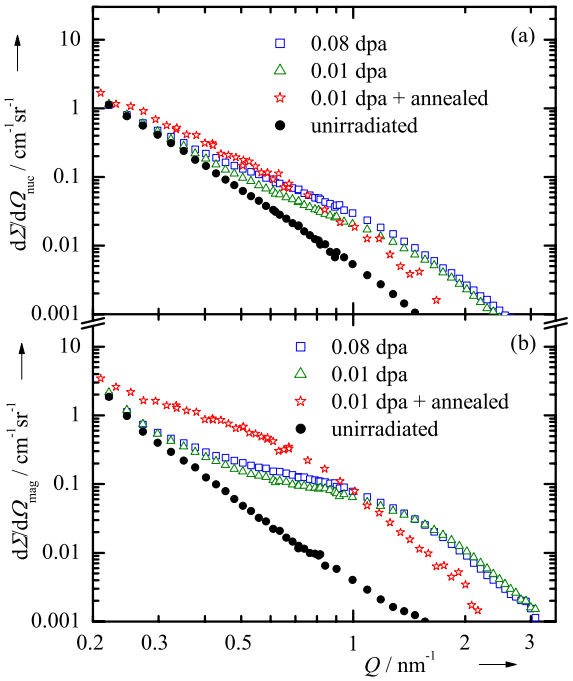

Abb. 11 Kohärente Streuwirkungsquerschnitte für die Eisenbasis-Modelllegierung ML-B: **(a)** nuklearer und **(b)** magnetischer Streuanteil.

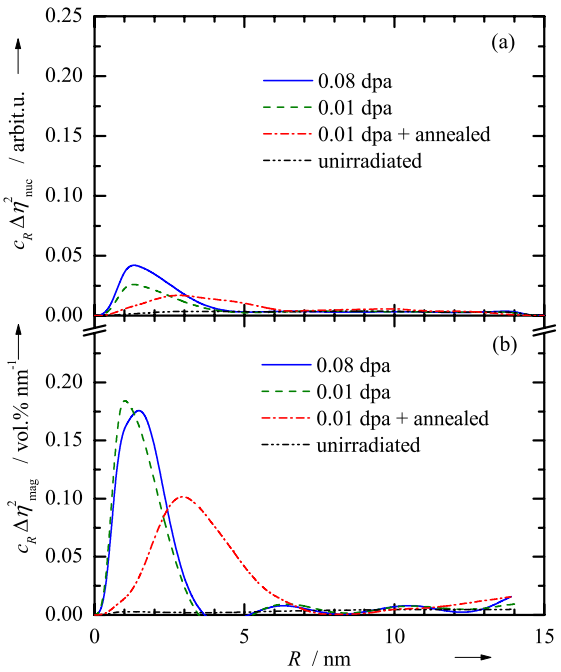

Abb. 12 Volumenverteilungsfunktionen von Streuzentren berechnet aus den Streukurvenverläufen der Abb. 11 skaliert mit dem **(a)** Kernstreukontrast $\Delta\eta^2_{nuc}$ und **(b)** magnetischen Streukontrast $\Delta\eta^2_{mag}$.

4 Diskussion

Aus der Abb. 1 geht hervor, dass die Streuintensität der bestrahlten Zustände des Materials KAB im Vergleich zum unbestrahlten Zustand im Q-Bereich > 0.5 nm^{-1} erhöht ist. Dies trifft sowohl für den magnetischen als auch für den nuklearen Streuanteil zu. Die Kongruenz des Kurvenverlaufs beider Streuanteile erlaubt die Schlussfolgerung, dass sowohl die magnetische als auch die nukleare Streuung an den gleichen Objekten erfolgt.

Der Bestrahlungseinfluss sowie die Relation zwischen magnetischem und nuklearem Streuanteil werden in den in Abb. 2 dargestellten Größenverteilungen der Streuzentren noch deutlicher sichtbar. Das ausgeprägte Maximum in den Verteilungen der bestrahlten Zustände ist offensichtlich auf die Bildung von Strahlendefekten zurückzuführen. Dabei handelt es sich um ausgedehnte Objekte, deren mittlerer Radius (Kugelform vorausgesetzt) etwa 1 nm und deren maximaler Radius etwa 3 nm beträgt. Ihr Volumenanteil, gegeben durch die Fläche unter dem Peak, nimmt mit steigender Neutronenfluenz monoton zu, während sich deren Größe nicht oder nur geringfügig ändert.

Aus Abb. 2 geht auch hervor, dass sich die mit dem magnetischen und nuklearen Streukontrast skalierten Größenverteilungen in ihrer relativen Höhe unterscheiden. Dieser Sachverhalt spiegelt sich im A-Verhältnis wider (siehe Tab. 3). Volumenanteil Δc und A-Verhältnis sind in Abb. 13 in Abhängigkeit von der Neutronenfluenz Φ dargestellt. Zunächst nimmt dieser Volumenanteil rasch zu (bis etwa $\Phi = 0.01 \cdot 10^{21}\,cm^{-2}$). Oberhalb $0.08 \cdot 10^{21}\,cm^{-2}$ ändert er sich nur noch geringfügig. Inwieweit bereits bei $0.143 \cdot 10^{21}\,cm^{-2}$ eine Sättigung der Bildung von bestrahlungsinduzierten Clustern erreicht ist, kann anhand der Messdaten nicht sicher entschieden werden. Die Annahme, dass es sich bei den bestrahlungsinduzierten nicht-magnetischen Objekten mit 0.26 Vol.-% um reine Cu-Cluster handelt, würde bedeuten, dass bei einer Besetzung der Fe-Gitterplätze durch Cu-Atome 0.29 Masse-% Cu in den streuenden Objekten angehäuft sind. Dies übersteigt jedoch den Wert des gesamten Cu-Gehaltes der Matrix (Tab. 1). Die mögliche Ausscheidung von Cu infolge der Bestrahlung kann den gefundenen Anteil an Strahlendefekten demnach nicht ausreichend erklären. Die vereinfachende Annahme reiner Cu-Cluster widerspricht auch den Messergebnissen zum A-Verhältnis der Strahlendefekte. Dieses fällt mit zunehmender Fluenz von Werten über 4 auf Werte unter 3 ab (Abb. 13). Reine Cu-Cluster ergeben nach Gl. (3) ein A-Verhältnis von 12. Wird ebenfalls vereinfachend für alle Strahlendefekte ein Modell von binären Leerstellen-Cu-Clustern zugrundegelegt, dann ergibt sich nach Gl. (3) eine Abhängigkeit des A-Verhältnisses vom Cu-Anteil v wie in Abb. 14 dargestellt. Der Vergleich mit dem experimentellen Befund (Abb. 13) zeigt, dass der Cu-Anteil in den Strahlendefekten im Rahmen der Gültigkeit des zugrundegelegten Modells mit zunehmender Fluenz von etwa 80 % auf etwa 65 % abfällt. Das kann so gedeutet werden, dass zunächst Cu-reiche Cluster gebildet werden. Mit Verarmung der Matrix an Cu nimmt der mittlere Cu-Anteil der Cluster ab und es

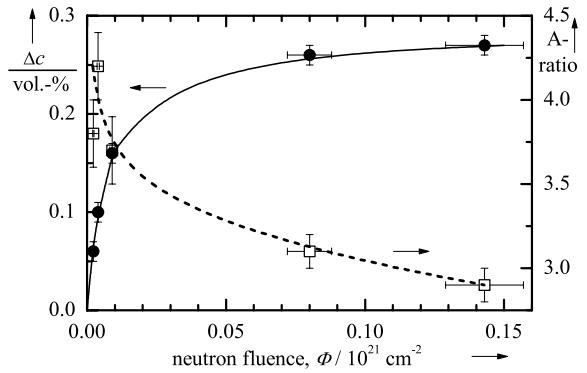

Abb. 13 Abhängigkeit des Volumenanteils an Strahlendefekten und deren A-Verhältnis von der Neutronenbestrahlung für das Material KAB.

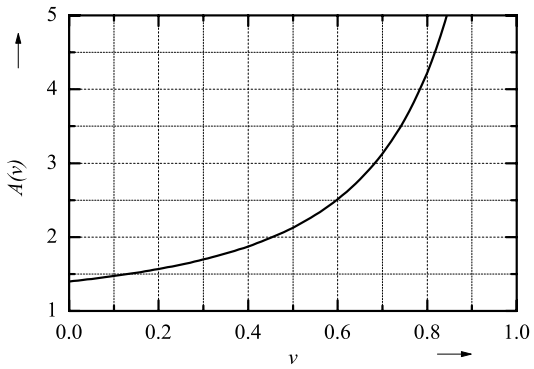

Abb. 14 A-Verhältnis für Leerstellen-Cu-Cluster im RDB-Stahl in Abhängigkeit vom Cu-Anteil v innerhalb des Clusters.

bilden sich immer weniger. Es kommt zum beobachteten Sättigungseffekt. Die ermittelten *A*-Verhältnisse unterscheiden sich immer noch deutlich vom Wert für Poren von 1.4 (entsprechend $v = 0$ in Abb. 14).

Erstmals konnten im Rahmen dieser Arbeit SANS-Messungen zur Untersuchung des Wiederbestrahlungsverhalten von RDB-Material durchgeführt werden. Hierfür stand ein WWER-440 Schweißwerkstoff (Charge VTT) zur Verfügung, der nach einer Neutronenbelastung von 0.035 dpa ausheilwärmebehandelt und anschließend mit bis zu 0.038 dpa wiederbestrahlt wurde. Die infolge der ersten Bestrahlung gebildeten Cluster mit einem *A*-Verhältnis von 1.6 sind nach der Ausheilwärmebehandlung verschwunden (Abb. 4). Zusätzlich trat im ausgeheilten Zustand gegenüber dem Ausgangszustand eine geringfügige Änderung in der aus dem magnetischen Streubeitrag berechneten Größenverteilung von Streuzentren bei $R \approx 3$ nm auf. Diese Veränderung war im Kernstreuanteil nicht nachweisbar. Es handelt sich dabei also um eine Population, die ein hohes *A*-Verhältnis hat. Die Gefügestruktur nach der erster Bestrahlung und Ausheilwärmebehandlung ist demnach nicht exakt dieselbe wie die des unbestrahlten Referenzzustandes. Durch die erneute Bestrahlung kommt es wieder zur Bildung von Clustern mit Radien bis zu 2 nm. Ihr *A*-Verhältnis beträgt jetzt 2.2, woraus sich eine andere atomare Zusammensetzung ergibt. Im Vergleich zur ersten Bestrahlung bei ähnlicher Neutronenbelastung ist der Anteil dieser neu gebildeten Cluster aber wesentlich kleiner (Abb. 6). Eine abermalige Wärmebehandlung löst die Strahlendefekte ebenfalls wieder auf. Aus Sicht der SANS-Ergebnisse mit dem quantitativen Nachweis von bestrahlungsinduzierten Clusteranteilen, die größer als 0.5 nm im Radius sind (Nachweisgrenze), erscheint das RDB-Material nach einer Ausheilwärmebehandlung weniger strahlenanfällig.

Der WWER-1000 RDB-Stahl (Charge D) unterscheidet sich von den WWER-440 RDB-Stählen in seiner chemischen Zusammensetzung. Der Ni-Anteil ist mit über 1 Masse-% deutlich erhöht und der Gehalt an dem Karbidbildner Vanadium geringer (0.1 % statt 0.3 %). Die gemessenen SANS-Kurven und die daraus bestimmten Größenverteilungen an Strahlendefekten (Abbn. 7 bis 8) sind denen der WWER-440 Stähle (Abbn. 1 bis 4) trotzdem ähnlich. Das *A*-Verhältnis der bestrahlungsinduzierten Cluster von 2.8 ist aufgrund des niedrigen Cu-Gehaltes der Matrix (0.03 Masse-%) nicht mit dem einfachen Modell von binären Leerstellen-Cu-Clustern (Abb. 14) erklärbar. Cluster bestehend aus Leerstellen mit Mn- und Ni-Anreicherungen können dieses *A*-Verhältnis bewirken.

Die Abhängigkeit des Volumenanteil an bestrahlungsinduzierten Clustern von der Neutronenfluenz ist in Abb. 15 dargestellt. Darin enthalten sind zum direkten Vergleich zusätzlich Ergebnisse von zwei weiteren WWER-1000 Stählen, welche aus vorangegangenen Untersuchungen stammen. Es ist zu erkennen, dass aufgrund der um eine Größenordnung höheren

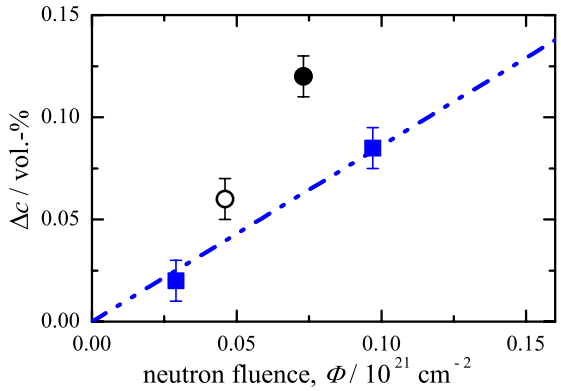

Abb. 15 Fluenzabhängigkeit des Volumenanteils bestrahlungsinduzierter Cluster für WWER-1000 Grundwerkstoffe (blaue Quadrate Charge D).

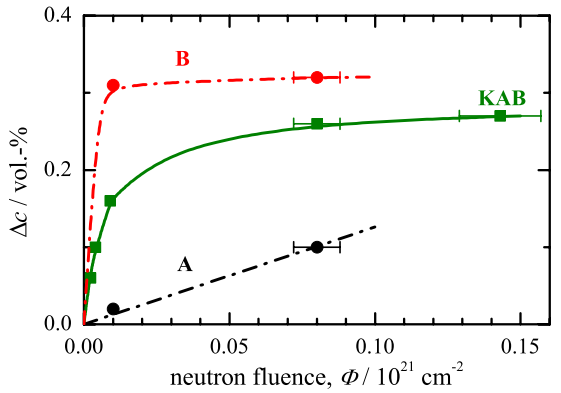

Abb. 16 Fluenzabhängigkeit des Volumenanteils bestrahlungsinduzierter Cluster für die Eisenbasis-Modelllegierungen ML-A und -B sowie den WWER-440 Stahl, Charge KAB.

Neutronflussdichte für die Charge D, der Volumenanteil an bestrahlungsinduzierten Clustern geringer ausfällt. Es erfolgt im Gegensatz zum WWER-440 Stahl (siehe Abb. 13) eine kontinuierliche Zunahme des Strahlendefektanteils mit der Neutronenfluenz.

Kontinuierlich nimmt auch der Strahlendefektanteil in der Eisenbasis-Modelllegierung ML-A zu (siehe Abb. 16) und das *A*-Verhältnis der Strahlendefekte von 1.7 in dieser Modelllegierung deutet auf leerstellenreiche Cluster hin, während die Modelllegierung ML-B (0.42 Masse-% Cu) bereits nach der ersten Bestrahlung einen deutlich erhöhten Anteil an Clustern (0.31 Vol.-%) hat, der im zweiten Bestrahlungszustand nur noch geringfügig ansteigt (auf 0.32 Vol.-%). Das *A*-Verhältnis dieser Cluster weist mit einem Wert ≥ 5 auf eine völlig andere Zusammensetzung hin (Cu-reiche Cluster).

5 Zusammenfassung

- Nahezu unabhängig vom Werkstofftyp treten im wesentlichen Cluster mit Radien bis zu 3 nm auf. Ihr mittlerer Radius nach Strahlenbelastungen, welcher ein WWER-RDB-Stahl innerhalb seiner ausgelegten Gesamtbetriebszeit ausgesetzt ist, beträgt (1.0 ± 0.1) nm (Ausnahme Cu-reiche Eisenbasis-Modelllegierung ML-B).
- Der Volumenanteil an Clustern steigt mit der Strahlenbelastung monoton, aber im allgemeinen nicht linear an. Wegen der Konstanz des Clusterradius trifft diese Aussage auch auf die Anzahldichte zu. In Abhängigkeit von der chemischen Zusammensetzung der Werkstoffe wurden bei vergleichbarer Strahlenbelastung deutliche Unterschiede im Volumenanteil festgestellt.
- Der Cu-Gehalt der Werkstoffe beeinflusst den Volumenanteil an bestrahlungsinduzierten Clustern am stärksten, was die besondere Rolle dieses Elements bei der bestrahlungsbedingten Materialalterung bestätigt.
- Mindestens zwei Typen von Leerstellen/Fremdatom-Clustern wurden identifiziert, die sich in ihrer Zusammensetzung und ihrer Bildungskinetik unterscheiden. Das Vorliegen von reinen Cu-Ausscheidungen kann definitiv ausgeschlossen werden.
- Eine Wärmebehandlung oberhalb der Bestrahlungstemperatur reduziert den Volumenanteil an bestrahlungsinduzierten Clustern, oftmals bis hin zu deren vollständiger Auflösung.
- Bei relativ hohen Cu-Gehalten der Werkstoffe (über 0.2 Masse-%) tritt bei Ausheilwärmebehandlungen eine Vergröberung von Clustern in Konkurrenz zu deren Auflösung.
- Eine Ausheilwärmebehandlung beeinflusst die Strahlenanfälligkeit der Werkstoffe bei Wiederbestrahlung. Nach der Wärmebehandlung wurde bei erneuter Bestrahlung mit schnellen Neutronen eine geringere Strahlenanfälligkeit in bezug auf die Anteil der im Werkstoff neu gebildeten Defekte festgestellt.

6 Literatur

[1] A. Ulbricht, Untersuchungen an neutronenbestrahlten Reaktordruckbehälterstählen mit Neutronen-Kleinwinkelstreuung, Dissertation, TU BA Freiberg, 2006.

Theoretical investigation on the kinetics of radiation-induced defect evolution related to VVER condition

Stay report by Dr. Vladimir A. Borodin

(RRC Kurchatov Institute, Moscow)

FZ Rossendorf, 2 May - 20 June 2004

Background

Our analytical model of the effect of radiation on embrittlement implies that the modification of crack propagation mode from ductile to brittle occurs because irradiation suppresses the development of plastic zones at the tips of microcracks, which can propagate in the tested specimen. A plastic zone develops at the crack tip as a result of dislocation emission from the tip and dislocation movement under the effect of stresses concentration around the tip. The size of the plastic zone is determined by the balance between the elastic stresses acting on dislocations and the strength of the barriers that counteract dislocation propagation. The distribution of stresses promoting dislocation motion is mainly affected by crack geometry and size, which have no direct relation to irradiation. On the other hand, the irradiation is able to modify the number density and strength of the barriers for dislocation motion.

Indeed, when a dislocation is pinned by incoherent precipitates or voids of radius R and number density N_b, the yield stress (that is, the stress required to detach dislocation from pinning defects), σ_y , is given by

$$\sigma_y \approx \mu a (N_b R)^{1/2}, \quad (1)$$

where μ is the steel shear modulus and a – the lattice parameter. In other words, the increase of either barrier size, or barrier number density increases the yield stress and thus decreases the steel ductility.

These considerations can be applied equally well to plastic zones around propagating crack tips, as long as the plastic zone comprises many dislocations and many barriers for dislocation motion. However, crack tip plastic zone has very specific shape – a thin long cylinder with an intricate cross-section, whose typical transverse size does not exceed ~ 1 μm. Correspondingly, the barriers responsible for the macroscopic yield stress modification – such as standard second-phase particles in an unirradiated material (various carbonitrides, oxides and sulphides) - can not noticeably modify the yield stress inside the crack tip plastic zone, because the sizes of these barriers are normally bigger or comparable to 1 μm, while their number densities are too low. Moreover, our fractographic study in the framework of the project, as reported earlier, indicate that propagating cracks prefer to pass around big precipitates, avoiding any direct interaction. Hence, in order to be able to interpret the ductile-to-brittle transition under irradiation in terms of local plasticity suppression, we are interested in the small (several nm large) barriers for dislocation motion that can be produced by irradiation in sufficiently big amounts.

As it has been demonstrated by SANS measurements performed in FZR, neutron irradiation indeed creates in RPV steels some features that can fit into the above-mentioned model. These features are sufficiently small (approximately 2 nm in size) in comparison to the crack tip plastic zone dimensions and do not grow with time. On the other hand, their number density grows approximately linearly with the fluence, which guaranties that after a certain dose eq. (1) becomes applicable in the crack tip plastic zone. After this threshold dose the local yield stress at the crack tip will increase as approximately square root of irradiation dose. The increase of the local yield stress should lead to the shrinkage of the plastic zone size and hence – to more brittle crack propagation at the fixed values of other parameters (the most important among these parameters being the test temperature). Not going too much into details of the analytical model (these can be found in other earlier reports on the project), we may ask ourselves, what these features might be and to which degree could they affect the efficiency of dislocation emission from the crack tip and the mobility of dislocations in the crack tip vicinity?

One of the most natural assumptions is that the features observed by SANS are somehow related to collision cascades. Indeed, fast neutrons (with energies exceeding 0.1 MeV) are able to transfer to some lattice atoms sufficiently high energies, knocking them off their lattice positions. These primary knock-on atoms (PKAs) collide with neighbouring atoms, which in turn collide with their own neighbours, etc, until a small region of highly mobile atoms (resembling very much a drop of overheated liquid) is formed. Due to the interaction with the surrounding matrix the internal energy contained in the liquid-like central zone of the cascade dissipates and the central zone cools down, so that after ~2ps from the moment of PKA creation the atoms inside the cascade are again in the solid state. The majority of atoms returns to normal lattice positions, but due to the very high cascade cooling rate the order is not completely restored. At the periphery of the cascade one can find a number of individual interstitials and small interstitial clusters, while vacancies are located preferably in the center of a cascade (see Fig. 1a). These "post-dynamic" cascade damage structures have typical sizes *d* of the order of 2-5 nm, which correlates quite well with SANS observation.

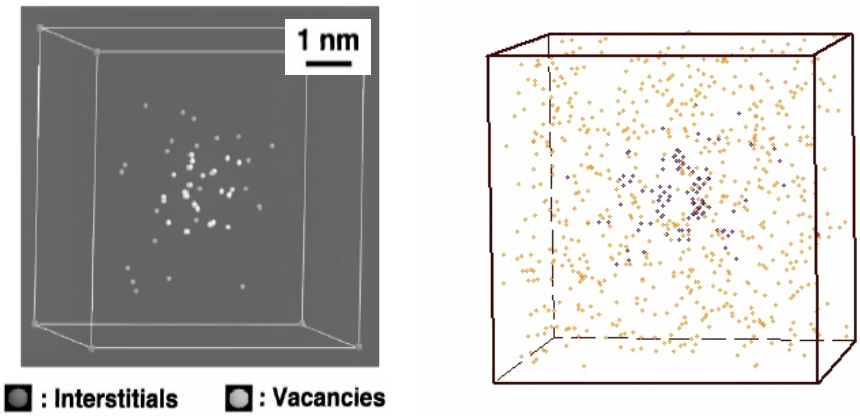

(a) (b)

Fig.1. (a) A typical structure of radiation damage remaining after the cascade cooling down. Results of MD simulations by Sekimura et al. [1]. (b) 3D Gaussian distribution of vacancies (dark) and random distribution of copper atoms (yellow) in a LKMC simulation cell.

Unfortunately, in bcc iron both vacancies and interstitials are highly mobile (the migration energy of a vacancy is, according to different estimates, in the range of E_{mV} ~0.6 – 1.1 eV, while that of an interstitial is less than E_{mI} ~ 0.1 eV). Correspondingly, the typical dissolution time of "post-dynamic" structure, as determined by slower defects (vacancies), can be roughly estimated as

$$\tau_{pd} \approx \left(d^2 / D_{V0}\right) \exp(E_{mV} / k_B T), \qquad (2)$$

where D_{V0} is the preexponential of vacancy diffusion coefficient, k_B – the Boltzmann factor and T – the material temperature. Assuming D_{V0} ~ 1 cm^2/s, E_{mV} ~0.68 eV [2,3] and irradiation temperature of 300^{o}C, one gets τ_{pd} ≈ 0.1 μs. Even having in mind the roughness of the estimate, the dissolution time is too short to allow the linear increase of the number density of "post-dynamic" cascade damage structures with dose.

On the other hand, RPV steels are complex Fe-Cr alloys containing many alloying elements (such as Ni, Cu, Mn, Si, P, etc.) in solid solution. The dissolution of cascade remnants can create a local redistribution of atoms in the cascade zone, which lives much longer than the "post-dynamic" cascade damage. Indeed, investigations by tomographic atomic probe (TAP) and atomic probe field ion microscopy (APFIM) [4,5] demonstrate that after neutron irradiation one can find in the specimens high number densities of local zones having

noticeable enrichment with some alloy components (in particular - Cu,Ni,Si,P), as compared to the average matrix concentration. The biggest relative enrichment is achieved with respect to copper, so these aggregates are usually referred to as "copper-reach zones". However, it should be kept in mind that the absolute copper concentration in these zones remains quite low and hence they should not be treated as copper precipitates, which are known to precipitate at noticeably higher temperatures. In fact, it is not quite clear what is the real microscopic structure of these zones. According to some Monte-Carlo calculations, these zones can contain an array of very small vacancy voids on equally small copper precipitates [6].

Research objectives

The objective of the research task was the clarification of the atomic structure of cascade remnants (copper-rich zones). This, in turn, would allow clarification of two other questions of practical importance:

(i) Can copper-rich zones result in the experimentally observed shape and intensity of SANS signal? The positive answer would allow a unique identification of the features observed by SANS.

(ii) Can copper-rich zones act as barriers for dislocation glide and what might be the strength of these barriers? The answer would give the input data for our analytical model dealing with the suppression of dislocation emission from crack tips.

Formulation of mathematical task and justification of approach

For mathematical simulation of the long-term (that is, at time scales noticeably exceeding cascade cooling down time, of ~ 0.1 ns) cascade annealing we have chosen the following model:

(i) *Initial conditions*

First of all, since the doses reached in the normal operation conditions of thermal nuclear reactors are much less than 0.01 dpa, the cascades practically do not overlap. So it is reasonable to assume that each cascade can be treated completely independently of the others. In order to investigate the evolution of an individual cascade, it is sufficient to consider a piece of the host matrix lattice (simulation cell) completely comprising the after-cascade defect distribution. Among the two components of the defect structure – vacancies and self-interstitials - only vacancies should be considered, since interstitials are very fast and, being located at the cascade periphery, quickly leave the cascade neighbourhood. The spatial distribution of vacancies can be quite nicely reproduced by a 3D Gaussian (see Fig. 1b), while the total number of vacancies remaining in the cascade (~ 100) can be borrowed from detailed MD simulations of cascades in pure iron [7]. The evident possible improvements (the use of exact vacancy distributions from MD runs and a two-component Fe-Cr host lattice) are not expected to influence the cascade dissolution kinetics very much. As far as copper atoms are concerned, their concentration in the matrix can be varied in the experimentally relevant range of (0.01 – 1 at.%), while copper distribution in the matrix can be considered as completely uniform. Indeed, in a virgin matrix substitutional copper atoms are distributed over the iron lattice sites completely at random and MD simulations for a system Fe-Cu demonstrate that the dynamic stage of the cascade does not change the randomness of copper distribution in the simulation cell [8].

(ii) *Kinetic pathways*

When the initial profiles of vacancies and copper are fixed, the vacancies should be allowed to make diffusion jumps. The frequencies of vacancy diffusion jumps depend on the vacancy proximity to copper atoms and to other vacancies, since vacancies and copper atoms are able to interact at distances up to the second nearest neighbours. The neglect of

this interaction can lead, as shown below, to completely incorrect kinetic pathways and resulting structures.

(iii) Simulation run duration

As vacancies reach the cell borders, they are absorbed by the surroundings. Alternatively, vacancies can be captured in small Cu-V clusters with quite high lifetimes (comparable to years, or ~ 10^7-10^8 s). Therefore, the simulation should be continued until all vacancies either leave the simulation cell, or become bound in long-living complexes.

The most tricky part of the model is the intermediate stage of vacancy diffusion. Having in mind the length and time scales involved, the most adequate approach is lattice kinetic Monte-Carlo (LKMC). Such a code has been developed in RRC Kurchatov Institute for a number of years, but in order to be applied to research in the framework of the project it had to be adjusted so as to reflect the most essential peculiarities of the modeled system. Before specifying these particular features, it makes sense to discuss the general requirements that must be implemented in LKMC code dealing with a physical problem that involves particle diffusion:

Table 1.

	Requirements to LKMC code	Availability prior to the stay	Availability after the stay
(i)	The code should properly describe the simulation lattice, in case of iron – bcc	+	+
(ii)	The code should correctly describe interaction of particles with the simulation cell environment	±	+
(iii)	The code should take into account the presence of several kinds of particles at a time	+	+
(iv)	The code should allow to specify appropriate initial distributions of jumping particles	-	+
(v)	The code should allow to track time evolution	+	+
(vi)	The code should properly express jump probabilities for individual particles on the lattice in terms of particle energies and environment parameters, such as temperature	±	+
(vii)	The code should consider particle interaction at relevant distances between particles	±	+

Now let us discuss the code requirements in more detail, having in mind its application to the aims of the project:

(i) A proper description of underlying crystalline lattice is self evident. Bcc lattice is among those implemented in the code from the very beginning of its development, so that needed no adjustment.

(ii) Interaction of particles with the simulation cell environment means the decision that the code makes, when a particle attempts to jump out of the cell. This is equivalent to specification of boundary conditions. Generally, several different kinds of boundary conditions can be imagined, such as *periodic* boundary conditions (a particle leaving the cell on one side reappears at the opposite side), *reflecting* (a particle is not allowed to jump out of the cell), or *absorbing* boundary conditions (jumping out of the cell the particle is lost forever).

(iii) Simultaneous treatment of several particle kinds is self-explanatory. The current version of the program allows to deal simultaneously with vacancies and 2 different types of atomic species, which is sufficient for the project tasks.

(iv) The code presents a variety of possibilities for specifying the initial distributions of particles. Initial distribution of each atomic species is generated independently of the others, with the only restriction that a lattice site can not be occupied by more than one particle (that is – by a vacancy or an atom of any kind).

(v) Time tracking is one of the most essential requirements to a good LKMC code, because it is possible only provided correct physical assumption about the system kinetics are used and allows to follow physically justified kinetic pathways of MC system evolution. Simplified versions of LKMC that do not track time are also frequently used thanks to their accelerated performance, but they predict kinetic pathways whose reliability can not be justified.

Let us considers a system of vacancies and copper atoms in iron matrix, each of these objects being able to participate in a certain number of events (in the simplest case – jumps from one position to another). Normally LKMC procedure consists in a repetition of essentially the same basic steps, each including selection and realization of one among possible events. Let us assume that after some LKMC step the system has got a certain configuration and the question is, how to long the system is going to stay in this configuration and which particular event will happen next? Different codes use different approaches, each approach having is advantages and drawbacks.

(a) *"Continuous time" algorithm*

The most reliable procedure used in modern LKMC codes is provided by the so called "continuous time" or "residence time" algorithm (see e.g. [9]). The reasoning is based on the consideration that the time Δt when the system remains in a certain configuration is essentially the time, during which no event happens, since after at least one event the system configuration changes and all the event probabilities should be updated to the new configuration. The probability P_m that a certain event m does not happen within time span Δt is given by

$$P_m = \exp(-p_m \Delta t)\,. \tag{3}$$

If all the events are statistically independent, which normally can be safely assumed, the probability P that no event happens within time span Δt is given by the product of individual probabilities (3),

$$P = \exp(-p\Delta t)\,, \tag{4}$$

where

$$p = \sum_{m=1}^{M} p_m\,. \tag{5}$$

Hence, where p is known, the selection of Δt can be made either within the whole time interval from 0 to infinity with a relative probability defined by equation (4), or in a simplified manner, assuming that Δt is close to the average time $\Delta\bar{t}$ required for at least one event to occur,

$$\Delta\bar{t} = \frac{\int_0^\infty t\exp(-pt)\,dt}{\int_0^\infty \exp(-pt)\,dt} = \frac{1}{p}\,. \tag{6}$$

The "residence time" algorithm commonly uses the latter possibility, assuming $\Delta t = \Delta\bar{t}$.

Certainly, defining the time between two consecutive events according to equations (4) or (6), we do not yet know, which particular event will occur. However, the MC code can select a particular event randomly from all available possibilities, weighted according to their relative contribution to the total frequency, p_m/p.

The advantages of the "residence time" algorithm are evident. It is founded on solid physical arguments and thus selects accurate kinetic pathways of system evolution. The approach is flexible, adjusting the duration of each MC step to the current state of the system. Each MC step is "successful" in the sense that it results in a new configuration of simulated objects. However, the price to pay is the necessity to update the frequencies of all possible events, which can require noticeable time, especially when jump frequencies are determined by interaction between particles separated by several interatomic distances.

(b) *Random sequential sampling*
An alternative to the residence time algorithm, which is also widely used in LKMC codes, is the selection of subsequent events with the help of a basic step that involves the following sequence of actions:

- an arbitrary object n is selected at random among all available,
- an arbitrary event m is selected among those associated with the chosen object,
- the selected event is performed with a probability equal to p_m/p_{max}, where p_{max} is the frequency of the fastest event among all the possible events that can happen in the system during its evolution.

The drawbacks of this approach are multiple, from both physical and computational points of view. The algorithm gives no clue to tracking the duration of individual MC events. The run duration in this algorithm is usually measured in Monte-Carlo steps (MCS), where 1 MCS corresponds to a sequence of N basic steps. Due to the unphysical selection of individual event, one can never be sure that the sequence of consecutive events selected by the algorithm corresponds to a realistic kinetic pathway. In fact, the only advantage of the algorithm is related to the fact that the event frequency at each basic MC step is estimated for only one selected event. Having in mind that calculation of jump frequencies is often a "bottleneck" of LKMC procedure, this trick is able to highly increase the efficiency of the code, even in spite of sometimes quite high percentage of "wasted" steps.

(vi) The definition of the frequencies of individual events is usually very straightforward, provided all the necessary input parameters are known. Indeed, when the elementary events are diffusional jumps, the general theory of diffusion predicts that the frequency p_m of a jump event can be expressed in the form of Arrhenius law,

$$p_m = p_0 \exp(-(E_{sp} - E_{in})/k_B T), \qquad (7)$$

where p_0 is some constant with dimension of inverse time, E_{sp} is the energy of the atomic system at the moment, when the atoms participating in the jump are in a "saddle point" configuration, and E_{in} – the energy of the atomic system before the jump. It should be kept in mind that except for the temperature, which can be treated as an adjustable parameter, the values entering this formula are external to MC program. Moreover, they depend often not only on two atoms that participate in the jump, but on their surroundings as well.

Evidently, in the most general form there is little chance to treat each individual jump exactly according to eq. (7), simply because the energies entering it can not be found exactly. Therefore, a number of physically reasonable approximations is commonly used. First of all, it is not necessary to treat the energies entering equation (7) as the total

energies of the system. In fact, we can chose a certain pair of exchanging particles as a "reference", assuming that the system with this pair of particles in the equilibrium (initial) configurations has energies E_0 and E_{sp0}, respectively, while the energies of other pair configurations can be measured as deviations from these reference values, $-E_{bi} = E_i - E_{i0}$ and $-E_{bs} = E_s - E_{s0}$. Second, though p_0 depends on the particular pair of jumping particles and sometimes on the chemical composition of the pair environment, it is a common practice to neglect the dependence on both. Having in mind these two approximations, we can reformulate equation (7) as

$$p_m = p_b \exp((E_{bs} - E_{bi})/kT) , \quad (8)$$

where

$$p_b = p_0 \exp(-E_{m0}/kT) \quad (9)$$

and $E_{m0} = E_{s0} - E_{i0}$ is the energy barrier for the reference jump.

Note that p_b is a common factor for all events and as such it does not influence the relative probability of an individual event. For this reason, the assignment of jump probabilities is normally performed with $p_b = 1$, while the correct value of p_b is calculated separately and is used for the conversion of MC time to the real time.

In principle, when binding energies for any particular configuration of objects participating in any particular event are known or can be borrowed from some database, the event frequencies are uniquely defined by equation (8). However, even the energies of equilibrium configurations, which are normally calculated straightforwardly, are seldom known for more than a small part of all possible configurations. As for the saddle-point energies, the input database is normally much worse, for the simple reason that it is much harder to measure or calculate them. Hence, one has to introduce some simplifications in order to be able to interpolate more or less reasonably all the variety of possible configurations, using only a "minimum set" of data, which should be available in any case.

We encounter therefore two questions:

(a) How to calculate the energy of two exchanging particles in an equilibrium state and in the saddle point of a diffusion jump, provided the surrounding configuration is known?

(b) How can we treat the jump probability, if there is no chance to find E_s?

The answer to question (a) is discussed farther in comment (vii), so here we restrict ourselves to the consideration of the most common models of approximating saddle point energies (these will be referred to below as *transition models*).

When the saddle-point energies are known for all possible events, we obtain *exact* transition model without any simplifications. But in reality, the saddle point values are most often unavailable or available only for some special events. On the other hand, the energies of particle in equilibrium lattice positions must be available in any case, being calculated either exactly, or in terms of a more or less reliable approximation. So one has to interpolate somehow the saddle point energy, using equilibrium values for system energy before and after the jump event.

Let us consider the variation of the system energy as a function of some "reaction coordinate", which allows to track instantaneous system state during the transition form the initial to the final jump configuration (for example, when vacancy jumps into a nearby position is considered, this reaction coordinate may be the instantaneous location of an

atom jumping to the vacancy, as measured along the line connecting the initial and final vacancy locations). Qualitatively, this profile looks like that shown in Fig. 2. In a general case, the energies of the system in the initial and final jump configurations, E_f and E_{in}, are different and the activation energies for the forward and backward jumps are different too. It is convenient to define the migration barrier as the difference between the saddle point energy and the biggest equilibrium energy among the final and the initial configurations,

$$E_m = E_{sp} - \max(E_i, E_f), \tag{10}$$

so that the jump from the less energetically favorable configuration requires overcoming of the energy barrier E_m and the jump from the more energetically favorable configuration – the barrier $E_m + E_b$, where $E_b = \left|E_{in} - E_f\right|$. As can be seen, the energy E_b is defined only by equilibrium energies, which are assumed to be known, so the approximation to be introduced relates only to the migration barrier of individual jump events. When the exact values of migration barriers are not known, the most widespread assumption is that the migration barrier is the same for all possible events, including the "reference" jump. Making use of equation (8) with p_b set equal to unity, the relative probability of a jump from the energetically unfavorable configuration should be set equal to unity, while that of the reverse jump – to $\exp(-E_b/k_BT)$. This method of relative jump probability assignment was originally proposed by Metropolis et al. [10], and can be refereed to as *Metropolis* transition model.

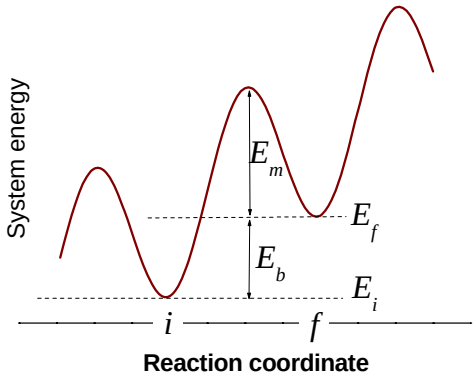

Fig. 2. Qualitative picture of the change of system energy with the variation of the system state during a jump event.

An alternative possibility is to assume that the saddle point energy remains the same for all jump events, so that the jump probabilities are given by

$$p_m = p'_b \exp(-E_{bi}/k_BT), \tag{11}$$

where

$$p'_b = p_0 \exp(-(E_s - E_{i0})/k_BT). \tag{12}$$

As before, we can set here $p'_b = 1$, introducing at the same time the appropriate scaling of MC step duration. This transition model is usually refereed to as *Kawasaki* model [11]. It is somewhat more straightforward than the Metropolis model, defining the event probability with the help of only the energy of initial jump configuration, but in practice it works worse than the Metropolis model and is thus much less used.

A certain improvement of Metropolis model is possible, when at least some information about the saddle-point energies is available. For example, in multi-component systems it is usually possible to estimate the activation energies of the direct position exchange of two particles on a perfect host lattice. It is then reasonable to assume that all the jump

events that involve a certain pair of particles have the energy coinciding with that for the same jump in a perfect lattice. In this case the jump probabilities should be defined directly from equation (8). In particular, it is known that vacancy-copper exchange in iron requires much lower energy as compared to the reference event, that is – vacancy exchange with a nearby host atom.

(vii) In contrast to saddle-point energies, which are really hard to obtain numerically, the energy of an equilibrium configuration in relevant physical systems can be obtained rather straightforwardly, e.g. by molecular statics, or by ab-initio methods. The common problem is, however, that the "configuration" of atoms influencing the frequency of a jump event includes not only the pair of particles that exchange their positions, but also particles located in lattice sites in the vicinity of the exchanging pair. In all cases this "vicinity" includes nearest neighbours of both jumping particles, but sometimes also second, third and higher-order neighbours can contribute to the energy of equilibrium configuration. In reality, one has at hand usually only very limited information, such as the formation energy of an individual diffusing particle in an otherwise perfect lattice and the energy of bonding between two particles of the same kind (a "like" dimer) or of different kinds ("unlike" dimers, appearing when more than one particle type is present, or when the lattice is not monatomic). For this reason the equilibrium energies are usually also approximated using available information about the energies of a limited number of particle configurations.

The most common approximation uses essentially the same idea as Molecular Dynamics simulations, namely, that the interaction of a particle with the surrounding atoms can be decomposed into a sum of pair-wise interactions, which are conveniently interpreted in the framework of a so-called "bond" model. This model assumes that all atoms located at distances below some threshold value from one another are connected between themselves by bonds, either real (e.g in the case of covalent solids) or fictitious. Each bond is assumed to have its own energy that depends only on the chemical nature of two atoms terminating the bond and on the bond length (in crystals the allowed bond lengths form a discrete set, which can be uniquely indexed by indicating to which nearest neighbour shell of one atom belongs the other one). In the bond model approximation the energy of the crystal can by written down as

$$E_{tot} = \sum_k \sum_{A,B} z_{AB}^{(k)} E_{AB}^{(k)} ,$$

where $z_{AB}^{(k)}$ is the number of bonds connecting atoms of type *A* and *B* (in our particular case *A,B* = Fe, Cu or a vacancy) located at the separation corresponding to neighbour shell *k*. In MC calculations with the invariable total number of participating particles it is convenient to characterize each bond not by its absolute energy, but by the energy gain reached when the distance between the pair of interacting atoms noticeably exceeds the size of their interaction domain,

$$G_{AB}^{(k)} = (E_{AH}^{(k)} - E_{HH}^{(k)}) + (E_{BH}^{(k)} - E_{HH}^{(k)}) - (E_{AB}^{(k)} - E_{HH}^{(k)}) , \qquad (13)$$

where *H* stands for a host atom (iron), while A and B are particles different from the host (that is, Cu atoms or vacancies). Then the defect energy change after a jump involving vacancy exchange with atom of type *A* (*A* = Fe,Cu) can be written down as

$$E_f - E_{in} = \sum_k [(i_{VCu}^{(k)} - f_{VCu}^{(k)}) G_{VCu}^{(k)} + (i_{VV}^{(k)} - f_{VV}^{(k)}) G_{VV}^{(k)}] \qquad (14)$$

where $i_{VA}^{(k)}$ and $f_{VA}^{(k)}$ are the number of A-type atoms in *k*-th coordination shell around the jumping vacancy in its initial and final position, respectively.

Summing up, in order to perform transitions between different configurations of individual defects in a small complex, MC program needs generally a set of 3 energy gain values (VV, CuV and CuCu) for each considered bond length.

Description of work during the stay

a. *Code modification*

The main aim of the work during the stay was to adopt the available LKMC code to particular conditions of the mathematical task. The adoption was related in particular to the following code requirements, as enumerated in Table 1:

(ii) The initial version of the code implemented only periodic and reflecting boundary conditions. However, according to the mathematical model, the most appropriate boundary conditions for vacancies would be those absorbing, because a vacancy that escapes the simulation cell is most probably lost forever. During the stay, absorbing boundary conditions were implemented in the code, but not yet tested.

(iv) The initial spatial distributions of particles generated by the code before the stay included completely uniform lattice filling with a specified concentration of particles and filling of various rectangular and ellipsoid-like regions. These were sufficient to reproduce the initial copper distribution in the matrix, but in order to describe the cascade-like initial distribution of vacancies a 3D Gaussian initial profile generation was implemented.

(vi) As indicated by existing ab-initio [12] and MD [2] simulations the exchange of positions between a vacancy and a cooper atom requires much lower activation energy than vacancy jump in the host iron matrix. Therefore, it is important for the studied task that the LKMC code were able to treat properly the difference in the exchange barriers of different chemical species. During the stay this was implemented in the framework of the modified Metropolis algorithm, namely the code is able to select the jump barrier depending on the kinds of particles exchanging their positions.

(vii) The biggest part of the work constituted the development of appropriate numerical means for treating interaction between different diffusing species at separations up to the third coordination sphere. This was an important development of the code in comparison to the traditional scheme, when only bonds to nearest neighbours of jumping pair are considered (see e.g. [3]). Indeed, according to recent ab-initio calculations [12], both vacancy-vacancy and copper-vacancy pairs efficiently interact not only as first nearest neighbours, but as second nearest neighbours as well.

b. Investigation of basic mechanism of copper diffusion

Modifications introduced in the code allow its application to large-scale modeling. However, in order to obtain reliable results the code should be extensively tested in various regimes and for various combinations of parameters. This testing requires adequate computing resources and time. Since the main time of the stay was devoted to the code development, only initial testing of the code on a physical task was performed. This physical task is, however, important for the subsequent predictions of the cascade dissolution kinetics.

The studied task was related to investigation of the mechanism of copper diffusion. Copper is a substitutional impurity in iron and hence the jumps of copper atoms are mediated by vacancies. In general, two mechanism of substitutional impurity diffusion are possible. The

first one is realized, when the interaction between substitutional atom and a vacancy is negligible. Then a jump of the substitutional atom occurs only when a vacancy appears in the first nearest neighbour shell of the atom, exchanges positions with the atom and then jumps away. As a result, one event of vacancy encounter with a substitutional atom can shift the atom by maximum one interatomic distance and, moreover, not every encounter leads to the shift of substitutional atom due to correlation effects. The same qualitative picture holds true, when substitutional atom is attracted to a nearest-neighbour vacancy, only the atom-vacancy pair lifetime in a bound state increases as compared to the case of vanishing interaction.

On the other hand, when a vacancy is attracted to a substitutional atom at distances bigger than the first nearest neighbour (NN) separation, then even jumping off of the atom, the vacancy remains bound to it. As a result, it is much more probable that at the next jump the vacancy returns back to the atom than jumps away into the bulk. If, additionally, the returning vacancy has more than one way for return, it can repeat the sequence of jumps to and from the substitutional atom again and again, appearing from different sides of the atom and providing a possibility of atomic jumps in different directions (see Fig. 3). Such mechanism of substitutional atom-vacancy diffusion in the form of a bound pair is known in the literature as "ring" mechanism [13]. Depending on the vacancy-atom exchange efficiency and on the lifetime of the bound state, one vacancy is able to provide the shift of substitutional atom to distances noticeably exceeding one interatomic separation.

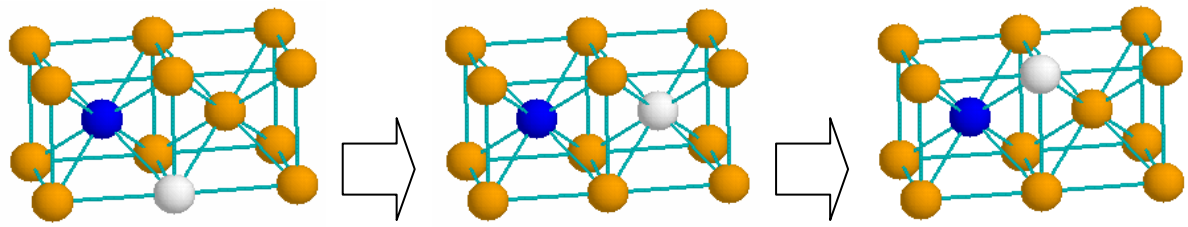

Fig. 3. A sequence of vacancy (white) jumps around a substitutional atom (blue) in a ring mechanism: 1st NN – 2nd NN – 1st NN with a different orientation of the pair.

From the point of view of cascade decomposition, copper enrichment in the central zone of the cascade, not to speak about copper clustering, requires noticeable copper mobility during the time of vacancy core dissolution in the surrounding matrix. It is, therefore, important, whether the ring mechanism of copper-vacancy diffusion can be realized, how long it the lifetime of the bound state and how far a copper atom can jump from the position, where it is found by a freely migrating vacancy.

The study of the vacancy-copper migration history by LKMC simulation required first of all the definition of input interaction energies. The literature search has demonstrated that the information concerning the copper-vacancy interaction is quite limited. The summary of available data is presented in Table 2.

Table 2. Interaction energies between Cu atoms and Vacancies in the first and second NN shells, as well as the differences between the vacancy-copper and vacancy iron migration barriers (migration gains), in eV, according to different sources.

	Cu-Cu			V-Cu			V-V		
	LS	BD1	BD2	LS	BD1	BD2	J	BD1	BD2
1 NN	0.2	0.17	0.14	0.184	0.11	0.16	0.13	0.06	0.15
2 NN		0.09	0.03	0	0.10	0.18	0.20	0.15	0.29
Migration gain				-0.44	-0.12	-0.12			

LS – from [3]; DB1 – from [12], ab-initio calculations for fully relaxed 54 atomic simulation cell; DB2 - from [12], ab-initio calculations for volume-conservative 128 atomic simulation cell; J – from [2]

LKMC simulations were performed for all 3 datasets presented in Table 2. It was found that the lifetime of a bound complex Cu-V depends on temperature, Fig. 4. At the relevant temperature of 300°C the expected lifetime of the complex is at least an order of magnitude larger than the expected time of cascade vacancy core dissolution, as estimated from equation (2). But nevertheless, even assuming that a vacancy interacts with several copper atoms before it leaves the simulation volume, we may expect that the vacancy core lifetime remains much smaller than the operation times of nuclear reactor structures.

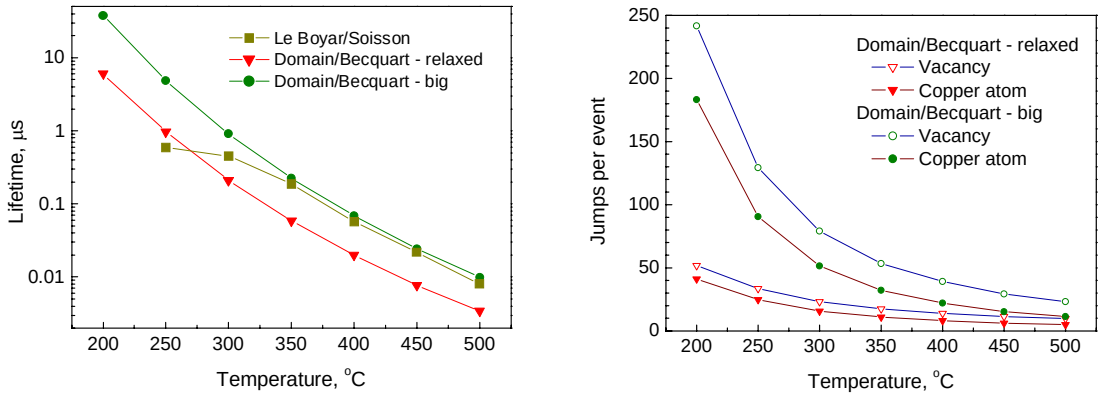

(a) (b)

Fig. 4. The lifetime of a bound complex Cu-V (a) and the number of jumps in a bound state (b) predicted for different sets of input parameters, as specified in Table 2.

On the other hand, for LS dataset the ring mechanism is impossible, because this dataset does not include 2nd NN interaction. However, for two other datasets quite noticeable numbers of both vacancy and copper atom jumps before the pair dissociation is expected. The average shift of Cu atoms during the bound pair lifetime at 300°C was found to be 2-3 interatomic distance, but this number is not very reliable due to the rather limited statistics. In any case the variance of the copper shift is quite noticeable and in some MC runs copper atoms shifted by 8-10 interatomic distances. At experimentally relevant copper concentration of 0.1at.% this would allow encounters of bound Cu-V pair with another copper atom already within the lifetime of the bound complex, which should promote efficient copper clustering. However, more reliable predictions can be obtained only after large-scale calculations will be performed later during the project duration.

Summary

1. Assuming that irradiation can modify the threshold temperature for brittle fracture by influencing the local plastic zones at crack tips, we have demonstrated that the most probable barriers for dislocation emission from crack tip are cascade remnants, in the form of impurity rich zones.
2. Application of LKMC as a tool for the investigation of the internal microstructure of cascade remnants ("copper-rich zones") is justified and the necessary requirements to an appropriate LKMC code are formulated. During the stay the code developed earlier in RRC KI is adopted for investigation of cascade annealing in bcc system Fe-Cu.

3. Literature review is performed in order to specify the necessary input data for the code and the preliminary testing of the code is performed as applied to investigation of the mode of vacancy driven copper diffusion.

References

1. N. Sekimura, T. Morioka, K. Morishita, J. Nucl. Materials 283-287 (2000) 758.
2. R.A.Johnson, Phys.Rev., Phys.Rev, 134 (1964) A1329.
3. Y.Le Bouar, F.Soisson, Phys.Rev. B, 65 (2002) 094103.
4. P. Auger et al., J. Nucl. Mater. 225 (1995) 225.
5. A. Barbu et al., Nucl.Instr.Meth.Phys.Res. B146 (1998) 278.
6. O. Khrushcheva et al., Nucl.Instr.Meth.Phys.Res B202 (2003) 68.
7. D.J. Bacon et al., J. Nucl. Mater. 323 (2003) 152.
8. A.F.Calder, D.J. Bacon, in: Microstructure Evolution During Irradiation, Sympos. Proc. Vol. 439 (Materials Research Society, Pittsburgh, 1997) p. 521.
9. M.E.J. Newman, G.T. Barkema, *Monte Carlo Methods in Statistical Physics* (Clarendon, Oxford, 1999)
10. N.Metropolis, A.W.Rosenbluth, M.N.Rosenbluth, A.H.Teller and E.Teller, J.Chem.Phys. 21 (1953) 1087.
11. K.Kawasaki, Phys. Rev. 145 (1965) 224.
12. C. Domain and C. S. Becquart, Physical Review B **65** (2001) 024103.
13. L.C.Kimerling, H.M. DeAngelis, J.W.Diebald, Solid State Commun. 16 (1975) 171.

INVESTIGATION OF PHYSICAL MECHANISMS OF COPPER CLUSTERING IN RPV STEELS PROMOTED BY RADIATION PRODUCED COLLISION CASCADES AND FREELY MIGRATING VACANCIES

Stay report by Dr. Vladimir A. Borodin

(RRC Kurchatov Institute, Moscow)

April - July 2005

FZ Rossendorf, 2005

1. Introduction

Modification of macroscopic properties of solids results from kinetic processes involving matter redistribution at the microscopic scale. These processes include migration of individual atoms (both main solid constituents and impurity atoms) and point defects (vacancies, self-interstitials), as well as formation and dissociation of various new phase clusters and defect complexes. This situation is met, in particular, when one deals with the kinetics of reactor pressure vessel (RPV) steels in irradiation conditions. Roughly, these steels can be considered as iron containing several percent of minor constituents (first of all – chromium}, distributed in the bulk either in solid solution or in second-phase inclusions, while neutron irradiation produces point defects that enhance the minor constituent redistribution and can promote both dissolution of already existing phase inclusions and formation of new phases. Not all among various impurities redistribute under irradiation in a way that leads to undesirable consequences in terms of mechanical property stability. However, it has been experimentally found that some impurities, when present at concentrations exceeding certain limits, can drastically deteriorate mechanical stability of steel under irradiation. One of such undesirable impurities is copper, which can alloy the steel at the production stage. Low-chromium steels containing above 0.1-0.2 wt% Cu are known to noticeably increase the temperature of ductile-to-brittle transition (DBTT) under irradiation, which bears potential risk of pressure vessel brittle failure under accident conditions.

Microscopic reasons for copper-induced embrittlement of RPV steels are not clear. At present they often correlate the effect of irradiation on the mechanical property degradation, as manifested in e.g. the shift of DBTT under irradiation, with the redistribution of copper atoms in the iron matrix by primary radiation damage. This conclusion is correlated with the experimental observations that neutron irradiation leads to the formation of so-called “copper-rich zones”, that is – the regions of several nanometers size, where the concentration of the minor alloy constituents is increased with respect to these average concentration in the bulk. Information about such small zones, which cannot be observed in transmission electron microscope (TEM) is provided by very sophisticated methods, such as atomic probe field ion microscopy (APFIM) [1-3]. An indirect information on nanometric cluster formation under neutron irradiation is provided also by small angle neutron spectroscopy (SANS) [4]. These clusters manifest the properties that make them very probable candidates for the increase of the DBTT under irradiation.

Precipitates in general have a trend to hinder or block dislocation motion, and copper clusters are not an exception [5-7], so that CRZ formation should be accompanied with the steel hardening. Irradiation indeed results in the hardening of RPV steels, but it can be due, in addition to CRZs, to other precipitates (quite large carbonitrides, oxides and sulphides) and to the evolution of the dislocation network (work hardening). A special role of CRZs is due to the fact that not every microstructural component can be associated with the experimentally observed change of the fracture mode in the DBT region from ductile to brittle and thus be responsible for the DBTT shift. Since the crack propagation mode is determined, first of all, by dislocation emission from the crack tip, the radiation-induced precipitates should be able to suppress the formation of local plastic zone at the crack tip. The cross-section of this zone is within several micrometers and thus the dislocation emission from the crack tips can be noticeably affected by irradiation only provided the irradiation creates sufficiently high concentrations of very small precipitates within the potential local ductile zone at the crack tip. CRZs are sufficiently small and, according to SANS measurements [4], their size does not change with the irradiation dose, while the concentration grows nearly linearly with the dose, reaching quite high values.

Due to the potential role of small copper-rich clusters, the problem of cluster nucleation under irradiation has been addressed in the literature (e.g. [8-10]). However, the copper clustering models are typically aimed at the description of pure copper cluster

precipitation, which is not the process leading to copper clustering under irradiation. Indeed, the formation of pure copper clusters is observed usually during annealing at temperatures above at least 500°C, where thermal vacancies in iron become mobile. However, the operation temperatures of RPV steels are close to 300°C and at such temperatures noticeable copper mobility can be achieved only provided vacancies are introduced in a non-equilibrium fashion, which is the case for irradiation. However, a simple introduction of isolated vacancies, e.g. by electron irradiation [11], does not change the mechanisms of precipitation as compared to thermal aging and the clusters formed are not CRZs, but nearly pure copper (with up to 70%Cu content) clusters. On the contrary, copper content in CRZs does not exceed several percent; these are rather copper clouds than clusters. Having in mind this CRZ morphology, as well as other features of CRZ accumulation (e.g. linear increase of microcluster number density with irradiation dose [1,4]), it seems reasonable to assume that CRZ are related to a specific feature of neutron irradiation, namely - collision cascades. In favour of such conclusion is the fact that CRZs are typically enriched not only in Cu, but also in other minor alloy components and impurities (Ni, Si, Mn) [12]. These impurities, in contrast to copper, repel each other [13] and avoid clustering during annealing. On the other hand, all these impurities have at 300°C a noticeable binding to vacancies (typical solute-vacancy binding energies ~0.2 eV [13,14]), implying that local component redistribution can be promoted by the dissolution of pronounced vacancy enrichment in the core of a collision cascade.

Collision cascades are created in metal by the fast component of reactor neutron spectrum. Neutrons with energies exceeding 0.1 MeV are able to transfer some to of the lattice atoms (referred to as "primary knock-on atoms" or PKAs) the energy sufficient not only to move these atoms away from their lattice sites, but to put in motion several hundreds atoms in their vicinity (the excited region has typically the size of several nanometers). The ballistic stage of the cascade itself does not lead to impurity redistribution in the cascade region [15,16], but after the cascade cooling down quite a number of vacancies and interstitials remains in the cascade region. Typically, spatial separation of vacancies and interstitials takes place – the latter are located at the cascade periphery, while the former are created closer to the cascade core center. Interstitials in metals are extremely mobile at irradiation relevant temperatures and within nanoseconds leave the cascade region, partially recombining with the vacancies, but mainly diffusing into the surrounding matrix. Since interstitials normally do not interact with substitutional impurities (except, possibly, Mn [13]), they hardly affect impurity redistribution in the cascade core vicinity. The mobility of vacancies is much lower, so at the time scale of interstitial migration they can be considered as immobile. After the interstitials leave the cascade area, a compact region with the enhanced vacancy concentration is left. Currently it is not clear, whether the annealing of the vacancy-reach cascade core can be responsible for the formation of CRZs and, moreover, which microstructural features can be formed as a result of the interaction of locally enriched cascade vacancy population with copper in the cascade region. In particular, the formation of mixed copper-vacancy clusters has been detected after neutron irradiation [1,17].

The main aim of the present work was simulation of the annealing kinetics of vacancy-enriched cascade cores. The characteristic times of such annealing at temperatures of interet for nuclear reactor operation are of the order of seconds and thus require simulation tools that are able to follow the system evolution for comparable time. Among different techniques of system simulation at the atomistic level, kinetic Monte-Carlo is the one able to follow the particle diffusion and clustering at comparable times. For this reason, simulations here were performed using lattice kinetic Monte-Carlo approach. To our knowledge, one paper where LKMC annealing of collision cascade in Fe with Cu impurity is available in the literature [18], but due to the use of very small simulation cell with periodic boundary conditions its predictions are completely useless for analysis of the cascade annealing kinetics

2. Simulation Technique

Matter redistribution in crystalline solids occurs usually as a sequence of individual events - diffusional jumps, which can be generally described as the exchange of lattice positions of two atoms or point defects (in the most common case of vacancy-mediated diffusion one exchanging particle is a vacancy, while another one – a lattice or impurity atom). Individual jumps occur randomly and the probabilities per unit time (frequencies) of an individual jump events, P_i, depend on the nature of exchanging species, the separation between them, and, as a rule, on the chemical composition of their close environment. Typically, a jumping particle has a choice between several jump possibilities and one can never say, which particular event among those having non-zero frequency takes place in a certain time interval. In other words, starting from any fixed initial configuration of diffusing particles in a crystal, a lot of essentially different jump sequences can be imagined and hence it makes little sense to track the evolution of each individual particle. On the other hand, when one is interested in the "macroscopic" description of an ensemble of diffusing particles, e.g. in terms of the statistics of various clusters precipitated by a certain time, which is comparatively weakly sensitive to the detailed kinetic pathways of particle clustering, a good numerical approach is the lattice kinetic Monte-Carlo (LKMC).

In a standard LKMC simulation experiment one considers a small piece of appropriate lattice (here - bcc iron) with a certain initial configuration of impurity atoms and point defects (in our case – copper atoms and vacancies). Provided the algorithm allowing to define the frequencies of point defect jumps for any particular local chemical environment of jumping particles is specified, it is possible to follow the kinetics of the defect/impurity ensemble by consecutively selecting sufficiently small time intervals and allowing the mobile defects to jump into neighbouring lattice sites with probabilities appropriate to the current defect configuration. After such step-by-step annealing one gets a realization of a purely stochastic process of defect movement and interactions. When either the number of particles in the simulation cell, or the number of simulation runs with similar initial conditions are sufficiently big, the simulations provide a reasonable qualitative picture of the "average" trends of the defect ensemble evolution.

Evidently in order to reasonably represent the kinetics of real systems, even restricting to a rough "average" behavior, Monte-Carlo simulation experiment must satisfy certain requirements, which can be roughly separated into two categories, namely – the adequate definition of the probabilities of each diffusion jump at the beginning of each MC step and the adequate particle movement algorithm (the MC step itself). There exist various algorithms for both these aspects of MC simulation, but no matter which algorithms are used, in order to provide a reasonable description of a system with a particular chemical composition, they have to involve some system-dependent parameters, which remain external to the code itself. The use of adequate input parameters is an essential prerequisite for the reliability of simulation predictions.

Current simulations have been performed using a home-made code *CASINO-LKMC*. In this section we describe the main features of the algorithms used by the code and discuss the choice of input parameters for simulation of vacancy annealing and copper-vacancy cluster formation kinetics in iron.

2.1. Description of the code

2.1.1. Monte-Carlo algorithm and related aspects

The overall description of a Monte-Carlo algorithm, as given in any handbook on computer simulation (e.g. [19]), is extremely simple and in its classical version can be reduced to the following sequence of repeating steps:

(i) select an event (in some versions - several events at a time) among all events possible in the system under consideration;

(ii) according to some predefined rule specify a probability that this event occurs, select a random number in the range [0,1) and accept the event if the random number is lower than the event probability (in certain cases this probability can be selected equal to one which guarantees unconditional acceptation of the event).

(iii) update the list of possible events, taking into account the consequences of the last step (if any) and recalculating their individual probabilities (if this is required by a particular algorithm realization).

However, a practical implementation of this straightforward scheme involves so many *know-how* details that different MC codes simulating essentially the same physical process can have nothing in common, except for the random nature of individual event selection, which is the cornerstone of the algorithm itself.

2.1.1.1. *Basic events*

One can usually be quite flexible in defining the basic events for a particular system considered. Staying close to the problem of the annealing and clusterization of defects and impurity atoms in a solid, one can consider all essentially different objects met in the system - isolated defects, impurity atoms, their complexes of particular sizes and configurations – as individual entities and define an event as transformation of one or several objects into some other objects. For example, when two "monovacancy" objects find themselves at a distance below some threshold one, they are converted into a new object "divacancy" with the properties (mobility, thermal stability, capture probability at other objects, etc.) appropriate for this particular object type and having, generally, nothing in common with the properties of the objects (monovacancies) it formally consists of. This approach is usually referred to as "object Monte-Carlo"; its application to the problem of copper clustering in iron under irradiation is pursued e.g. in [20]. On the other hand, one can keep in mind that crystalline solids consist of atoms occupying the sites of a lattice and the jump event probability can be defined for any atom depending on the occupancy and the local chemical environment of the site where the atom is located. The latter approach, called also "lattice Monte Carlo", is implemented in *CASINO-LKMC*. Note that both approaches have their strong and weak points and in practical calculations are rather complimentary than competing. However, it can easily be conceived that completely different nature of elementary events in these approaches implies essential differences in both algorithmic realization and the basic sets of system-specific input parameters, even when dealing with exactly the same physical system.

2.1.1.2. *“Kinetic” pathway tracking*

A source of considerable differences between different MC codes is the implementation of the "probabilistic" step of MC algorithm. One aspect of these differences is related to the selection of the event acceptation criteria, which is dictated by the simulation experiment purposes. In many applications the aim of the simulation is to find as quickly as possible the desired (e.g. the most energetically favorable) final state, no matter how physically reasonable are the intermediate system states during the run. However, in the problem we are interested in the primary interest is not the most energetically favorable final state, which is never realized, but the particular kinetic pathways of the system decomposition. Correspondingly, the event acceptation criteria have to take into account the physics of individual events at each particular intermediate step. The algorithms allowing tracing the physically reasonable kinetic pathways (implemented, in particular in *CASINO-LKMC*) are referred to as "kinetic Monte-Carlo" [19].

2.1.1.3. *Kinetic time tracking*

Another aspect is the "local" or "global" nature of the event acceptation criterion used. In classical MC schemes all the imaginable events are selected at random and the probability

of the event is calculated "on the fly", for this particular event only. This makes the algorithm implementation very straightforward and, very often, exceptionally quick, because the event probability calculation requires normally information only about the objects in the immediate vicinity of the object participating in the event. However, when the dominating number of events has vanishing or very low probability, the efficiency of such algorithm falls down because the majority of selected events are not accepted. An alternative approach, implemented in the current version of *CASINO-LKMC*, requires the knowledge of probabilities of all possible events that can happen at the current MC step. In spite of the necessity to recalculate before each MC step the event probabilities for all objects affected by the previous event, which often makes such recalculation the bottleneck of the algorithm, this knowledge allows to discard from the very beginning all the "empty" events and to trace the total probability rate of ensemble transformation, P, which is defined as a sum of all current event probability rate,

$$P = \sum_i P_i \ .$$

The knowledge of total event probability rate before each jump has an additional advantage, allowing to follow the system kinetics as a function of time and not only as a function of the number of MS steps, as typical for the codes based on local event acceptation criteria. The algorithm for time tracking in our MC code is that referred to as "continuous time" or "residence time" (see e.g. [19]). Its basic assumption is that on the average one among all event happens within the time interval Δt defined by the total event probability rate before a MC step,

$$\Delta t = 1 / P \ . \qquad (1)$$

This time interval is selected as the duration of the subsequent MC step, while the particular event to happen is selected among all possible (that is, having non-zero probability) ones, taking into account the event's relative contribution into the total probability rate P.

2.1.1.4. *Definition of instantaneous jump rates*

According to the general theory of diffusion, the frequency P of a jump event can be expressed in the form of Arrhenius law,

$$P = P_0 \exp(-(E_{sp} - E_{in})/kT), \qquad (2)$$

where P_0 is some constant with the dimension of inverse time, E_{sp} is the energy of the atomic system at the moment, when the exchanging atoms are in a "saddle point" configuration, E_{in} – the energy of the atomic system before the jump and kT has its usual meaning. It should be kept in mind that except for the temperature, which can be treated as an adjustable parameter, the values entering this formula are external to MC program. Moreover, they depend often not only on two atoms that participate in the jump, but on their surroundings as well. Evidently, in the most general form there is little chance to treat each individual jump exactly. Therefore, a number of simplifications are commonly used.

First of all, it is not necessary to treat the energies entering equation (2) as the complete energies of the system. In fact, we can chose a certain pair of exchanging particles as a "reference", assuming that the system with this pair of particles in the equilibrium (initial) configurations has energies E_0 and E_{sp0}, respectively, while the energies of other pair configurations can be measured as deviations from these reference values, $-E_{bi} = E_i - E_{i0}$ and $-E_{bs} = E_s - E_{s0}$. Second, though P_0 depends on the particular pair of jumping particles and sometimes on the chemical composition of the pair environment, it is a common practice to neglect the dependence on both. Having in mind these two remarks, we can reformulate equation (2) as

$$P = P_b \exp((E_{bs} - E_{bi})/kT) \ , \qquad (3)$$

where

$$P_b = P_0 \exp(-E_b /kT) \qquad (4)$$

and $E_b = E_{s0} - E_{i0}$ is the energy barrier for the reference jump.

Since a particular value of P_b affects only the global time scale of MC run, but not the probability ratios of different jumps, the assignment of jump probabilities is normally performed with $P_b = 1$, while the correct value of P_b can be calculated separately and used later on for the conversion of MC time to the real time.

In principle, when binding energies for any particular configuration of exchanging pair can be taken from some database, the jump frequency is immediately obtained. The problem is, however, that normally "configuration" includes not only the exchanging pair, but also atoms surrounding it. In all cases the nearest neighbours of both jumping particles are to be considered, but sometimes also second, third and bigger-order neighbours can contribute to the energy changes associated with the diffusion jumps. In this situation the total number of possible atomic configuration is so large, that it is impossible to measure or calculate the energies for all of them. In reality, one has at hand usually only very limited information, such as the formation energy of an individual diffusing particle in an otherwise perfect lattice and the energy of bonding between two particles of the same kind (a "like" dimer) or of different possible kinds ("unlike" dimmers), provided more than one particle type is present, or the lattice is not monatomic. As for the activation energies for particle diffusion, the input database is normally even worse, for the simple reason that it is much harder to measure or calculate them. Hence, one has to introduce some simplifications in order to more or less physically reasonable interpolate the variety of possibilities, using only a "minimum set" of data, which should be available in any case.

Typically, the parameters required for the calculation of event probabilities for a MC simulation include the energies of exchanging particle pairs in an equilibrium position and in the saddle point of diffusion jump.

Equilibrium energies are calculated in *CASINO-LKMC* in the framework of the “bond model” approximation which is essentially a model of pair-wise interactions between atoms. Such kind of a model assumes that the total energy of the crystal can be presented as a sum of contributions, given by each pair of atoms in the crystal,

$$E = \frac{1}{2}\sum_{i=1}^{N}\sum_{\substack{j=1 \\ j\neq i}}^{N} E_{ij} \qquad (5)$$

where N is the total number of atoms in the crystal. Typically it is assumed that the contribution E_{ij} from a pair of atoms depends only on the chemical nature of contributing atoms and the distance between them. It is also assumed that the interaction decreases with the increase of the distance, so that atoms at distances above some critical one give vanishing contributions. Since lattice Monte-Carlo deals with fixed sets of interatomic distances, it is convenient to specify the distance between interacting atoms in terms of the number of coordination spheres separating the atoms, so that the cutoff distance corresponds to the maximum coordination shell K from one lattice site to the other one, where the interaction is still non-zero. Then the total energy can be rewritten as

$$E = \sum_{X}\sum_{Y}\sum_{k=1}^{N} Z_{XY}^{(k)} E_{XY}^{(k)} \qquad (6)$$

where $Z_{XY}^{(k)}$ and $E_{XY}^{(k)}$ are, respectively, the total number and the interaction energy for pairs of atoms of chemical types X and Y located at distance k, while summation in (6) is over the chemical types and the interatomic separations. Referring to a «ball and stick» representation of crystalline lattice, it is convenient to treat the atomic pairs with non-zero interaction as connected with "sticks" (or 'bonds") and $E_{XY}^{(k)}$ - as energies of bonds connecting atoms X and Y. The bond energies are free input parameters, which should be borrowed from external database (experimental measurements or detailed atomistic calculations).

When the saddle-point energies are not known for different environments of exchanging particles, which is usually the case, an additional approximation for the energy in the saddle point position of the jump is to be postulated. The common practice is to present the saddle point energy in the form

$$E_{sp} = E_m + \max(E_{in}, E_{fi}),$$

where E_{fi} is the energy of the system after the jump and E_m is the migration barrier. Such selection guaranties that the ratio of the transition probabilities for the forward jump and the backward jump satisfies the fundamental relation (called "the principle of detailed balance"):

$$P_b(i \to f) / P_b(f \to i) = \exp(-\frac{E_{bi} - E_{bf}}{kT}) \qquad (7)$$

The energies of equilibrium configurations are calculated in the code according to the bond model, while the migration barrier can be introduced in several ways. In the simplest case, we neglect the dependence of the migrating barrier on the environment of exchanging pair, assuming it equal to that for the jump of the same exchanging particles in a monatomic lattice of the host material. Such approximation is one of the most widely used in MC simulation practice, being the basic assumption of the so-called Metropolis algorithm. However, more complicated situations accounting for the chemical composition of a “lens” of common nearest neighbours of exchanging particles can be dealt with by the code, provided the energetic information for appropriate atomic configurations is available.

2.1.2. Code performance

CASINO-LKMC is a Windows application that provides user-friendly interface for selection of possible lattice types and sizes of model crystal. It allows simulation of simultaneous diffusion and clusterization of up to two different particle types, in addition to vacancies. Means of on-line visualization of atomic system progress and statistical data acquisition are provided.

Because of the necessity to re-calculate the jump probabilities for many atoms surrounding the jumping pair at each MC step, simulations are computationally costly. The necessity of covering several hundreds millions of atomic jumps means the duration of individual run of several days of CPU time at a PC with CPU frequency of 2.5-3 GHz.

2.2. Selection of input parameters

In order to simulate a particular system, a proper set of bond and migration energies must be specified. In the case of copper in iron, treated in the current simulations, there is very little relevant experimental information available, so we relied on the results of quantum-mechanical first principle calculations, published in [21]. These calculations explicitly take into account the magnetic effects on electron distribution in iron with defects and copper atoms, which is essential for the results to be reliable. Moreover, the subsequent calculations of binding energies of small copper and vacancy complexes in bcc iron [22] demonstrate that the bond model is a reasonable approximation for calculation of cluster energies.

The input values used in simulations are summarized in Table 1. All energies are measured with respect to pure iron background (that is, the Fe-Fe bond energy vanishes). These parameters correspond to the dataset of [21] for the biggest simulation cell (128 atoms) with fixed cell boundaries, which are the most appropriate for defect simulation in the material bulk.

Table 1. Input energy parameters for defects in bcc iron used in current calculations (from [21])

Input parameter	Value, eV
Vacancy formation energy	1.28
Vacancy migration energy in the bulk	0.65
Copper atom configuration energy	0.59
Vacancy-copper exchange barrier	0.53
Divacancy binding energy at 1NN separation	0.14
Divacancy binding energy at 2NN separation	0.28
Divacancy binding energy at 3NN separation	-0.02
Cu-V binding energy at 1NN separation	0.17
Cu-V binding energy at 2NN separation	0.19
Cu-V binding energy at 3NN separation	0.04
Cu- Cu binding energy at 1NN separation	0.14
Cu- Cu binding energy at 2NN separation	0.03
Cu- Cu binding energy at 3NN separation	-0.01

During the calculations we assume that Cu atoms and vacancies in the copper-vacancy clusters occupy the sites of the host bcc lattice. Strictly speaking, when pure copper clusters become sufficiently large, they may undergo phase transformation to, first, the so-called 9R phase and then to incoherent fcc Cu precipitates [23], but such transition occurs only for clusters of at least several nanometers size, which are not met in our simulations.

3. Simulation Results

3.1. The effect of freely migration vacancies on copper clustering

3.1.1. Basic assumptions

Modern phenomenological models of Cu clustering during irradiation of RPV steels are based on the idea of homogeneous clustering of Cu monomers, but become mobile under irradiation at elevated temperatures as a result of the increase of point defect (mainly vacancy) concentration (e.g. [8]). Usually they treat copper diffusion in terms of the simplest model, assuming no interaction between vacancy and Cu atom. However, as shown in Table 1, this interaction is sufficiently strong in order to allow a correlated diffusion of vacancy–copper pairs and bigger bound complexes, which makes analytical description of copper clustering cumbersome. In such situation KMC simulation is a convenient tool allowing to get deeper insight into the microscopy of the annealing of Cu solid solution. However, in order to correlate the simulations to the real life, one should realize the physical picture of the simulated process and the approximations involved.

The most important approximation is related to the limited size of the simulation cell. When diffusional annealing of impurity and defect ensembles are made by LKMC, it is usually implied that the concentration of all atomic species are at least higher than the inverse of the number of lattice sites in the simulation cell, N (in our case $1/N \sim 0.5\text{-}5\times10^{-6}$). This condition is valid for Cu, whose relevant concentrations in RPV steels vary in the range of 100-10000 appm. However, it can hardly be true for freely migrating vacancies in RPV steels in reactor operation conditions. Indeed, the concentration of freely migrating vacancies can be roughly estimated from the balance of point defect creation by irradiation and their loss either at point defect sinks, or due to recombination with interstitials. The rate of Frenkel pair production, K, in a thermal nuclear reactor is quite low, typically $K \sim 10^{-9}\text{-}10^{-10}$ dpa/s, while the sink density in ferritic steels is well known to be high (the main sinks are dislocations with

the density at the level of ~ 10^{10}-10^{11} cm^{-2}). The combination of low defect generation rate and high sink density practically excludes the direct recombination as an annealing mechanism for freely migrating defects, and the balance equation for the average steady-state concentration of freely migrating vacancy, C_v, can be written down in a standard rate theory way as

$$K - k_v^2 D_v C_v = 0, \quad (8)$$

where k_v^2 is the total vacancy sink strength. The vacancy diffusion coefficient is given by the equation

$$D_v = D_0 \exp(-E_{mv} / kT). \quad (9)$$

where E_{mv} is the energy of vacancy migration, which, according to different estimates (e.g. [20]), is approximately 0.64-0.68 eV and the prefactor D_0 is typically 1 cm^2/s. Assuming the above mentioned parameter values, we obtain for the irradiation temperature of 300°C an estimate C_v ~ 10^{-13}-10^{-14}. In other words, the average number of freely migrating vacancies in a volume of simulation cell, $\bar{N}_{vc} = C_v N$, is much less than unity. Hence, the simulation of copper redistribution by freely migrating vacancies required a special strategy, which allowed to give a reasonable interpretation of simulation results.

Indeed, if one selects inside the irradiated material a small cube with the size of the simulation cell, there is a very little chance to meet more than one freely migrating vacancy in the volume of this cube. Most of the time the selected volume contains no vacancies at all, and only seldom a single vacancy enters it, performs some redistribution of copper atoms inside and then leaves the cell. Because on the average there is one vacancy per $1/C_v$ lattice sites, the average part of the vacancy lifetime spent in the observation volume is of the order of $1/\bar{N}_{vc}$, provided each site is visited with the same probability. On the other hand, when there is no vacancy inside, nothing happens with the impurity distribution in the observation volume. Evidently, such situation can be reasonably well simulated as the annealing of the appropriate number of initially randomly distributed Cu atoms and exactly one vacancy in a simulation cell with periodic boundary conditions. The use of periodic boundary conditions corresponds to the exclusion of the "dead time" and is equivalent to the renormalization of the total time t of the evolution according to the relation

$$t = N_{vc}^{-1} t_{KMC}, \quad (10)$$

where t_{KMC} is the system evolution time calculated during the KMC run. For a typical simulation cell size of 5×10^5 lattice sites, as used here for simulation of the effect of freely migration vacancies, and with the above-mentioned estimate of the average vacancy concentration in the bulk, the scaling factor is 10^7-10^8. In other words, one second of the system evolution in KMC simulations described in section 3.1 corresponds to 1-10 years of pressure vessel operation history.

3.1.2. The kinetics of Cu redistribution: one vacancy per simulation cell

LKMC runs have been performed for Cu concentrations of 0.05, 0.1 and 0.2 at.%, and involved 250-350 millions Monte-Carlo steps (MCS), or, in terms of system evolution time t_{KMC}, from ~1.8 to ~5.6s (note that the system evolution time is determined in each run by is particular kinetic pathway and there is no one-to-one correlation between the number of MCS and the system evolution time). The simulations demonstrate that the diffusion of freely migrating vacancies in a solid solution of Cu atoms can indeed result in clustering of Cu atoms, but the whole picture of cluster nucleation turns out to be noticeably more complicated than one might expect from the modern rate theory approaches.

Qualitatively, the kinetics of the impurity ensemble can be divided into two or three stages, depending on Cu content, and the duration of each stage is also sensitive to the

concentration of Cu atoms. At the initial stage the jumping vacancy is captured from time to time by Cu monomers or dimers (a certain amount of dimers can be present from the very beginning due to geometrical packing restrictions). Such mixed pairs or trios are extremely mobile and, due to the positive binding between the vacancy and Cu atoms, move around as a bound complex for several interatomic distances. In most cases these complexes eventually lose the vacancy due to either direct vacancy thermal emission, or, in the case of trimers, with the intermediate splitting reaction V-2Cu ->Cu + V-Cu. However, two additional events can happen during the movement of bound copper-vacancy complex. First of all the complex can occasionally encounter with a free Cu monomer or (much more seldom) dimer and pick it up, increasing the cluster size. An alternative process of Cu atom (or even a Cu dimer) loss was also found to happen rather frequently. The mechanism of such Cu "emission" is related to the fact that clusters with several Cu atoms have quite irregular shapes. As a result of vacancy jumps inside the cluster, a Cu atom is sometimes left aside at 2-3 nearest neighbour (NN) separations from the remaining cluster. Such events were observed in bound V-Cu clusters containing up to 12 Cu atoms, however in clusters with more than 7 Cu atoms, these "escapes" are recaptured after several vacancy jumps within the cluster. However, the remaining cluster can also leave the escaped atom behind and move apart, the efficiency of this atom loss process increasing with the decrease of the size of the bound complex.

The lifetimes of bound complexes V-*n*Cu are limited, ultimately, by vacancy emission and vary considerably depending on the particular kinetics of Cu atom capture and loss. Indeed, as a result of the competition between the Cu pick-up and loss, the number of Cu atoms in a bound complex fluctuates and typically a cluster emits a vacancy when n falls below 5. Correspondingly, bound complexes with $n > 5$ were nearly always observed to lose several Cu monomers before the thermal emission of the vacancy and after the emission the remaining cluster (or, more exactly, a correlated configuration) of several Cu atoms only seldom has the maximum amount of Cu atoms gained by the moving bound complex.

Although the lifetimes of the vacancy in individual bound complexes vary noticeably, the general trend is the increase of the vacancy lifetime in a bound complex with the increase of the maximum size that it manages to reach. Therefore, after some time from the start of the annealing the mode of vacancy diffusion changes. While at the initial stage the vacancy does not differentiate between different Cu atoms and the vacancy-stimulated diffusion shifts all Cu atoms at approximately the same rate, after the fluctuative formation of compact clusters the vacancy spends more and more time in bigger bound complexes, first of all because of the increase of the bound complex lifetimes and, second, because bigger clusters have bigger vacancy capture cross-section. As far as mobile clusters contain 5-7 Cu atoms, the time of vacancy dwelling in the cluster is at least an order of magnitude longer than that between the emission and re-capture. Superficially it looks out like consecutive vacancy jumps from one bigger cluster to another (or even back to the same one), with minor perturbations of the spatial positions of all other Cu atoms during the short transition periods. One should have in mind, however, that the time between emission and re-capture is largely determined by the number density of the bigger clusters, which in our KMC simulations is necessarily quite high (even one cluster per cell means number density of $0.5\text{-}5\times10^{-6}$, depending on the simulation cell size).

At this second stage of Cu solid solution annealing the dominant process is the gradual increase of the size of the biggest clusters, which occur mainly due to capture of immobile Cu monomers by moving V-*n*Cu complexes. Indeed, clusters containing n~4-7 Cu atoms are still quite mobile and keep vacancy for the time sufficiently long to pick up and lose several Cu atoms. Although these captures and losses of Cu atoms occur randomly and the cluster size after vacancy emission can easily become even smaller than it was at the moment of vacancy capture, gradually the biggest cluster size increases from 4 to some threshold size, which promotes the onset of the next stage of the annealing.

The third stage of annealing can be described in short as the annealing "saturation". This saturation results from a combination of several factors. First of all, our simulations show that V–*n*Cu complexes containing already *n*~7-8 Cu atoms can keep the vacancy for times comparable to the simulation time (at least several seconds). This does not mean that such clusters never emit vacancies, but, as mentioned above, the thermal vacancy dissociation is usually preceded by the loss of several Cu atoms. On the other hand, for complexes with *n*> 8 we observe a clear trend that the chance of Cu atom escape from the cluster decreases with the increasing complex size. As a result, the first V-*n*Cu complex that manages to capture *n*~8-9 Cu atoms has a big chance to ultimately trap the vacancy and still increase its size, while all the remaining Cu atoms and clusters remain frozen in, except for those that are occasionally picked up by the V-Cu complex. On the other hand, with the increase of the cluster size beyond V-7Cu the cluster diffusion mobility visibly falls down as compared to dimers or trimers, not to mention mono-vacancies. The restricted cluster mobility diminishes the prospects for its subsequent growth.

As evidenced by our simulations in the Cu content range of 0.05-0.2at%, both the conditions for the formation of "vacancy traps" and the state of the remaining Cu solid solution (that is the number densities of pure Cu dimers, trimers, etc.) are sensitive to Cu content in the bulk. Indeed, the probability of cluster size increase seems to be proportional to the copper concentration, while the cluster decomposition probability is sensitive rather to the cluster size, but not so much to overall Cu content. Correspondingly, at 0.05 at% Cu one observes a definite dominance of the cluster decomposition trend. The main Cu clusters at this concentration were dimers, whose concentration noticeably fluctuated in time, but never exceeded 4-5 % of the total Cu content. Bigger pure copper clusters (trimers) also appear, but seldom and do not live long. The vacancy spends the majority of time in small V-*n*Cu complexes, the typical scenario being the capture of the vacancy by a dimer or trimer and a relatively quick pick-up of 2-3 Cu atoms as long as the cluster mobility remained high.. However, already 4-5 Cu atoms per cluster seems to drop the cluster mobility below a certain threshold and the time needed to capture more monomers becomes less then the time for cluster decomposition. Correspondingly, the fluctuative formation of clusters with 6-7 Cu atoms, even though sometimes observed, does not lead to the formation of a vacancy trap. Finally such cluster looses several Cu monomers and after vacancy emission a cluster of at best 3-4 Cu atom is left, which is typically decomposed into Cu monomers at subsequent vacancy capture.

Naturally, although within the maximum time reached in simulations (~2 s) no vacancy trap formation was observed, we cannot exclude that for this particular Cu content size a vacancy trap can be formed at the longer time scale, because the maximum complex size observed in simulations (V-8Cu) was quite close to the threshold. However, it seems that at the overall Cu contents below 0.05at% the diffusion of freely migrating vacancies does not lead to copper clustering and has little practical influence on the material strength.

At Cu contents above 0.05at%, the appearance of several Cu clusters containing 5-6 Cu atoms was found to be a prerequisite for the formation of the " vacancy trap", while the threshold size corresponded to n = 8-9. At 0.1at% Cu this threshold had been reached many times, involving different Cu clusters, and although no supercritical complex was formed prior to the termination of the run, one can be nearly sure that on the longer time scale it will form. On the contrary, in 0.2at.% Cu alloy already the second attempt to overcome the threshold of V-8Cu (starting from V-6Cu) was successful. Correspondingly, both the time for the final vacancy trapping and the final cluster size distribution were noticeably different for different Cu contents.

Summing up, in the considered case the early kinetics of Cu clustering by vacancies involves cluster growth promoted first of all by the movement of V-Cu bound complexes, which trap and detrap single immobile Cu monomers The combination of the increase of the

complex stability to vacancy emission and the decrease of complex mobility with the complex size results ultimately in vacancy trapping in a cluster of intermediate size (n ~10-15), which grows progressively slower with each next captured Cu monomer. In other words, a vacancy demonstrates a kind of "self-trapping": first it creates one or several small copper clusters and finally becomes captured in one of these. The lower bound for the copper content in the bulk required for the formation of vacancy trap lies, according to our simulations, close to 0.1 at% Cu. It is worth noting just this value is usually cited as the experimentally observed lowest content of Cu, after which pronounced radiation embrittlement is observed in RPV steels.

3.1.3. Kinetics of Cu redistribution: several vacancies per simulation cell

In the discussion above we assumed that the vacancy concentration is very low and so one can neglect the presence of other vacancies. Even though on the average the concentration of freely migrating vacancies in RPV steel is indeed very low, the "self-trapping" effect hinders vacancy annealing at other extended sinks (dislocations and grain boundaries) and thus after some irradiation dose a certain amount of vacancies is captured in traps. Due to the limited size of the simulation cell, it is not easy to estimate, how big can become the number density of such vacancy traps with the increasing irradiation dose. On the other hand, at Cu concentration ≥ 0.1at.% the formation of one trap per simulation cell (which corresponds to the number density as high as $10^{17}/cm^3$) required less than one second. Even using the time scaling factor of 10^7, as estimated in sect. 2.1, the time to reach such high number density of traps (and trapped vacancies) in reactor irradiation conditions will be less then a year, that is - much less than the pressure vessel operation time. Hence, is of interest to speculate what happens if the number of vacancies per cell becomes more than one.

For this purpose, the results of another simulation are instructive. In this run five vacancies had been put in a simulation cell of appr. $5x10^5$ sites which contained 0.1at.% of Cu and the whole array was annealed up to 0.56 s. At the initial stage the effects of each vacancy were practically additive, the vacancies were pairing with free Cu monomers, gradually creating dimers and trimers. However, already after 2.4 ms four of five vacancies were collected in one cluster (4V-4Cu) and did not leave it till the end of the run. The cluster was only moving around and steadily collected Cu atoms. The remaining vacancy was recaptured several times in complexes V–nCu, which were located sufficiently far from the multivacancy cluster. One such complex existed for relatively long time (~0.26 s) and managed to reach n = 7, but finally lost several Cu atoms and emitted the vacancy, leaving behind a copper trimer. The biggest cluster by that time reached the size of 4V-9Cu, while the pure Cu clusters were at best dimers and trimers. Correspondingly, after less then 0.01 s the remaining vacancy was captured by the bigger complex. The resulting complex 5V-9Cu retained certain mobility, but it was so low that no more Cu atoms were captured till the end of the run (that is, during ~0.3 s). On the other hand, the mixed V-Cu complex did not emit a sole vacancy and did not lose any Cu atom, which indicated quite high stability of such mixed complexes. It is interesting that although the positions of Cu atoms were changing all the time, the cluster remained compact and no trends to segregation of vacancies or Cu atoms inside the cluster were observed; it remained more or less a uniform mixture of copper atoms and vacancies. It is interesting to mention, that by the end of the simulation run the pure Cu clusters were only dimers and trimers, which contained ~15% of all copper content. However, no pronounced clustering of Cu atoms is observed regardless of relatively high Cu concentration.

It should be realized that the picture of multi-vacancy cluster formation discussed in this example implies rather high vacancy concentrations prior to the annealing, which are not relevant for the irradiation of RPV steels. However, the demonstrated trend of high stability of multivacancy complexes allows us to assume that stable bound V-nCu complexes become

traps for additional vacancies created by irradiation and can finally convert into complexes *m*V-*n*Cu, with *m* exceeding unity. It is not clear at the moment, however, how many vacancies can be captured in a cluster with a certain number *n* of Cu atoms and whether it can be converted into a stable void nucleus.

3.1.4. Summary

As can be concluded from the obtained results, pure Cu clusters created by freely migrating vacancies at 300°C in the Fe-Cu alloys in the 0.05-0.2 at.% Cu range are mainly dimers and trimers, the number density of which is established as a result of dynamic equilibrium of small cluster creation and breaking by migrating vacancies. However, the binding between the vacancies and Cu atoms results in the fact that the majority of time the freely migrating vacancy spends in small clusters V-*n*Cu, which are sufficiently mobile (up to copper content of at least $n \sim 10$) in order to collect immobile Cu monomers in the complex vicinity. Although the copper capture is counteracted by the loss of Cu monomers and dimers during the motion of the bound complex, at Cu concentrations at and above ~ 0.1 at% such V-*n*Cu clusters are able to fluctuatively accumulate a certain threshold number of Cu atom, which stabilizes the bound complex, transforming it into a stable vacancy trap. Such stabilized V-*n*Cu are expected to serve as traps for further vacancies.

Based only on the LKMC simulations, it is impossible to estimate, how big can become the number density of stable copper-vacancy clusters. It can only be concluded that it can hardly exceed ~ 10^{-6}, since one such cluster per simulation cell puts the monovacancies in the simulation cell completely out of the game. On the other hand, one can be sure that the number density of stable V-Cu clusters, even in alloys with super-threshold Cu content will saturate after sufficiently big irradiation dose, simply because the creation of stable clusters depletes the matrix with copper. Another reason is that sufficiently high concentration of stable clusters reduces the concentration of freely migrating vacancies in the matrix.

A practical conclusion from this picture is that it makes little sense to model the Cu cluster nucleation at temperatures relevant to nuclear applications in terms of standard nucleation theories assuming mobile monomers and immobile clusters. In fact, the picture predicted by KMC simulation is in better agreement with the experimental observations of very diluted Cu enriched zones, rather than perfect Cu clusters.

3.2 The effect of collision cascades on copper clustering

3.2.1. Cascade parameters

In contrast to freely migrating vacancies, whose concentration in irradiated RPV steel is low, high vacancy concentrations can be achieved locally in the cores of collision cascades initiated by fast neutrons, which are always present in the spectrum of thermal reactors. As discussed in the introduction, the most interesting from the point of view of possible copper clustering is the stage of annealing of the vacancy-enriched cascade cores that are left after the cascade cooling down and quick interstitial escape from the cascade. In order to perform KMC simulation of this annealing we need some information concerning the distribution of copper atoms and vacancies in the cascade region.

As discussed in the introduction, neither the ballistic stage of the cascade, nor the stage of quick interstitial escape introduce noticeable redistribution of Cu atoms in the cascade region, so that the initial distribution of copper atoms for a KMC run can be selected uniform and completely random within the simulation cell. In order to specify the parameters of vacancy enriched zones, we have relied on the literature data for the molecular dynamics simulations of collision cascades in iron.

Multiple simulations of this kind show that the volume occupied by a cascade, its shape and the number of vacancies in it are correlated and depend on the energy of PKA that initiates the cascade. Typical energy range for cascade-forming PKAs in iron is from 1 to 40 keV: at lower energies no cascades are created, while at higher energies cascades split into subcascades. According to molecular dynamics simulation the number of Frenkel pairs survived after cascade cooling down varies from ~10 at PKA energy of 3 keV to ~ 70 at 30 keV [24,25]. These estimates include only Frenkel pairs with sufficient separation that excludes spontaneous interstitial-vacancy recombination, so we assume that the number of vacancies left after the interstitial escape from the cascade region is not much different from the number of survived Frenkel pairs.

Somewhat less definite is the spatial distribution of vacancies in a cascade. According to [24], cascades in Fe can be described as confined in elliptical regions with different ratios of the long axis length, α, to the short axis length γ. The ratios α/γ vary broadly, and the most probable values depend on the approximations used in cascade simulations. Judging from the α/γ distribution histograms presented in [24], the range α/γ ~ 1-3 is valid for the majority of cascades. The absolute majority of vacancies in cascades are monovacancies, with only several divacancies at higher PKA energies [25].

Having in mind the molecular dynamics results, the majority of calculations has been performed for the cascade parameters, appropriate for cascades created by 20keV PKA. The numbers of vacancies in the cascades were approximately 40 and these vacancies were distributed randomly within elliptical regions ("initial cascade volumes") of ~400-500 a^3 (where a is the iron lattice parameter) with the axis ratios in the range of 1-3. The cascades were placed in the middle of the simulation cell, in order to maximize the distance from the cascade to the simulation cell boundaries.

In contrast to the case of freely migrating vacancies, the vacancies leaving the simulation cells were removed from further consideration, which corresponded to the absorbing boundary conditions. In order to better describe the evolution of copper solid solution in the vicinity of the cascade, a simulation cell of ~4.2 millions lattice sites was used (corresponding to cell edge length of 128a). The lengths of individual runs were limited either by the lifetime of a cascade (defined as the time, when the last vacancy left the simulation cell), or by a predetermined number of MC steps reached.

3.2.2. Cascade annealing in pure Fe

Prior to the investigation of the cascade annealing, we considered what happens with vacancies in pure iron. First of all, vacancies were distributed randomly in the volume of the simulation cell. After the onset of the simulation run, all vacancies left the cell in less than 0.2 ms, showing no trend for clustering. In other words, all clustering observed in the cascades is a consequence of highly correlated initial vacancy distribution.

After that, several correlated vacancy distributions were considered, with the same initial amount of vacancies, but differing either in the average diameter of the initial cascade region (from 5a to 15a) or in the degree of ellipticity (from α/γ = 1 to α/γ =3). In all considered cases qualitatively the same pattern of vacancy kinetics is observed. The initial local vacancy concentration in the cascade region is very high and on the microsecond time scale several small vacancy clusters are formed by vacancy coalescence, while the remaining vacancies escape from the cascade region into the surrounding matrix. The mobility of small clusters remains high and their subsequent evolution is determined by the competition of two processes: cluster coalescence and thermal diffusion. Due to coalescence, vacancy clusters containing more than 10 vacancies can sometimes be formed, but finally even the biggest clusters dissolve and no vacancies are left in the simulation cell.

The cascade lifetimes varied mostly within 0.01-0.1 s, the main factor determining the lifetime being the size of the biggest cluster formed during the coalescence of vacancies and

smaller clusters. The clusters with the sizes less than 5-6 vacancies dissociate within a millisecond, but with the increase of the cluster size its stability against thermal decomposition increases and when the biggest cluster size exceeded 10 vacancies, the dissolution of this cluster was the cascade lifetime limiting factor. Thus, in several simulation runs voids containing up to ~¾ of the initial number of vacancies managed to form. The dissolution of these voids required ~ 1s (see e.g. Fig. 1), which can be considered as the upper threshold for the cascade lifetime in pure iron.

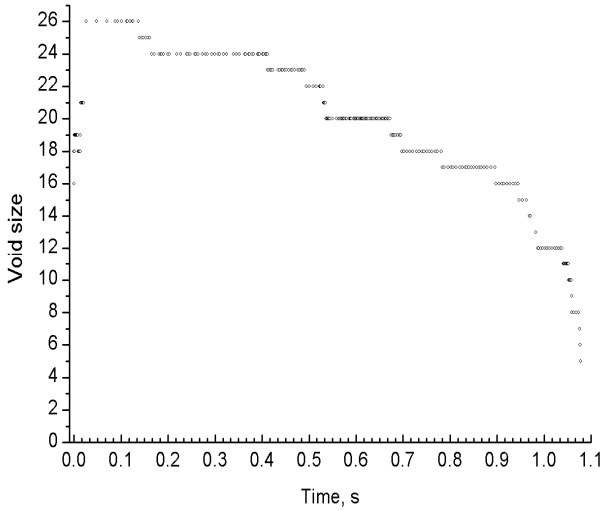

Fig. 1. The kinetics of creation and annealing of a big vacancy cluster in one of the cascade annealing simulation runs.

The cascade lifetime has a trend to decrease with the increase of the initial cluster volume. The increase of the aspect ratio at the fixed initial cluster volume tends to increase the cascade lifetime, seemingly as a result of more efficient coalescence of vacancies into a chain of small clusters, e.g. Fig. 2. However, due to the small number of vacancies per cascade and thus highly fluctuative nature of vacancy and cluster coalescence, no one-to-one correlation between the initial cascade volume or shape and cascade lifetime has been found.

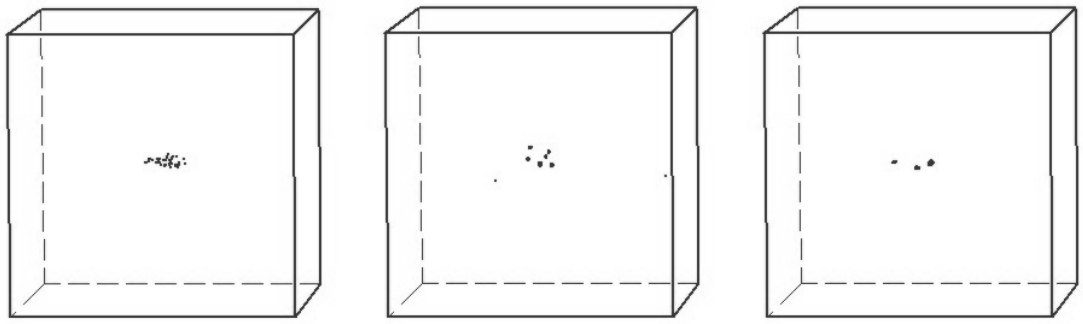

(a) (b) (c)

Fig. 2. The kinetics of annealing at 300°C for a cascade with the initial aspect ratio α/γ =3. (a) initial configuration; (b) after 3×10^{-5} s of annealing; (c) after 10^{-3} s.

3.2.3. Cascade annealing in Fe-Cu alloys

3.2.3.1. *The effect of Cu content*

Several Cu concentrations were studied, starting from quite low concentration of 0.01at.% Cu, which is known to produce no effect on the mechanical behaviour of irradiated RPV steels, up to 1at% Cu. The increase of copper concentration in this range has very pronounced effect on the cascade annealing kinetics.

At the lowest considered concentration of 0.01at% Cu practically no effect of dissolved Cu from cascade annealing was observed. The cluster annealing kinetics is very similar to that observed in pure iron. Namely, very quick formation of several small vacancy clusters takes place, but these contain normally no Cu atoms and dissolve within practically the same time as the cascades of identical initial shape in pure iron. The only difference is the formation of mobile V-Cu pairs during the vacancy transport from the cascade region to the simulation cell surface, so that by the end of simulation runs the majority of Cu atoms is shifted from their initial positions, but the spatial distribution of copper atoms remains random and no Cu clustering is observed.

At 0.05 at.% Cu the annealing of cascades demonstrates bigger variability. In some runs one observes cluster annealing occurring in a very similar way to that typical for 0.01at.% Cu, where cascade quickly separates into several small clusters, which move around and dissolve rather quickly, normally within 0.1 s. However, in some runs these small voids coalesced, making cluster of more than 20 particles (containing predominantly vacancies with several Cu atoms). Such clusters remained stable for much longer times. These nanosize voids practically did not move and the main diffusion events observed in simulations were associated with Cu atom diffusion over the void surface. These events are quick and thus even a big number of MC jumps (several tens of millions) used in simulation did not always allow to completely dissolve nanovoids. However, having in mind that these clusters contain predominantly vacancies, it can be expected that they will finally anneal within 1-2 seconds. From the point of view of copper distribution, no big changes occur during the cascade lifetime, only several copper dimers are formed in the whole simulation cell.

With the increase of Cu concentration to 0.1 at% the latter annealing pattern, that is – the quick separation of initial vacancy cloud into small clusters that finally combine into nanovoids (including more that a half of initial vacancies and 1-2 Cu atoms collected during nanovoid migration) starts to dominate. It is interesting that such nanovoids are already sufficiently big to be detected by e.g. small angle neutron scattering. The variation in non-magnetic SANS curve can indeed be noticed in Fig. 3, but the picture is very much obscured by the signal from chaotically distributed Cu atoms.

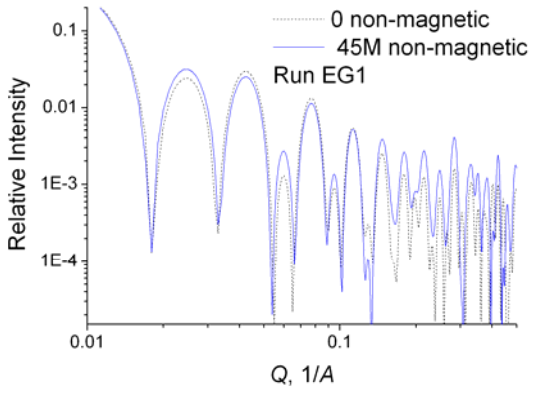

Fig. 3. Calculated SANS signals from the simulation cell with 0,1 at.% Cu before and after cascade annealing for ~0.045 s. The final configuration contains a nanovoid consisting of 26 vacancies and 2 Cu atoms.

In simulation cells with copper concentration to 0.2 at.% the majority of vacancies remains within the simulation cell for the whole simulation run. The biggest part is collected in small vacancy clusters in the central part of the cascade. These clusters move around and sometimes coalesce into 1-2 somewhat nanovoids (> 10 particles), but mostly the number of defects in the cluster remains less than ten, including both vacancies and copper atoms. In contrast to lower copper concentrations, where such clusters were nearly pure voids, the amount of vacant and Cu sites in these clusters are comparable (see Fig. 4).

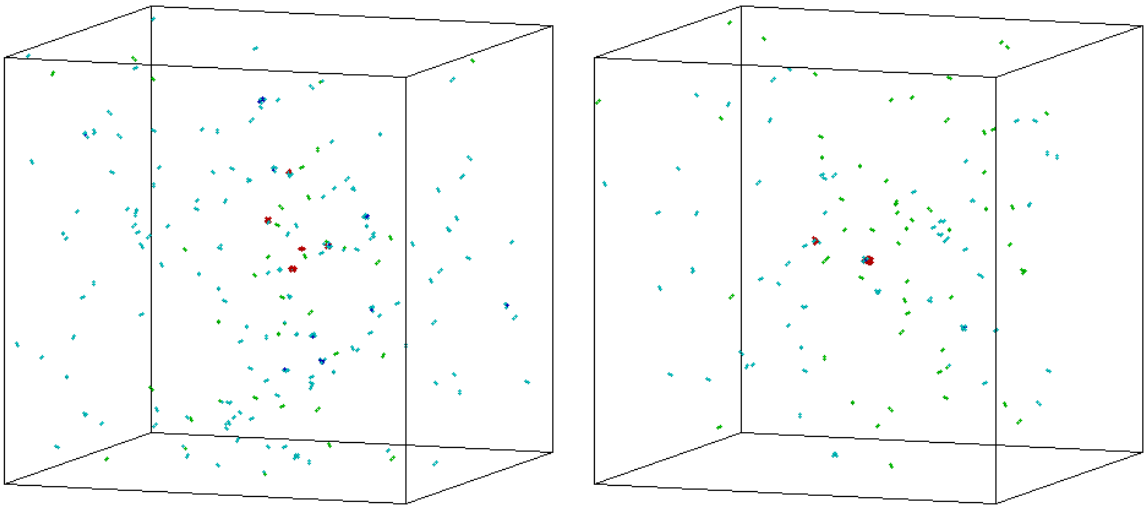

(a) (b)

Fig. 4. Typical spatial distributions of Cu-V clusters after cascade annealing in iron with 0.2 at% Cu. Two different runs are shown. Annealing times are (a) 15 ms and (b) 22 ms. Vacancies are colored in red, Cu atoms – according to the number of nearest neighbours (Cu dimers are green, while with the increase of the particle neighbours the color becomes progressively darker blue). Copper monomers are not shown for clarity.

On the other hand, the vacancies that escape from the central cascade part are very efficiently captured by copper atoms and form small Cu-V clusters that move around collecting copper monomers. The direct visualization of annealing kinetics indicates a fast diffusional movement of these small clusters, resembling very much “bees in a hive”. As a result, in addition to relatively vacancy-rich central clusters, there appears a number of either pure Cu or Cu-rich clusters (up to 6 particles/cluster) outside the cascade region. This “peripheral” activity of monomer vacancies takes time of the order of milliseconds before they either leave the simulation cell, or, rarely, are captured by vacancy-rich clusters.

The subsequent annealing kinetics is governed by the motion of vacancy rich clusters and thermal emission of vacancies from them. As a rule, emitted vacancies are not re-captured by the clusters, but leave the simulation cell. However, during vacancy diffusion to cell boundaries, at least several captures of the vacancy by Cu atoms happens, which contributes to creation of Cu dimers and trimers. In exceptional cases these clusters manage to capture 5-6 Cu atoms, which results, as discussed above, in a cluster relatively stable against vacancy thermal emission. The amount of copper in monomers decreased by up to 2% towards the end of simulation runs, which lasted for relatively short real times (tens of milliseconds) insufficient for complete cluster annealing. Though such decrease does not sound as a big one, after several tens of cascades one can expect quite considerable reduction of copper monomer number.

The trend of clustering efficiency increase with the increase of initial copper concentration becomes more pronounced as copper concentration reaches 0.4 at.%. In this case more than ¾ of initial vacancies remained in the simulation cell even in extremely long runs (several hundreds millions of MCS), which corresponded to times of hundreds of ms. The initial vacancy clouds initially separates into several (from 3 to 7) small clusters, which are quite mobile and sometimes coalesce, but no coalescence into one big nanovoid was observed. Instead, cluster size increases at the expense of copper capturing, which is promoted by rather high content of Cu in the simulation cell. Correspondingly, the V/Cu ratio in vacancy-rich clusters decreases with annealing time.

On the other hand, due to the high concentration of Cu atoms, the capture of individual vacancies is relatively easy. Hence the “peripheral” vacancies escaping from the initial cascade core promote formation of nearly pure Cu clusters. However, the time of complete annealing of monomer vacancies falls within several milliseconds, see Fig. 5, and so no much change in the number of pure Cu dimers and trimers is observed. Nonetheless, several clusters with 4-5 Cu atoms could be formed. Clustered Cu atoms are located in a denser ensemble than at smaller Cu contents in the matrix, see Fig. 6. Note, however, that although clusters are distributed in a correlated manner, they are not centered at the initial cascade center of mass.

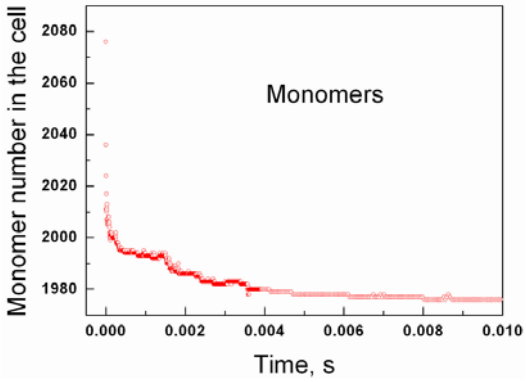

Fig. 5. An example of monomer annealing kinetics in a cell with ~ 0.5 million lattice sites and Cu content of 0.4 at.%. After ~ 4 ms approximately 10% of Cu atoms and all vacancies are clustered.

A new feature arising in simulations at 0.4 at.% Cu is that vacancies emitted from time-to time by vacancy-rich clusters mostly do not leave the simulation cell, but promote formation of new mobile V-Cu clusters as the annealing proceeds. This is not typical for lower Cu concentrations.

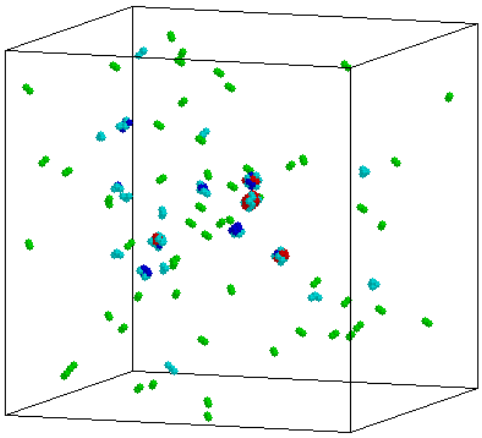

Fig. 6. An example of spatial distribution of Cu-V clusters after cascade annealing in iron with 0.4 at% Cu. Annealing time ~ 0.2 s. Atom coloring is the same as in Fig. 4. Note, however, that linear sizes of simulation cell in all directions are only half of those in Fig. 4.

SANS signal (nonmagnetic) of the annealed simulation cell is shown in Fig. 7. Note that the initial curve is valid both before and after cascade introduction in the cell, because the added vacancies give nearly no contribution to the signal from the background Cu. However, clustering removes quite noticeable amount of Cu from solid solution and lets it be spread in a correlated manner. Hence, one can see a characteristic increase of the signal in the range of 1-3 nm^{-1}.

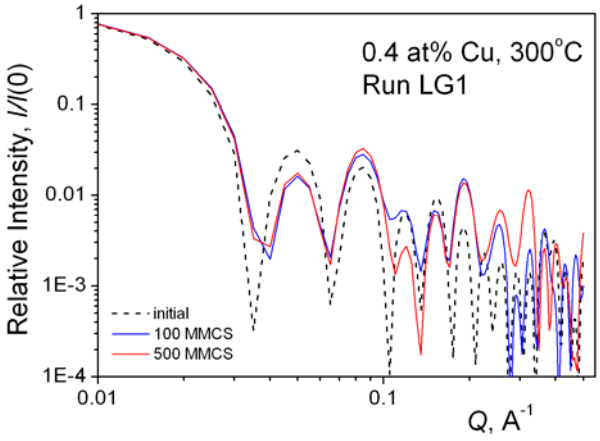

Fig. 7. Calculated SANS signals from the simulation cell with 0.4 at.% Cu before and after cascade annealing for ~0.2 s (at 500 MMCS).

Finally, as the concentration of Cu in the matrix increases to 1 at%, the initial vacancy cloud splits within microseconds into small Cu-V clusters with comparable amounts of Cu atoms and vacancies per cluster. The number of Cu dimers and trimers varies little as compared to the initial configuration, where these are present due to purely geometrical reasons. On the other hand, all vacancies created in the cascade remain (at least within simulation times) inside the simulation cell, leading to the creation of two types of V-Cu clusters: a small amount (1-3 per cell of 0.5 million lattice sites) of clusters formed at the

onset of cascade annealing (with vacancies contribution of ~30-40% of the particles in a cluster) and somewhat bigger amount (~10 per simulation cell) of clusters of 8-10 particles, containing 1-3 vacancies. The latter clusters are formed by consecutive accumulation of Cu monomers, and at such sizes, as discussed in sect. 3.1, are sufficiently stable to dwell for times longer that the typical simulation times and moving too slowly to capture additional Cu atoms. Correspondingly, the cluster structure stabilizes rather quickly (within a millisecond) and consists of a noticeable amount of relatively small clusters distributed over the region with transversal size of ~15 nm, Fig. 8.

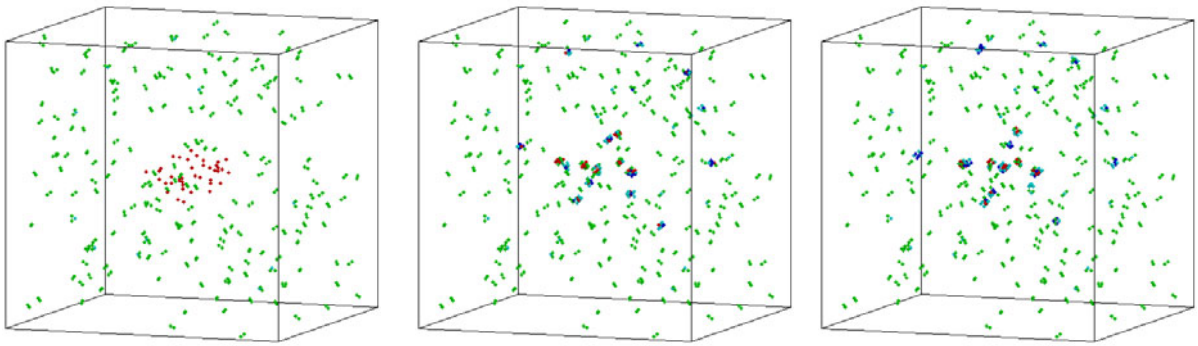

(a) (b) (c)

Fig. 8. A sequence of spatial distributions of Cu-V clusters during cascade annealing in iron with 1 at% Cu. Simulation cell contains ~ 0.5 million lattice sites. (a) Initial, (b) after 10 MMCS (~2.5 ms), (c) after 35 MMCS (~10 ms). Atom coloring is the same as in Fig. 4, copper monomers are not shown.

Summing up, the concentration of copper in iron is an important factor in the effect of cascades on the microstructural transformation. At concentration below 0.1 at% Cu the cascades anneal out practically like in pure iron, with a formation of a small vacancy voids (or 2-3 voids) in the central region of the cascade, which dissolve within 0.01-1 s. At higher Cu concentrations instead of nanovoids small Cu-V clusters with vacancy amount varying from 1-3 per cluster to ~50 % per cluster form, the relative contribution of the latter decreasing with the increase of copper concentration. It is interesting that the cascade remnants include in this case many relatively small clusters distributed over the region with the size approximately an order of magnitude bigger than the size of the initial vacancy-rich zone left after the ballistic stage of the cascade.

3.3.2. *The effect of irradiation temperature*

A limited check of the effect of temperature variation on clustering during cascade annealing was performed at Cu concentrations exceeding 0.1at% Cu. From general considerations, the decrease of temperature makes the binding between particles relatively more efficient, but slows down the kinetics due to the suppression of vacancy mobility. On the contrary, temperature increase should suppress clustering both because it weakens the particle binding efficiency and accelerate the vacancies. It was found, however, that the temperature decrease by 50ºC has little effect on either the qualitative clustering kinetics, or the typical times of cascade annealing. On the contrary, noticeable increase of temperature allows even for high Cu contents to reach complete removal of vacancies from the cascade region within the typical simulation run times.

For example, at 700ºC a cascade in an alloy with 1 at% Cu was annealed completely within 0.1 ms. However, the correlated movements of temporary Cu-V clusters resulted in an intermediate formation of rather big cluster (20V-10Cu after 1.5 μ), which later on dissolved by vacancy emission and, in parallel, moved around collecting copper atoms. As a result, by

the moment of the last vacancy emission the resulting cluster was rather big (14 Cu atoms). In other words, even regardless of strongly accelerated kinetics, the cascades at high temperatures are able to produce nuclei of pure copper clusters, which are able later on to grow (e.g. by absorption of mobile V-Cu dimers and trimers).

3.3.3 *Cascade interaction with self-stabilized vacancy traps*

In the previous sections dealing with the cascade annealing we neglected completely the presence of freely migrating vacancies. Indeed, the cascade lifetime is limited by at most seconds and there is little chance that a freely migrating vacancy appears within this time in a volume of the size of simulation cell around the cascade. Moreover, even if it does, it plays little role compared to several tens of vacancies created in a cascade. However, at Cu contents exceeding 0.1 at.% the freely migrating vacancies modify the state of Cu solid solution, somewhat increasing the number of Cu dimers and trimers. At high irradiation doses the formation of relatively high concentrations of vacancy traps also cannot be excluded. It was interesting to see what happens when a cascade is generated in a material transformed by the freely migrating vacancies.

For this purpose a cascade of 50 vacancies was superimposed onto the final configuration of one of the runs, where the effect of freely migrating vacancies had been studied. This configuration corresponded to 0.1 at.% Cu and contained, in addition to one V-5Cu complex located approximately in-between the cascade region and the cell periphery, more than 10% of Cu atoms in the form of dimers and trimers.

However, nothing very different from the usual cascade annealing pattern has been observed. Several small vacancy clusters were formed and then coalesced in the central region of the cell. The initial V-5Cu complex also behaved in a usual way, dissolving completely within 4 ms. Only two individual features of the annealing are worth mentioning. First of all, the resulting central void captured nearly 80% of all vacancies in the cascade, as well as 2 Cu atoms. The resulting cluster had diameter of appr. 1 nm. Such a void is still too small to be observed in TEM, but is sufficiently big in order to be detected by more sensitive experimental techniques, such as small angle neutron scattering, see Fig. 9. LKMC annealing of such a big void requires a lot of CPU time even in the absence of copper surface diffusion, so the run was stopped very soon after the formation of the void (at 0.17 s).

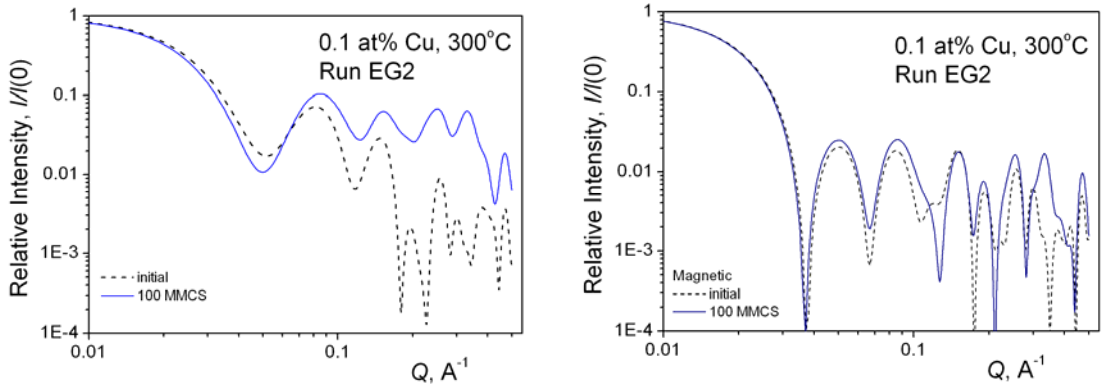

(a) (b)

Fig. 9. Calculated SANS signal from the vacancies and Cu atoms in simulation cell, assuming non-magnetic (a) and magnetic (b) neutron scattering lengths for iron and copper. Dashed line corresponds to the original Cu distribution and solid one – to the end of the run (at 10^8 MCS).

Second, a copper trimer that occasionally turned out to lay close to the initial cascade region, captured four vacancies and the resulting cluster demonstrated both high mobility and resistance to vacancy emission. By the end of the run the composition of this cluster was 3V-

7Cu. Having in mind that complexes V-*n*Cu with Cu content below 6 are very unstable, one can conclude that the addition of vacancies to a small vacancy-copper complex favors the increase of the complex lifetime.

Conclusions

As can be concluded from the current simulations, the clustering in neutron irradiated copper alloyed iron involves at least two non-trivial mechanisms. The first mechanism is related to collision cascades created by fast neutrons. First of all, at copper contents exceeding 0.1 at. % a collision cascade is able to create a region with several small Cu-V clusters spread over a region of 10-20 nm in diameter. The vacancies captured in small clusters survive for times at least as big as 0.1 s at 300ºC (which was the typical time of calculation runs). On the other hand, at low copper concentrations the cascade annealing frequently results in the formation of localized clusters (nanovoids), containing noticeable part (up to 70%) of the vacancies left after the ballistic cascade stage.

The second mechanism is related to the action of freely migrating vacancies on copper clustering. It is demonstrated that interaction of freely migrating vacancies with Cu atoms leads to the formation of highly mobile small V-Cu clusters. At Cu concentrations at and above ~ 0.1 at% such mobile V-*n*Cu clusters are able to fluctuatively accumulate a certain threshold number of Cu atoms, which stabilizes the bound complex, transforming it into a stable vacancy trap.

From the point of view of radiation embrittlement, both nanonvoids and zones with correlated Cu-V nanocluster distribution can serve as barriers for dislocation glide and contribute to material hardening. However, nanovoids completely dissolve by vacancy thermal emission within 1 s at 300ºC, which is extremely short time as compared to reactor campaign duration, and hence the average concentration of incompletely dissolved nanovoids should be too low to answer the requirements to the dislocation barriers implied in our model (that is high number densities of ultra-disperse barriers). On the contrary, self-stabilized Cu-V nanoclusters remain as nuclei for trapping freely migrating vacancies and can even increase their sizes at the expense of newly captured monovacancies. Hence, it seems that the main role of collision cascades is the accelerated creation of self-stabilized vacancy traps in alloys with Cu concentrations above a threshold of ~ 0.1 at% Cu, as compared to the case of freely migrating vacancies. Additionally, the creation of Cu-V nanoclusters in a spatially correlated way should increase their efficiency as obstacles for dislocation glide, though the quantification of this efficiency requires simulation means that we do not use here.

References

[1] M. Akamatsu, J. C. Van Duysen, P. Pareige, P. Auger, J. Nucl. Mater. 225, 192 (1995).
[2] P. Auger, P. Pareige, M. Akamatsu, D. Blavette, J. Nucl. Mater. 225, 225 (1995).
[3] P. Pareige, M.K. Miller, Appl. Surf. Sci, 94-95, 370 (1996).
[4] J.Böhmert, H.-W.Viehrig, A.Ulbricht, J. Nucl. Mat. 334, 71 (2004).
[5] D. J. Bacon, Yu. N. Osetsky, J. Nucl. Mater. 329-333, 1233 (200).
[6] K. Tapasa, D.J. Bacon, Yu.N. Osetsky, Mat.Sci.Eng. A, 400-401, 109 (2005).
[7] M.E. Fine, D. Isheim, Scr.Met, 53, 115 (2005).
[8] S. Schmauder, P. Binkele, Comp.Mat.Sci 24, 42 (2002).
[9] A.Gokhman, J. Böhmert, A.Ulbricht, Rad. Eff. Def. Sol. 158, 783 (2003).
[10] A. V. Barashev, S. I. Golubov, D. J. Bacon, P. E. J. Flewitt and T. A. Lewis, , Acta Mat. 52, 877 (2004).

[11] M. H. Mathon, A. Barbu, F. Dunstetter, F. Maury, N. Lorenzelli, C. H. de Novion, J. Nucl. Mater. 245, 224 (1997).
[12] P. Auger, P. Pareige, M. Akamatsu, J.C. Van Duysen, J. Nucl. Mater. 211, 194 (1994).
[13] E. Vincent, C.S. Becquart, C. Domain, Nucl. Instr. Meth. Phys. Res. B, 228, 137 (2005).
[14] A. Möslang, E. Albert, E. Recknagel, A. Weidinger, P. Moser, Hyperfine Interact. 15/16, 409 (1983).
[15] A.F.Calder, D.J. Bacon, MRS proc., 439, 321 (1997).
[16] C. S. Becquart, C. Domain, J. C. van Duysen, J. M. Raulot, J. Nucl. Mater. 294, 274 (2001).
[17] M. Akamatsu, X. Li, P. Moser, J. C. van Duysen, Ann. Chim. France, 18, 287 (1987).
[18] O. Khrushcheva, E.E. Zhurkin, L. Malerba, C.S. Becquart, C. Domain, M. Hou, Nucl. Instr. Meth. Phys. Res. B 202, 68 (2003).
[19] M.E.J. Newman and G.T. Barkema, Monte Carlo Methods in Statistical Physics, (Clarendon, Oxford, 1999).
[20] C. Domain, C.S. Becquart and L. Malerba, J. Nucl. Mater. 335, 121 (2004).
[21] C. Domain and C. S. Becquart, Phys. Rev. B, 65, 024103 (2001).
[22] C. Becquart, C. Domain, Nucl. Instr. Meth. Phys. Res. B 202, 44 (2003).
[23] Y. Le Bouar, Acta Mat. 49, 2661 (2001).
[24] M.Hou, A.Souidi and C.S.Becquart, J. Phys.: Cond. Matter, 13, 5365-5375 (2001).
[25] A. Souidi, M.Hou, C.S.Becquart; and C. Domain; J. Nucl. Mater. 295**,** 179 (2001).